Titre: Title:	Study of a new class of aperture-compensated microstrip low-pass and band-pass filters
Auteur: Author:	Huizheng Bu
Date:	2000
Type:	Mémoire ou thèse / Dissertation or Thesis
Référence: Citation:	Bu, H. (2000). Study of a new class of aperture-compensated microstrip low-pass and band-pass filters [Mémoire de maîtrise, École Polytechnique de Montréal]. PolyPublie. https://publications.polymtl.ca/8613/

URL de PolyPublie: PolyPublie URL:	https://publications.polymtl.ca/8613/
Directeurs de recherche: Advisors:	Ke Wu
Programme: Program:	Non spécifié

UNIVERSITÉ DE MONTRÉAL

STUDY OF A NEW CLASS OF APERTURE-COMPENSATED MICROSTRIP LOW-PASS AND BAND-PASS FILTERS

BU HUIZHENG
DÉPARTEMENT DE GÉNIE ÉLECTRIQUE
ÉCOLE POLYTECHNIQUE DE MONTRÉAL

MÉMOIRE PRÉSENTÉ EN VUE DE L'OBTENTION
DU DIPLÔME DE MAÎTRISE ÈS SCIENCES APPLIQUÉES
(GÉNIE ÉLECTRIQUE)

JUILLET 2000

UNIVERSITÉ DE MONTRÉAL

ÉCOLE POLYTECHNIQUE DE MONTRÉAL

Ce Mémoire intitulé

STUDY OF A NEW CLASS OF APERTURE-COMPENSATED MICROSTRIP LOW-PASS AND BAND-PASS FILTERS

Présenté: BU Huizheng

En vue de l'obtention du diplôme de: Maîtrise ès sciences appliquées

A été dûment accepté par le jury d'examen constitué de:

M. BOSISIO Renato, M.Sc., président

M. WU Ke, Ph.D., membre et directeur de recherche

M. LAURIN Jean-Jacques, Ph.D., membre

ACKNOWLEDGEMENT

This thesis is a summary of my Master study from January 1998 to July 2000 at the Department of Electrical and Computer Engineering, École Polytechnique de Montréal, towards the completion of my Master's Degree of Applied Sciences. I am grateful to many people who have directly or indirectly helped me complete this research work.

First of all, I would like to express my deep gratitude to Prof. Ke Wu, my supervisor, who has granted me the chance to carry out this research work, and also has given me his invaluable advice and warm encouragement throughout the whole work.

Secondly, I would like to express my acknowledgement to Dr. Lei Zhu who has given me a number of technical advices and discussions with respect to the operating mechanism of several bandpass filters developed in this work.

Also, I would like to thank Mr. Jules Gauthier for his assistance in the circuit fabrication, and Mr. Rene Archambault for his help in the use of computer software.

My thanks also go to all the professors and my colleagues in the Poly-Grames Research Center for providing me with lots of assistances over the past years.

Finally, I would like to thank the Natural Sciences and Engineering Research Council (NSERC) of Canada and Wavesat Telecom, Inc. in Canada for their financial assistance during this work, in particular, through the NSERC/industrial post-graduate fellowship.

ABSTRACT

The objective of this research is to propose, characterize and design a new class of low-cost and high-quality microstrip integrated low-pass and band-pass filters for application in wireless communication and radar systems. The whole content of this work is organized into three main parts: aperture compensation technique, low-loss microstrip low-pass filter, and ultra-broadband microstrip band-pass filter.

First of all, a brief introduction is made on the basic theory of transmission line low-pass and band-pass filters, the state-of-the-art of typical microstrip filters, as well as their related synthesis and optimization design procedures.

Secondly, an aperture compensation technique is presented for the microstrip line structure by partially removing its backside ground plane that is used for the realization of low-loss microstrip line with high impedance as well as parallel-coupled microstrip line (PCML) with tight coupling strength. Their electrical characteristics are investigated and discussed for different aperture sizes, through the use of a fullwave EM software developed in our group.

Thirdly, a microstrip line with backside aperture is used as an equivalent series inductance for the optimized design of a low-loss microstrip low-pass filter due to its high impedance. After its electrical behavior is characterized in terms of a general-purpose equivalent circuit topology, this filter is optimally designed by applying the HP Momentum Software to simulate its entire layout. A filter is fabricated and measured to well verify our predicted results over a wide frequency range (*1.0* to *10.0 GHz*).

Fourthly, a novel class of miniaturized, multi-pole and ultra-broadband microstrip band-pass filters is developed by linking the two identical PCML sections with backside aperture through a microstrip line. On the basis of an equivalent J-inverter based circuit, its operating mechanism is physically studied to illustrate its multi-pole and ultra-broad pass-band that is basically attributed by a tight coupling of the PCML and first-/second-order resonant modes of the line resonator. Further, a capacitively loaded line resonator is formulated for this filter for an effective realization of wide and deep out-of-band rejection. Through the HP Momentum, two types of broadband microstrip band-pass filter are optimally designed with the aim of minimizing their return loss inside the broad pass-band. Also, one filter sample is fabricated and its measured results are in excellent agreement with our optimized results, showing attractive performance with return loss of about *–20dB* and bandwidth of *60%* to *70%*.

Finally, the research work is briefly summarized and future prospects on this research topic are also described.

Étude d'une nouvelle classe de filtre passe-bas et passe-bande microruban compensé par ouverture

Avec la forte croissance, au cours des dernières années, du marché des services de télécommunications, les technologies RF et micro-ondes sans fils utilisant les circuits planaires ont suscité un intérêt sans cesse grandissant dans le milieu industriel. Cet intérêt marqué est attribuable au faible coût, à la compacité des circuits et la facilité de production de masse de ces dispositifs. Les filtres utilisant des lignes de transmission planaires ont été abondamment étudiés, étant considérés comme un élément clé des circuits et sous-systèmes planaires intégrés.

En général, les filtres peuvent être classifiés en circuit passe-bas, passe-bande, coupe-bande et passe-haut. Durant les dernières décennies, des recherches approfondies ont permis de développer une procédure de synthèse systématique se basant sur un simple prototype de filtre passe-bas composé d'éléments discrets, inductances et capacités, en cascade. Selon la réponse en fréquence, ils peuvent être spécifiés en filtre sans ondulation, Chebyshev (ou à ondulation constante) et elliptique. Cependant le filtre Chebychev est le plus utilisé dans la pratique courante. Mon intérêt principal se portera sur la conception théorique et pratique d'une nouvelle classe de filtre passe-bas et passe-bande intégré, qui sera présentée dans ce mémoire.

Un filtre passe-bas microruban est composé de plusieurs sections de ligne microruban (LM) cascadées, avec différentes largeurs de lignes (minces et larges), afin d'obtenir l'impédance caractéristique désirée (élevée ou faible). Une section de LM haute impédance permet d'obtenir une inductance série quasi-discrète tandis qu'une section de LM basse impédance est équivalente à une capacité parallèle. Une LM basse impédance est facilement réalisable en élargissant la largeur de la ligne, toutefois il est plus problématique de construire une LM haute impédance en réduisant la largeur de la

ligne, étant donné les fortes pertes par conduction, les difficultés de fabrication amenées par la grande précision requise et les effets parasites causés par l'épaisseur de la ligne. D'un autre côté, un filtre microruban passe-bande est habituellement formé en agençant ensemble plusieurs résonateurs microrubans demi-longueurs d'ondes de façon à obtenir des éléments de LM couplés parallèlement (LMCP). Chaque LMCP est introduite entre deux résonateurs microrubans adjacents. Un couplage élevé entre deux lignes de cet arrangement de LMPC est toujours requis dans la conception d'un filtre microruban passe-bande possédant une grande largeur de bande. Pour l'obtenir, la façon habituelle consiste à réduire la largeur des LM et des espacements entre celles-ci. Cependant, ceci conduit à une augmentation rapide des pertes par conduction ainsi que des difficultés de fabrication de LM étroites.

Dans ce travail, une technique utilisant la compensation par ouverture est proposée et appliquée à la réalisation de LM faible perte possédant une impédance caractéristique élevée et de LMCP possédant un couplage élevé. Celles-ci sont réalisées en créant une ouverture dans le plan de masse sous la ligne ou les lignes couplées. À l'aide de cette ouverture, il est possible d'alléger grandement le fort couplage présent entre la ligne conductrice et le plan de masse. La LM haute impédance et les LMCP avec fort couplage et faible perte par conduction peuvent être réalisées en gardant les lignes électriquement larges.

En fait, la procédure de conception utilisée à date, a été essentiellement développée en assumant l'indépendance fréquentielle des paramètres des éléments discrets sur toute la bande de fréquence. Il semble alors difficile d'appliquer cette procédure à la conception de filtre passe-bande à large bande ($BW>20\%$). En effet, tous les éléments, comme les résonateurs microrubans ainsi que des sections de lignes couplées, sont fortement dépendants de la fréquence. En utilisant le fort couplage des LMCP avec une ouverture dans le plan de masse, une nouvelle classe de filtre passe-bande microruban multi-pôles,

miniaturisé et à large bande est présentée pour la première fois en attachant un résonateur microruban uniforme ou non-uniforme entre les deux sections de LMCP.

En utilisant les approximations analytiques, les performances des LM sans ouverture dans le plan de masse sont premièrement étudiées sous trois différents aspects : la constante diélectrique effective (ε_{reff}), l'impédance caractéristique (Z_0) et le coefficient de perte par conduction (α_c). Nos résultats démontrent une augmentation graduelle de Z_0 et une diminution de ε_{reff} lorsque la largeur de la ligne (W) diminue tandis que α_c est pour une grande portion des pertes totales et augmente rapidement avec W. En outre, il apparait difficile d'obtenir un Z_0 élevé en gardant les pertes par conduction basses. Dans ce travail, une ligne microruban compensée par ouverture (LM-CO) est créée en enlevant une partie du plan de masse sous le conducteur. Cette LM-CO permet d'obtenir une impédance caractéristique élevée tout en gardant α_c bas, simplement en élargissant l'ouverture dans le plan de masse tout en gardant la ligne conductrice large. Étant donné qu'il n'y a pas de logiciel disponible permettant la caractérisation de cette LM-CO, le logiciel de simulation électromagnétique *SOC-MoM*, développé à notre laboratoire, est employé pour modéliser le deux ports comprenant la LM-CO et deux lignes externes permettant l'excitation ainsi que pour extracter le modèle équivalent du circuit.

Cette structure LM-CO peut être caractérisée par un circuit équivalent comprenant une réactance inductive série (jX_L) et deux réactances capacitives parallèles (jB_L), lesquelles peuvent être à leur tour représentées par des éléments discrets (L et C) à basse fréquence. Des simulations ont été effectuées avec différentes valeurs de longueur (l_L) et largeur (W_a) d'ouverture. Les résultats montrent que l'inductance série (L) augmente linéairement et la capacité parallèle (C) s'élève légèrement en fonction de l_L. Lorsque W_a est élargi, L augmente légèrement tandis que C reste à un niveau élevé. Si W_a est augmenté au-delà de la largeur du conducteur (W), L augmente linéairement et C diminue rapidement.

Dans ce travail, une technique d'extraction simple est développée afin de dériver l'impédance caractéristique (Z_0) et la constante diélectrique effective (ε_{reff}) de la LM-CO à partir des paramètres calculés, jX_L et jB_L. Les paramètres jX_L et jB_L comptent pour la totalité des propriétés électriques du deux ports LM-CO, incluant les effets des discontinuités entre la LM permettant d'exciter la structure et la section LM-CO. Deux structures de LM-CO de longueurs différentes, l_a et l_b, permettent l'extraction des paramètres d'une LM-CO uniforme de longueur $l_L=l_b-l_a$. Cette technique de déplacement des plans de références est développée afin d'enlever les effets des discontinuités entre la LM et la LM-CO. Les résultats démontrent que Z_0 augmente premièrement lentement et ensuite rapidement quand W_a augmente. D'un autre côté, ε_{reff} diminue lentement puis ensuite rapidement suivant l'augmentation de W_a. Avec $W=0,2mm$, Z_0 est d'environ 125Ω pour $W_a=3.0\ mm$ et peut être élevé sur une grande plage en élargissant l'ouverture (W_a).

Le comportement du couplage des LMCP traditionnelles a été largement étudié en utilisant le concept des deux impédances caractéristiques, Z_{0e} et Z_{0o}, correspondant aux modes quasi-TEM pair et impair. Plusieurs équations approchées de conception sont utilisées dans ce travail pour évaluer théoriquement le degré de couplage. Comme la largeur du conducteur (W) augmente, Z_{0e} et Z_{0o} se trouvent à diminuer rapidement. Lorsque la largeur de la fente (S) augmente, Z_{0e} et Z_{0o} se déplace vers le haut et vers le bas respectivement. Ces résultats illustrent que le degré de couplage peut être augmenté en réduisant S et W. Mais, ceci peut conduire à une augmentation des pertes par conduction ainsi que des effets parasites dus à l'épaisseur des conducteurs.

Pour parvenir à un couplage élevé, une ligne microruban couplée parallèlement compensée par ouverture (LMCP-CO) est réalisée en enlevant une partie du plan de masse sous les conducteurs couplés. Ce deux-ports LMCP-CO avec deux LM externes peut être caractérisé par le circuit équivalent d'un inverseur J composé de la susceptance de l'inverseur (J) et de deux sections de lignes de transmission ($\theta/2$). Ce

modèle tient compte du couplage entre les deux lignes conductrices ainsi que des autres effets parasites. La susceptance (J) ne représente pas seulement le degré de couplage mais nous permet aussi de concevoir efficacement le filtre passe-bande en terme de cascade de circuits équivalents.

En utilisant le logiciel *SOC-MoM*, tous les paramètres, J et $\theta/2$, peuvent être dérivés à partir de la matrice Y symétrique calculée du deux-ports. Nos résultats sont obtenus pour différentes largeurs d'ouverture (W_a) de cette LMCP-CO pour une large bande de fréquence et fournissent un bon aperçu du comportement du couplage. Premièrement, la susceptance normalisé J/Y_0 augmente légèrement puis diminue graduellement lorsque la fréquence augmente et ce pour toutes les largeurs d'ouverture (W_a). Lorsque W_a est élargie, J/Y_0 augmente à sa valeur maximale de $0,7$ à partie de $0,27$ pour $W_a=0mm$. Ceci nous montre que la compensation par ouverture nous permet d'obtenir un couplage beaucoup plus élevé. Si W_a est encore élargie, la valeur maximale de J/Y_0 peut être élevée à un niveau supérieur à 1. D'un autre côté, la longueur électrique $\theta/2$ augmente approximativement linéairement en fonction de la fréquence et la valeur maximale de J/Y_0 apparaît autour de la fréquence où $\theta/2=90°$.

Maintenant, la LM-CO est utilisée comme inductance série dans la conception d'un filtre passe-bas à faible perte. Un filtre passe-bas à cinq étages est conçu en raccordant deux LM-CO et trois LM ensemble et est terminé par deux lignes externes 50Ω. Un circuit équivalent est présenté afin d'optimiser ce filtre en utilisant une procédure basée sur les éléments discrets. Dans ce modèle, la LM-CO est caractérisée par un circuit équivalent en π avec une inductance série (jX) et deux capacités parallèles (jB) tandis que la LM et simplifiée à une simple ligne de transmission avec une impédance caractéristique (Z_0) et une longueur électrique (θ).

Dans un premier temps, les paramètres du circuit, jX_L et jB_L, sont obtenus en fonction de la longueur de l'ouverture (l_L) pour une largeur de ligne $W=0.2mm$ et une largeur

d'ouverture W_a=*3,0mm* sous la bande de fréquence comprise entre *1,0* et *10,0 GHz*. Ensuite, la réponse en fréquence de ce filtre passe-bas est conçue de façon optimale en terme du modèle de circuit amélioré avec les paramètres statiques et dynamiques du circuit. La matrice finale ABCD du filtre est obtenue en multipliant plusieurs matrices ABCD associées aux cinq parties du filtre, ensuite les pertes d'insertion $|S_{21}|$ et les pertes de retour $|S_{11}|$ sont dérivées à partir de transformations de la matrice obtenue. Les pertes de retour $|S_{11}|$ obtenues sont d'environ *–15 dB* dans la partie passe-bas (< *3,0 GHz*) et augmentent rapidement à la valeur maximale de *0 dB*, démontrant le caractère coupe-haut. La valeur minimale du $|S_{21}|$ augmente de façon significative à *–27 dB* dans le cas statique tandis qu'elle monte jusqu'à *–23 dB* dans le cas dynamique.

Afin d'étudier le comportement électrique de façon plus précise, le logiciel *HP Momentum* est employé pour simuler les champs électromagnétiques du filtre en entier en augmentant le nombre de maille ainsi qu'en utilisant un maillage non uniforme aux discontinuités. Toutefois, ceci amène quelques problèmes dans la procédure d'optimisation tel que un temps de simulation très long et une large utilisation de la mémoire. La procédure de conception est entreprise en ajustant légèrement le nombre limité de dimensions du filtre de départ, lesquelles sont déterminées par le modèle circuit amélioré. La réponse en fréquence simulée est obtenue pour différentes longueurs d'ouverture (*D*) et longueurs de lignes microrubans (*L*), qui sont : *D=3,0mm* et *L=4,2mm* ainsi que *D=2,9mm* et *L=4,6mm*. Nous pouvons observer une bonne correspondance entre les méthodes sur toute la bande de fréquence (*f=1,0 à 10,0 GHz*). Les pertes d'insertion $|S_{21}|$ minimales de *–27,2 dB* et *–27,5 dB* respectivement se comparent au *–23 dB* obtenu à partir du modèle circuit amélioré. Les pertes de retour $|S_{11}|$ maximales sont de *–19,0 dB*.

En utilisant le filtre optimisé, un filtre passe-bas à LM-CO est fabriqué et mesuré afin de le comparer aux résultats théoriques. Afin de mesurer la réponse en fréquence, les deux lignes microrubans *50 Ω* de sortie sont interconnectées aux ports de l'analyseur de

réseau. La procédure est effectuée en utilisant l'option de calibration deux ports complète. Dans ce cas, les trois changes de référence, soit le circuit ouvert, le circuit fermé et la charge adaptée, permettent de calibrer au bout des lignes coaxiales. Les lignes coaxiales sont alors interconnectées directement ensemble afin de vérifier les performances de transmission et d'adaptation. Après cette calibration, le filtre passe-bas est interconnecté aux câbles de l'analyseur et la réponse en fréquence est mesurée en utilisant la calibration pré-établie.

La réponse en fréquence mesurée, soit $|S_{21}|$ et $|S_{11}|$, présente environ le même comportement de filtrage que ceux obtenus à partir du modèle circuit amélioré et de la simulation *HP Momentum* sur toute la bande de fréquence (*1,0 à 10,0 GHz*). Les pertes de retour $|S_{11}|$ maximales dans le filtre passe-bas sont de *–16 dB* et les pertes d'insertion minimales après la fréquence de coupure sont de *–26 dB*. En comparant les trois réponses en fréquence obtenues, nous pouvons affirmer que les résultats sont plus près des résultats simulés par *HP Momentum* que ceux calculés par le modèle circuit amélioré.

Maintenant, nous aborderons l'étude du couplage intense de la structure proposée LMCP-CO et de son application dans la conception d'un nouveau type de filtre microruban large bande miniaturisé. Comme il a été discuté auparavant, une large ouverture dans le plan de masse permet d'augmenter fortement le couplage maximal (*J/Yo*). Les paramètres de l'inverseur J du circuit équivalent peuvent être extraits efficacement à partir des calculs effectués par le logiciel *SOC-MoM*.

Les paramètres extraits sur une large bande (*1,0 à 10,0 GHz*) indiquent que *J/Yo* varie périodiquement en fonction de la fréquence pour toutes les différentes largeurs d'ouverture. Ceci peut être interprété par le fait que le couplage entre deux conducteurs couplés parallèlement dépend fortement de la longueur électrique des sections de LMCP, c'est-à-dire L/λ_{g0}. Le *J/Yo* maximale apparaît autour des fréquences où

$4L/\lambda_{g0} = (2n-1)$ et le *J/Yo* nul est près de la fréquence où $4L/\lambda_{g0} = 2n$ ($n = 1$ ou 2). De plus, la valeur maximale de *J/Yo* augmente significativement de *0,6* à *1,2*, au-dessus de *1*, lorsque *Wa* passe de *1,4* à *3,0* mm. D'un autre côté, la longueur électrique ($\theta/2$) augmente rapidement, passant de 15^0 à 260^0 lorsque la fréquence varie de *1,0* à *16,0 GHz*. En regardant *J/Yo* et $\theta/2$ ensemble, on remarque que le maximum de *J/Yo* apparaît aux alentours de la fréquence où $\theta/2=90^0$ ou 270^0 tandis que les nuls (*J/Yo*) apparaissent autour de $\theta/2=180^0$.

Les paramètres du réseau inverseur J sont alors transformés en matrice de paramètre S afin d'évaluer le comportement électrique en fréquence. Les simulations des pertes de retour et de transmission, $|S_{11}|$ & $|S_{21}|$, sont obtenues pour différentes largeurs d'ouverture (W_a=*2.2mm* et *3.0mm*). Les résultats montrent bien un comportement de filtre passe-bande avec un ou deux pôles, démontrant que le *J/Yo* distribué en fréquence peut générer sa propre bande passante autour des fréquences où *J/Yo* est maximale et proche de *1*.

Maintenant, une nouvelle classe de filtre passe-bande microruban est présentée et conçue en utilisant le type de couplage présent dans les LMCP-CO. Le filtre prototype est formulé en insérant une section de ligne microruban uniforme entre deux sections identiques de LMCP-CO. Comme décrit précédemment, la section LMCP-CO est caractérisée par un inverseur de susceptance J et deux lignes électriques de longueurs $\theta/2$. La ligne centrale peut être vue comme un facteur de phase (ϕ) additionnel, la longueur électrique totale (Φ) devient alors une somme de trois composantes, $\Phi=\theta/2+\phi+\theta/2$, pour former un résonateur électrique équivalent. Ce résonateur est choisi afin de générer deux pôles additionnels du filtre passe-bande à partir des modes de résonance de premièr et deuxième ordre, correspondant aux cas $\Phi=180°$ et $\Phi=360°$.

En se basant sur le théorème des lignes de transmission, l'admittance d'entrée (Y_{in}) est facilement déduite et exprimée en fonction de J, Y_0 et Φ. Le coefficient de réflexion (S_{11}) peut alors être formulé dans le but d'avoir une meilleure compréhension des ses performances de filtrage. Nous pouvons observer qu'il existe plusieurs pôles aux fréquences où $\Phi=180°$, $\Phi=360°$ et $J=Y_0$. À notre connaissance, les deux premiers pôles correspondent à la première fréquence de résonance. Le ou les deux derniers proviennent de la susceptance accrue de l'inverseur J ($J=Y_0$).

La réponse en fréquence du filtre LMCP-CO a été premièrement obtenue pour une longueur d'ouverture $D=5,0mm$ et une ligne centrale $L=4,9mm$ pour la bande de fréquence comprise entre $1,0$ et $10,0$ GHz, démontrant un comportement passe-bande dans la région d'intérêt. Dans le cas d'une ouverture mince ($W_a=1,4mm$), seulement deux pôles sont observés. Ils apparaissent aux fréquences de résonance de demi et pleine longueur d'onde, dénommées par F_{01} et F_{02}, correspondant à $\Phi=180°$, $\Phi=360°$. La valeur maximale de J apparaît à $0,8Y_0$, indiquant un relativement faible couplage qui correspond à un mauvais comportement de filtre passe-bande dont les pertes de retour minimales sont $|S_{11}|=-6,0dB$ entre F_{01} et F_{02} et le pôle amené par $J=Y_0$ est absent.

Lorsque W_a élargit à $2,2mm$, $|S_{11}|$ décroît rapidement et sa forme est séparée en deux parties par rapport au pôle central. Ce pôle additionnel est généré par la valeur maximale de la suceptance de l'inverseur J qui tend vers Y_0. Lorsque W_a augmente jusqu'à $3,0mm$, il est possible d'observer un pôle se divisant en deux dans la bande passante. À son maximum $J>Y_0$, les deux fréquences ou $J=Y_0$ correspondent aux deux pôles additionnels. Cependant, $|S_{11}|$ est largement dégradé dans la bande passante car $J>>Y_0$. Ce filtre est alors conçu afin d'obtenir une faible perte de retour dans la bande passante en ajustant légèrement la largeur de l'ouverture à $W_a=2,5mm$. Nous trouvons qu'à son maximum $J=1,05Y_0$ et les pertes de retour sont réduites avec succès à $-17,0$ dB en partant de $-9,0$ dB quand l'ouverture était égale à $W_a=3,0mm$. Les quatre pôles

sont dispersés sur une large bande (*3,8* à *7,8 GHz*) et les pertes d'insertion sont inférieures à *–0,2dB*.

Dans le but de vérifier les résultats calculés ainsi que d'obtenir une réponse en fréquence plus précise, le logiciel Momentum de HP est utilisé afin de caractériser le filtre en entier. Les résultats de la simulation Momentum confirment raisonnablement ceux obtenus par le modèle circuit sur une large bande de fréquence. Mais il existe quelques différences notables. En réduisant W_a à *2,1mm* les pertes de retour, $|S_{11}|$, dans la bande passante passent à *–16 dB*, un résultat bien meilleur que le *–8,2 dB* obtenu par la première simulation. Notre attention se portera maintenant sur la suppression harmonique non-désirable de la bande passante, observée dans le filtre dont nous venons de parler.

Pour ce faire, un résonateur composé d'une LM non-uniforme est construit en ajoutant deux tronçons circuit ouvert au milieu de la ligne centrale. Cette paire de tronçons peut être vue comme une susceptance capacitive court-circuit (jB_s). À la position centrale nous obtenons un court-circuit pour le premier et troisième mode de résonance (mode impair) et un circuit ouvert pour le deuxième et quatrième mode de résonance (mode pair). L'ajout de ces tronçons doit permettre de diminuer efficacement la deuxième et quatrième fréquence de résonance tandis que la première et la troisième demeurent inchangées.

La réponse en fréquence prédite est premièrement obtenue en utilisant le circuit équivalent pour un couplage faible : $J<<Y_0$. Les résultats montrent que la première et la troisième fréquence de résonance, F_{01} et F_{03}, demeurent identiques même si la longueur de tronçon (S) est augmentée significativement. Toutefois, la seconde et quatrième fréquence de résonance, F_{02} et F_{04}, se trouvent à diminuer vers leur contrepartie (première et troisième) quand S augmente. La bande de réjection est significativement élargie alors que la bande passante diminue de *3.2* GHz à *0.8* GHz. L'ajout de tronçons capacitifs permet de réaliser un filtre passe-bande large bande avec une bonne

suppression des harmoniques. La réponse en fréquence optimisée, pour une longueur de tronçon *S=2,08mm*, est obtenue sur une large bande de fréquence (*1.0 à 15 GHz*) et permet d'obtenir d'excellents résultats avec une largeur de bande de *60%* et un $|S_{11}|$ inférieur à *-20 dB* pour un filtre quatre pôles. Dans ce cas, une bande passante causée par les harmoniques non-désirable apparaît à *14,0 GHz*, démontrant une amélioration de la bande de réjection, maintenant de *100%*.

Le logiciel Momentum de HP est alors utilisé afin de simuler le filtre en entier. Les trois résultats obtenus des différentes techniques, montrent un comportement large bande identique avec la fréquence centrale autour de *6,6 GHz* et une bande passante causée par les harmoniques à *14,4 GHz*. Nous pouvons aussi observer que les pertes de retour sont asymétriques en fréquence de chaque côté de la bande passante. En allongeant légèrement la longueur des tronçons de *2,36 mm* à *3,46 mm*, la valeur maximale de $|S_{11}|$ diminue de *–15 dB* à *–17 dB* et la bande passante causée par les harmoniques diminue en fréquence. D'un autre côté, les pertes d'insertion minimales sont supérieures à *–0,4 dB*. En ajustant légèrement la longueur de la ligne (*L*) les pertes de retour sont améliorées, passant de *–17,2* à *–20,7* dB.

Afin de vérifier la réponse en fréquence optimisée, utilisant les différentes techniques mentionnées, un filtre passe-bande est conçu et mesuré. La longueur totale de ce filtre avec les tronçons (*D+L+D=13,36mm*) est inférieure à la longueur d'onde guidée, soit environ $0,7\lambda_{g0}$ à la fréquence centrale (f_0=*6,1 GHz*). Les résultats mesurés sont conformes à ceux prédits, démontrant une large bande passante et une excellente réjection. Les pertes d'insertion minimales sont de *–0,6 dB* comparativement au *–0,4 dB* prédit et les pertes de retour maximales sont de *–16 dB*, légèrement supérieures à la valeur prédite de *–20,0 dB*.

TABLE OF CONTENTS

Acknowledgement iv

Abstract v

Summary (French) vii

Table of contents xviii

Figure list xxi

Table list xxvii

CHAPTER I

Introduction: Theory and Background 1

1.1 Prototype Lowpass Filter 2

1.2 Transmission Line Lowpass Filter 6

1.3 Admittance Inverter and Modified Prototype Filter 9

1.4 Transmission Line Bandpass Filter 12

1.5 Purpose and Content of This Research Work 15

1.6 References 17

CHAPTER II

Aperture Compensation Technique: Concept and Characteristics 18

2.1 Introduction 18

2.2 Traditional Microstrip Line (ML) 18

2.3 Aperture-Compensated Microstrip Line (AC-ML) 23

2.4 Traditional Parallel-Coupled Microstrip Line (PCML) 34

2.5 Aperture-Compensated Parallel-Coupled Microstrip Line (AC-PCML) 40

2.6 Conclusion 49

2.7 References 50

CHAPTER III

Aperture-Compensated Microstrip Line (AC-ML) for Design of Low-Loss Microstrip Lowpass Filter 51

3.1 Introduction 51

3.2 Layout and Unified Circuit Model 51

3.3 Unified Circuit Model of AC-ML Structure 55

3.4 Circuit Model Based Synthesis and Optimization 58

3.5 Fullwave EM Simulation 62

3.6 Measurement and Discussion 65

3.7 Conclusion 68

3.8 References 68

CHAPTER IV

Aperture-Compensated Parallel-Coupled Microstrip Line (AC-PCML) for Design of Broadband Microstrip Bandpass Filter 69

4.1 Introduction 69

4.2 Unified Circuit Model of A Single AC-PCML Structure 70

4.3 Concept and Model-Based Design of Prototype Bandpass Filter 76

4.4 Fullwave Characterization of Prototype Bandpass Filter 82

4.5 Concept and Model-Based Design of Improved Bandpass Filter 85

4.6 Numerical & Experimental Investigation of Improved Bandpass filter 91

4.7 Conclusion 99

4.8 References 100

CHAPTER V

Conclusions **101**

Figure List

Figure 1.1 n-stage prototype lowpass filter. (a) inductance-input type; (b) capacitance-input type 2

Figure 1.2 Insertion loss (L) of n-stage Chebyshev prototype lowpass filter versus normalized (Ω-1): L_p=$0.1dB$. 4

Figure 1.3 n-stage lumped-element lowpass filter: inductance type 6

Figure 1.4 Physical configuration and equivalent circuit network of microstrip quasi-lumped series inductance and shunt capacitance elements. (a) series inductance element; (b) shunt capacitance element 7

Figure 1.5 Physical layout and its equivalent circuit topology of a 5-stage microstrip lowpass filter 9

Figure 1.6 K- and J-inverter network 10

Figure 1.7 Two classes of n-stage modified prototype filters. (a) K-inverter filter; (b) J-inverter filter 12

Figure 1.8 Coupled line section and its equivalent K- or J-inverter network 13

Figure 1.9 Equivalent topology and layout of a 3-stage microstrip bandpass filter. (a) cascaded J-inverter topology; (b) microstrip bandpass filter layout.. 14

Figure 2.1 Cross-section of traditional microstrip line 19

Figure 2.2 Characteristic impedance (Z_0) and effective dielectric constant (ε_r) as a function of strip width (W) under the strip thickness t=0.1mil & 0.7mil.. 21

Figure 2.3 Loss attenuation coefficients (α_c and α_d) as a function of strip width (W) at the operating frequency: f=2.0GHz as an example 22

Figure 2.4 Cross-section of aperture-compensated microstrip line (AC-ML) ... 24

Figure 2.5 Geometrical layout and its equivalent circuit model of an aperture-compensated microstrip line (AC-ML) structure to be studied.
(a) geometrical layout; (b) equivalent circuit model 25

Figure 2.6 Extracted equivalent series inductance ($L=X_L/\omega$) and shunt capacitance ($C=B_L/\omega$) as a function of aperture width (W_a).
(a) series inductance 26
(b) shunt capacitance 27

Figure 2.7 Layout and equivalent circuit model of an AC-ML with line length (l_a).
(a) layout; (b) equivalent circuit model 28

Figure 2.8 Layout and equivalent circuit model of an AC-ML with line length (l_b).
(a) layout; (b) initial circuit model; (c) alternative circuit model 29

Figure 2.9 Extracted equivalent series reactance (jX_L) and shunt susceptance (jB_L) as a function of operating frequency (f) under the width: $W_a=3.0mm$.
(a) series reactance (jX_L) 33
(b) shunt susceptance (jB_L) 33

Figure 2.10 Cross-section of a parallel-coupled microstrip line (PCML) 34

Figure 2.11 Electric and magnetic filed configuration of even and odd modes for a parallel-coupled microstrip line (PCML) 35

Figure 2.12 Characteristic impedance and effective dielectric constant of the even- and odd-modes as a function of W/h.
(a) characteristic impedance 40
(b) effective dielectric constant 40

Figure 2.13 Cross-section and top-view of the aperture-compensated parallel-coupled microstrip line (AC-PCML) structure to be studied. (a) cross-section; (b) top-view 41

Figure 2.14 Two sets of unified equivalent circuit model used for characterization of the two-port AC-PCML structure. (a) Y-matrix model; (b) J-inverter model 42

Figure 2.15 Normalized J-inverter susceptance (J/Y_0) and equivalent electrical line length ($\theta/2$) of an AC-PCML structure with different W_a. (a) J-inverter susceptance ..... 44 (b) equivalent electrical line length 45

Figure 2.16 Normalized J-inverter susceptance (J/Y_0) as a function of equivalent electrical line length ($\theta/2$) 47

Figure 2.17 Calculated insertion loss (S_{21}) as a function of frequency (f) under differentaperture width (W_a) 48

Figure 3.1 Schematic layout of two classes of microstrip lowpass filters usingthe aperture-compensated microstrip line (AC-ML) structure. (a) capacitive-input class; (b) inductive-input class 52

Figure 3.2 Top-view and its two equivalent circuit models of a five-stage AC-ML lowpass filter. (a) top-view; (b) initial circuit model; (c) improved circuit model 53

Figure 3.3 Layout and equivalent circuit model of the two-port AC-ML section. (a) layout; (b) equivalent circuit model 55

Figure 3.4 Extracted series inductance (jX_L) and shunt capacitance (jB_L) as a function of operating frequency: static case (dashed line) and dynamic case (solid line).

(a) series reactance (jX_L) 56
(b) shunt capacitance (jB_L) 57

Figure 3.5 Predicted frequency response of a five-stage microstrip lowpass filter, obtained from two equivalent circuit models as in Figure 3.2(b) and (c).
(a) insertion loss (S_{21}) 60
(b) return loss (S_{11}) 61

Figure 3.6 Predicted and optimized frequency response of the five-stage microstrip lowpass filter obtained from the HP Momentum software 64

Figure 3.7 Upper- and bottom-layer configuration of a five-stage microstrip lowpass filter arranged for etching fabrication.
(a) upper-layer 65
(b) bottom-layer 66

Figure 3.8 Measured frequency response of the five-stage microstrip lowpass filter sample using the HP Network Analyzer 67

Figure 4.1 Geometry and unified equivalent circuit model of the two-port AC-PCML. (a) geometrical layout; (b) top-view;
(c) J-inverter network 71

Figure 4.2 SOC-calibrated J-inverter network parameters of the two-port AC-PCMLwith different aperture widths W_a=*1.4, 2.2, 3.0mm.*
(a) normalized J-inverter susceptance 72
(b) equivalent electrical line length 73

Figure 4.3 Predicted insertion and return losses (S21 & S11) of the two-port AC-PCMLcalculated from the extracted J-inverter susceptance plotted in Figure 4.2(a) 75

Figure 4.4 Schematic layout and its equivalent circuit topology of the proposed multi-pole bandpass filter with a single uniform line resonator.

(a) layout 76
(b) equivalent circuit model 77

Figure 4.5 Predicted frequency response of the filter layout as described in Figure4.4 with different aperture widths W_a.
(a) insertion loss $|S_{21}|$ 78
(b) return loss $|S_{11}|$ 79

Figure 4.6 Optimized frequency response of the prototype multi-pole bandpass filter 81

Figure 4.7 Predicted frequency response of the prototype bandpass filter with the same aperture width (W_a=2.5mm) as in Figure 4.4, from the HP Momentum 82

Figure 4.8 Optimized frequency response of this bandpass filter with aperture width (W_a=2.1mm) 84

Figure 4.9 Schematic layout and its equivalent circuit topology of the improved bandpass filter with a single capacitive-loaded line resonator.
(a) layout (b) equivalent circuit model 86

Figure 4.10 Predicted frequency response of the filter layout with different stub length S.
(a) return loss (S_{11}) 89
(b) insertion loss (S_{21}) 90

Figure 4.11 Optimized frequency response of the filter layout with the stub length (S=2.08mm) 91

Figure 4.12 Simulated frequency response of the bandpass filter using the HP Momentum software: Group (I).
(a) return loss (S_{11}) 92
(b) insertion loss (S_{21}) 93

Figure 4.13 Simulated frequency response of the bandpass filter using the HP Momentum software: Group (II).
(a) return loss (S_{11}) 94
(b) insertion loss (S_{21}) 95

Figure 4.14 Optimized frequency response of this bandpass filter using the HP Momentum software 96

Figure 4.15 Upper- and bottom-layer configration of an improved microstrip bandpass filter arranged for etching fabrication. (a) upper-layer; (b) bottom-layer 97

Figure 4.16 Comparison of predicted and measured frequency response of the improved bandpass filter with completely same dimension 98

Table List

Table 1.1 Lumped parameters (g_i) of n-stage Chebyshev lowpass filter (L_p=0.1dB & k=0.15262) 5

Table 2.1 MoM-extracted characteristic impedance (Z_o) and effective dielectric constant (ε_{reff}) of AC-ML line versus aperture width (W_a) with those of 2-D static ML (W=0.2mm, f=1.0GHz, l_a=0.6mm and l_b=3.0mm) 32

CHAPTER I
INTRODUCTION: THEORY AND BACKGROUND

As the market for telecommunication services in the areas of Internet, mobile and multi-media has grown very rapidly over recent years, wireless RF & microwave technologies are gaining an increasing attention in the industrial and academic sectors. The rapid development of fabrication and processing techniques for monolithic microwave integrated circuits (MMICs) has further aroused a considerable interest in exploiting commercial wireless systems through the use of planar integrated circuits as basic building blocks. Basically, it should be attributed to their competitive electrical features in practical application, such as low fabrication cost, size compactness and easy for mass manufacturing.

Planar transmission line filters have extensively been studied and developed as one of key circuit components in the design of planar integrated circuits and subsystems. Usually, these filters can be conceptually classified into the following four distinct structures: low-pass (or highstop), band-pass, band-stop and high-pass (or low-stop) filters, according to their electrical behaviors. They can be designed and realized on the basis of a variety of planar and uniplanar transmission line structures, such as microstrip line (ML), coplanar waveguide (CPW), coplanar stripline (CPS) and slotline (SL).

To carry out the design procedure for these integrated filters, extensive research works have been successfully done in the past decades so that a systematic synthesis design procedure has been established for the synthesis, design and optimization of filter layouts in an efficient and effective manner. Our following discussion will briefly be made on the basic theory, physical layout and electrical characteristics of traditional transmission line filter structures in conjunction with microstrip low-pass and band-pass filters.

The fundamental concept and theory of planar transmission line filters are generally developed and formulated on the basis of an equivalent lumped prototype low-pass filter, which is made up of several lumped inductors and capacitors in the ladder-shaped manner. We begin our description from a so-called "insertion attenuation" parameter (L) in a two-port lossless circuit network, which is defined as the ratio of the input power (P_i) and the output power (P_l). According to its frequency characteristics in the synthesis design procedure, the filter itself is often classified into maximally flat, Chebyshev (or equi-ripple) and elliptical function filters. In this work, we will focus our attention on the understanding and characterization of Chebyshev multi-stage low-pass and band-pass filters.

1.1 PROTOTYPE LOWPASS FILTER

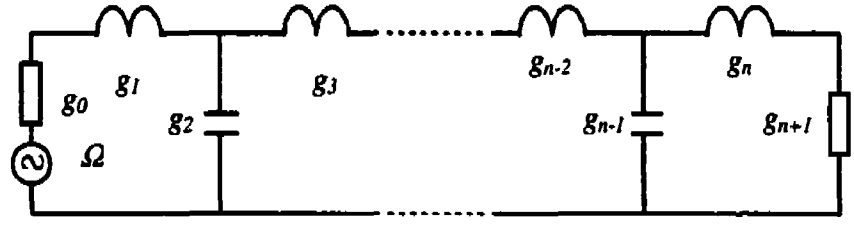

(a) inductance-input type

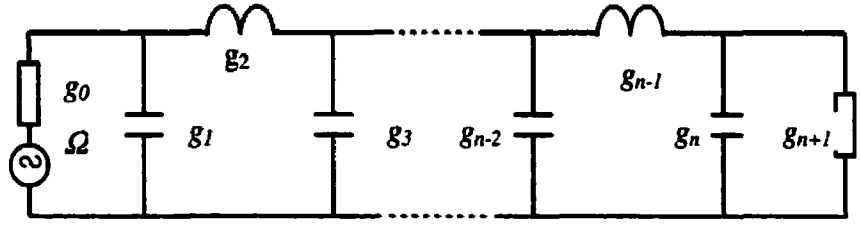

(b) capacitance-input type

Figure 1.1 n-stage prototype lowpass filter

Prototype low-pass filter is a two-port lumped-element network over the low frequency range and is extended into the high frequency range as a theoretical basis towards the

establishment of a synthesis procedure in the design of RF & microwave filters. Figure 1.1(a) and (b) illustrate the circuit topology of two classes of n-stage prototype lowpass filters, named, inductance-input type and capacitance-input type, respectively. In Figure 1.1, the parameters, g_0 and g_{n+1}, represent the normalized resistance or conductance at the input and output terminals while g_i (i= 1, 2 ,...., n) is the i-th normalized inductance or capacitance of this lowpass filter. Otherwise, Ω is the so-called "normalized frequency", which can be linked with the actual RF frequency through the frequency transformation under the filter classification. For the lowpass filter, $\Omega=\omega/\omega_c$, where ω_c is its cutoff frequency.

On the basis of a simple circuit theorem, the normalized input impedance (z_{in}) at the source terminal can analytically be deduced and further can be expressed into the following algebraic equation,

$$z_{in} = j\Omega g_1 + \cfrac{1}{j\Omega g_2 + \cdots \cfrac{\cdots}{j\Omega g_n + \cfrac{1}{g_{n+1}}}} \tag{1.1}$$

Accordingly, the related insertion attenuation (L) can be obtained with the use of its relationship with the reflection coefficient: $\Gamma=(z_{in}-g_0)/(z_{in}+g_0)$.

$$L = \frac{P_i}{P_l} = \frac{P_i}{P_i - P_r} = \frac{1}{1-|\Gamma|^2} \tag{1.2}$$

For a two-port lossless network in conjunction with two prototype filters illustrated in Figure 1.1, the insertion attenuation parameter ($L>1$) can be in general expressed as an algebroidal function with the normalized frequency (Ω).

$$L = 1 + P^2(\Omega) \tag{1.3}$$

In the case of n-stage Chebyshev or equi-ripple filter, Equation (1.3) can be further expressed in terms of a Chebyshev function $T_n(\Omega)$ as,

$$L = 1 + k^2 T_n^2(\Omega) \tag{1.4a}$$

or

$$L(dB) = 10 \log_{10}\left(1 + k^2 T_n^2(\Omega)\right) \tag{1.4b}$$

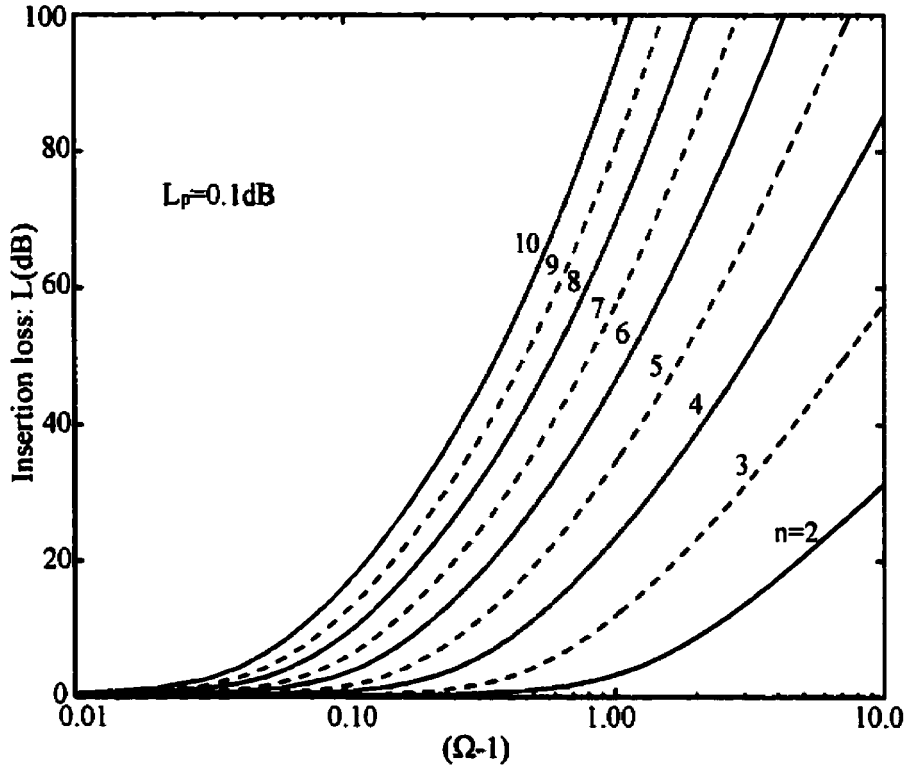

Figure 1.2 Insertion loss (L) of n-stage Chebyshev prototype low-pass filter versus normalized (Ω-1): L_p=0.1dB.

By comparing Equation (1.2) and (1.4) with the help of Equation (1.1), the stage number and each lumped parameters (g_i) of a prototype low-pass filter can be determined according to the maximum insertion attenuation (L_p) and the cutoff

frequency (ω_c) designated in the filter design. At the frequency of $\omega=\omega_c$ where $\Omega=1$, we can express L_p as a function of unknown coefficient (k) from Equation (1.4).

$$L_p(dB) = 10\log_{10}(1+k^2) \quad (dB) \tag{1.5}$$

From Equation (1.5), the coefficient k can accordingly be solved if L_p is given. For convenience in implementing the practical design, Equation (1.4) is usually expressed in the form of graphic curves under the different L_p and n. Figure 1.2 illustrates the insertion loss $L(dB)$ versus $(\Omega-1)$ in the case of $L_p=0.1dB$, where $k=0.15262$, under $n=2, 3, \ldots, 10$, showing that the insertion loss (L) beyond the operating frequency band gains a great enhancement with a sharply changed configuration as the number (n) increases. Table 1.1 lists the values of each parameter (g_i) in this case, for example, used for the synthesis design of such a prototype filter with the n-pole.

Table 1.1 Lumped parameters (gi) of n-stage Chebyshev lowpass filter ($L_p=0.1dB$ & $k=0.15262$)

n	g_1	g_2	g_3	g_4	g_5	g_6	g_7	g_8	g_9	g_{10}	g_{11}
1	0.3052	1.0000									
2	0.8430	0.6220	1.3554								
3	1.0315	1.1474	1.0315	1.0000							
4	1.1088	1.3061	1.7703	0.8180	1.3554						
5	1.1468	1.3712	1.9750	1.3712	1.1468	1.0000					
6	1.1681	1.4039	2.0562	1.5170	1.9029	0.8618	1.3554				
7	1.1811	1.4228	2.0966	1.5733	2.0966	1.4228	1.1811	1.0000			
8	1.1897	1.4346	2.1199	1.6010	2.1699	1.5640	1.9444	0.8778	1.3554		
9	1.1956	1.4425	2.1345	1.6167	2.2053	1.6167	2.1345	1.4425	1.1956	1.0000	
10	1.1999	1.4481	2.1444	1.6265	2.2253	1.6418	2.2046	1.5821	1.9628	0.8853	1.3554

1.2 TRANSMISSION LINE LOW-PASS FILTER

In this section, a brief description will be focused on the issue of how to apply the above closed-form design equations in the synthesis design of n-stage transmission line low-pass filters. It is one of the important issues to be addressed that the normalized frequency (Ω) is transformed into the related actual radio frequency (ω) in order to link the insertion loss curves in the prototype low-pass filter with those in its corresponding lumped-element low-pass filter.

In the case of a low-pass filter, the relationship between two frequencies, Ω and ω, can simply be defined as $\Omega=\omega/\omega_c$, where ω_c is the cutoff frequency. Now, it is the next issue to establish the relationship between two groups of insertion loss for two types of low-pass filter.

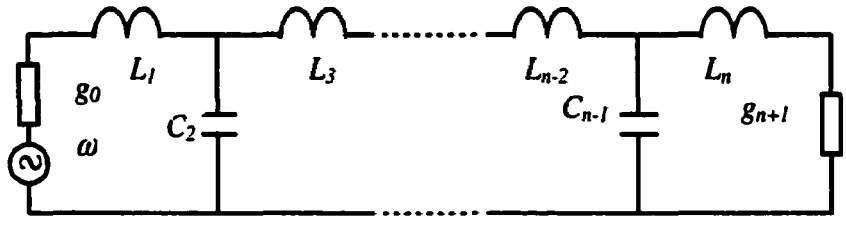

Figure 1.3 n-stage lumped-element low-pass filter: inductance type

Figure 1.3 depicts the circuit scheme of the n-stage lumped-element LC low-pass filter (inductance-input type), as opposed to its prototype low-pass filter in Figure 1.1(a). The equality theorem of insertion loss allows that the two networks should have the equal insertion loss if they have the similar circuit topology with identical branch impedance at each location or point of their whole circuit topology. Under this condition, it allows us simply formulating the inter-relationship between two groups of component parameters, as illustrated in Figure 1.1(a) and Figure 1.3, respectively.

$$\begin{cases} L_i = \dfrac{Z_0}{\omega_c} g_i \\ C_i = \dfrac{1}{\omega_c Z_0} g_i \end{cases} \qquad (i=1,2,\ldots n) \qquad (1.6)$$

At the low operating frequency, e.g., lower than *1.0GHz*, it usually preferred to directly use the high-quality, low-lose and compact-size lumped capacitor and inductor chips in the filter design. As the frequency increases beyond *1.0GHz*, however, some of frequency-distributed parasitic parameters appear that may seriously cause the degradation of the wanted electrical properties of these lumped chips.

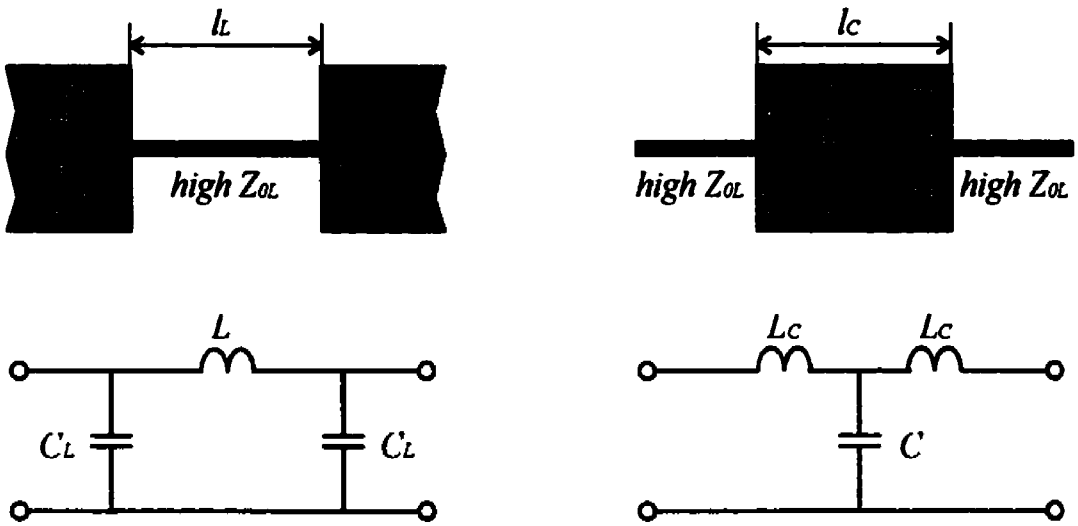

(a) series inductance element (b) shunt capacitance element

Figure 1.4 Physical configuration and equivalent circuit network of microstrip quasi-lumped series inductance and shunt capacitance elements

On the other hand, an increasing interest has been shifted towards the development of microwave low-pass filters using transmission line structures such as microstrip line (ML), coplanar waveguide (CPW), coplanar stripline (CPS) and etc. Due to several attractive features such as low fabrication cost, easy for mass manufacturing and size-

compactness, these printed filters has widely been studied and developed as one of key components in the microwave integrated circuits and subsystems. In this work, our main research focus will be on the filter structures, which are formed by traditional and aperture-compensated microstrip lines.

Figure 1.4 depicts the physical configuration and their equivalent circuit networks of microstrip quasi-lumped series inductance and shunt capacitance elements, respectively. The former is made up of a high-impedance microstrip line section with extremely narrow strip width, while the latter corresponds to a low-impedance line section with extended strip width.

Under the assumed condition that the line length (l_L and l_C) is electrically short, these microstrip elements act predominantly as a perfect series inductor or perfect shunt capacitor, respectively. Their electrical parameters (L and C) can be expressed in a class of closed-form equations. In addition, two pairs of parasitic lumped elements at the two sides, C_L and L_C, are contributed by the step discontinuities and also frequency-distributed line section as the frequency increases beyond the quasi-static range.

$$L = \frac{Z_{0L} l \sqrt{\varepsilon_{rL}}}{c}$$

$$C = \frac{l \sqrt{\varepsilon_{rC}}}{Z_{0C} c} \qquad (c\text{: light speed}) \qquad (1.7)$$

With the use of these quasi-lumped elements, the n-stage transmission line low-pass filter can be realized by linking them in a cascaded manner. Figure 1.5 shows the layout and its equivalent circuit topology of a 5-stage microstrip low-pass filter. In the synthesis design, the stage number (n) should be determined under the specified electrical properties such as maximum insertion loss (L_p) and out-of-band frequency response, according to the calculated curves as plotted in Figure 1.2 (L_p=*0.1dB*). At the

same time, each lumped parameter (g_i) in the prototype low-pass filter can be obtained with reference to Table 1.1.

As a result, each equivalent quasi-lumped element (L_i and C_i) in the transmission line filter as shown on the bottom of Figure 1.5 can be deduced through Equation (1.6). Finally, the dimension of each microstrip section with different strip widths as illustrated at the top of Figure 1.5 can be derived on the basis of pre-calculated design curves of characteristic impedance (Z_{OL} & Z_{OC}) and effective dielectric constant (ε_{rL} & ε_{rC}). These transmission parameters have been derived and expressed in a set of closed-form equations, which will be written in Chapter II.

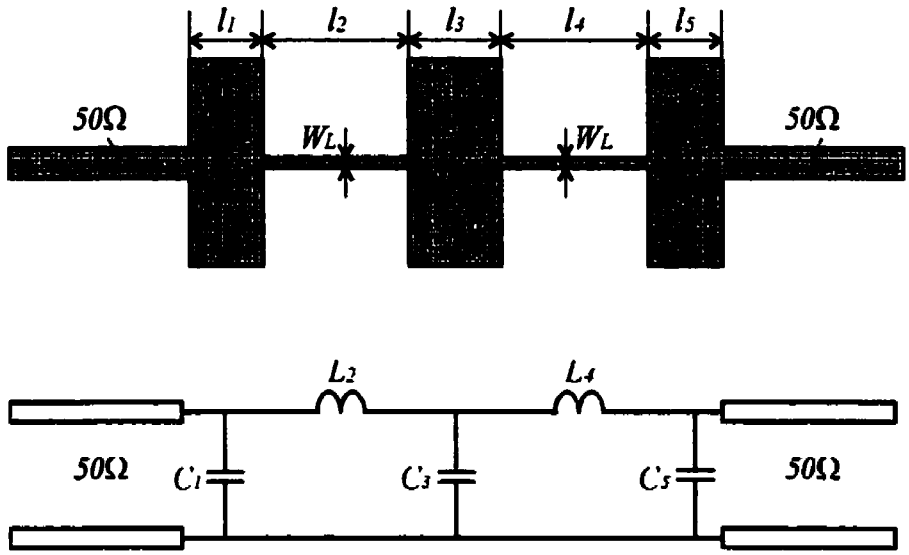

Figure 1.5 Physical layout and its equivalent circuit topology of a 5-stage microstrip low-pass filter

1.3 Admittance Inverter and Modified Prototype Filter

To extend effectively the above design theorem stemming from the prototype low-pass filter in the design of microwave band-pass filter, we start with the description of a

modified prototype bandpass filter using a frequency transformation. According to the existence of lower and upper-cutoff frequencies (ω_1 and ω_2) and its central frequency (ω_0), it is usual way to define the frequency transformation as a function of the normalized frequency (Ω),

$$\Omega = \frac{\omega_0}{\omega_2 - \omega_1}\left(\frac{\omega}{\omega_0} - \frac{\omega_0}{\omega}\right) = \frac{1}{w}\left(\frac{\omega}{\omega_0} - \frac{\omega_0}{\omega}\right) \tag{1.8}$$

where $w = (\omega_2 - \omega_1)/\omega_0$ is the relative frequency bandwidth (BW). Following Equation (1.8), we can build up an initial band-pass filter topology with cascaded series and shunt LC branch elements simultaneously. Unfortunately, it is extremely difficult in practice to realize both series and shunt LC resonator elements. In this case, the designer prefers to use a so-called "impedance K-inverter" or "admittance J-inverter" to remove out either shunt LC resonator elements or series LC resonator elements. Figure 1.6 depicts their circuit network. Equation (1.9a) and (1.9b) illustrate the input impedance (Z_{in}) or admittance (Y_{in}) as a function of output load impedance or admittance (Z_l or Y_l) through the K reactance or J susceptance.

$$Z_{in} = \frac{K^2}{Z_l} \tag{1.9a}$$

$$Y_{in} = \frac{J^2}{Y_l} \tag{1.9b}$$

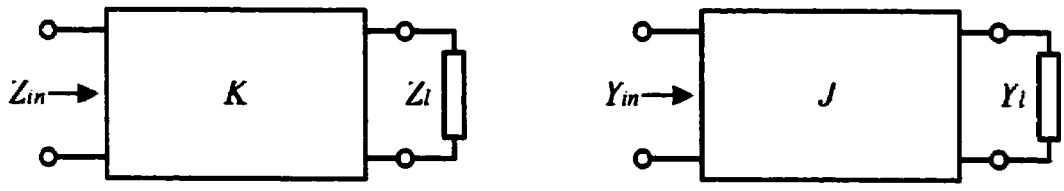

Figure 1.6 K- and J-inverter network

Under the equality of insertion loss mentioned above, two classes of prototype low-pass filters as shown in Figure 1.1 can be expressed as a cascaded circuit network in terms of the K-inverter or J-inverter. Figure 1.7 illustrates two classes of modified prototype lowpass filters, where R_A & R_B or G_A & G_B are the resistance or conductance inside the source and at the load, respectively. By ordering the equality of their reflection coefficients in the two types of circuit networks as depicted in Figure 1.1 and Figure 1.7, we can deduce the three closed-form equations to establish the relationship among all their circuit parameters.

Equation (1.10) and Equation (1.11) give the two groups of these equations in the case of K-inverter and J-inverter networks. As a result, each K-inverter reactance ($K_{i,i+1}$) or J-inverter susceptance ($J_{i,i+1}$) can be determined as each g_i found from Table 1.1 and series L_i or shunt C_i are given.

K-inverter Network:

$$\begin{cases} K_{01} = \sqrt{\dfrac{R_A L_1}{g_0 g_1}} \\ K_{i,i+1} = \sqrt{\dfrac{L_i L_{i+1}}{g_i g_{i+1}}} \qquad (i=1,2,\ldots,n-1) \\ K_{n,n+1} = \sqrt{\dfrac{R_B L_n}{g_n g_{n+1}}} \end{cases} \tag{1.10}$$

J-inverter network:

$$\begin{cases} J_{01} = \sqrt{\dfrac{G_A C_1}{g_0 g_1}} \\ J_{i,i+1} = \sqrt{\dfrac{C_i C_{i+1}}{g_i g_{i+1}}} \qquad (i=1,2,\ldots,n-1) \\ J_{n,n+1} = \sqrt{\dfrac{G_B C_n}{g_n g_{n+1}}} \end{cases} \tag{1.11}$$

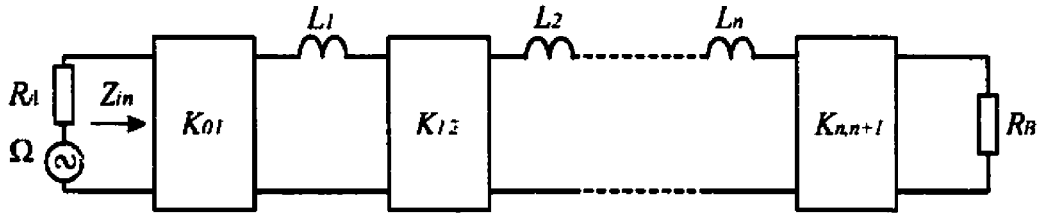

(a) K-inverter filter

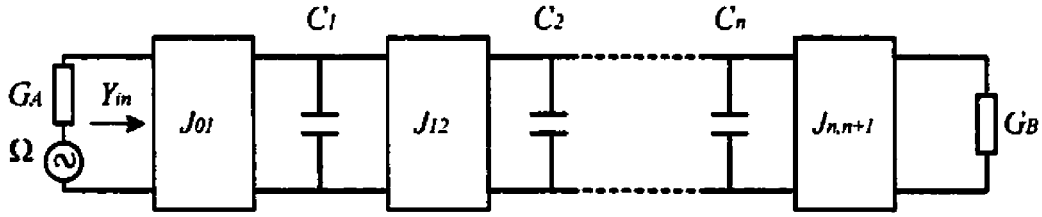

(b) J-inverter filter

Figure 1.7 Two classes of n-stage modified prototype filters

1.4 TRANSMISSION LINE BANDPASS FILTER

There are several methods to date in the realization of K-inverter and/or J-inverter networks such as quarter-wavelength line section, lumped shunt inductor, lumped series capacitor, parallel-coupled line section and etc. To our knowledge, the parallel-coupled line section with the quarter-wavelength line length at the central frequency has gained popularity in the design of practical band-pass filters.

Figure 1.8 illustrates the configuration and its equivalent K- or J-inverter network of a parallel-coupled line section with two characteristic impedances, Z_{0e} and Z_{0o}, with regards to the even and odd coupled modes, respectively. This coupled line section can be very effectively used as a K-inverter or J-inverter in the filter design. By ordering the equality in their terminal voltages and currents of the two networks as in Figure 1.8, we can derive closed-form equations in linking the even/odd characteristic impedances with K- or J-inverter network parameters, as written in Equation (1.12) and Equation (1.13). However, it should be noted here that these two groups of equations are completely

accurate in theory only if $\phi=\pi/2$, and become gradually approximate as the frequency goes away from its central frequency.

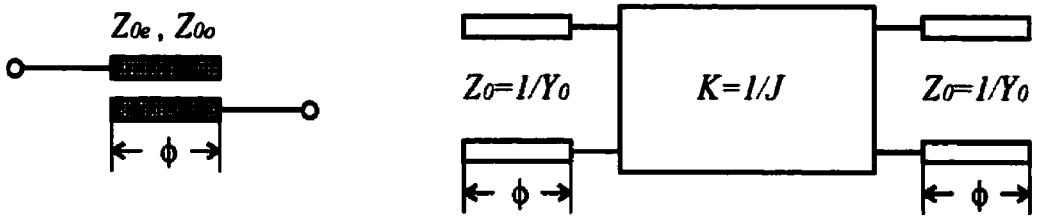

Figure 1.8 Coupled line section and its equivalent K- or J-inverter network

$$Z_{0e} = Z_0\left(1+\frac{Z_0}{K}+\frac{Z_0^2}{K^2}\right)=\frac{1}{Y_0}\left(1+\frac{J}{Y_0}+\frac{J^2}{Y_0^2}\right) \tag{1.12}$$

$$Z_{0o} = Z_0\left(1-\frac{Z_0}{K}+\frac{Z_0^2}{K^2}\right)=\frac{1}{Y_0}\left(1-\frac{J}{Y_0}+\frac{J^2}{Y_0^2}\right) \tag{1.13}$$

Now, it turns to the issue on how to define the series inductance (L_i) or shunt capacitance (C_i) as shown in Figure 1.8 in terms of the parallel-coupled line characteristic impedance (Z_0) and the specified frequency bandwidth (w). It is done through the use of the so-called reactance or susceptance slope parameters, x_i or b_i, at the central frequency (ω_0). According to the frequency transformation equation in Equation (1.8), L_i & C_i can be expressed as the series or shunt LC element in the RF frequency (ω), respectively. In the J-inverter case, we give a simple formula under the condition that the electrical line length is close to the half-wavelength, e.g., $\phi=\pi$.

$$C_i = wb_i = \frac{\pi w Y_0}{2} \tag{1.14}$$

By substituting Equation (1.14) into Equation (1.11), we can obtain one group of equations, that is, Equation (1.15) to link the J-inverter susceptance ($J_{i,i+1}$) with the lumped parameters (g_i) in the prototype lowpass filter as shown in Figure.1.

$$\begin{cases} \dfrac{J_{01}}{Y_0} = \sqrt{\dfrac{\pi w}{2 g_0 g_1}} \\ \dfrac{J_{i,i+1}}{Y_0} = \dfrac{\pi w}{2\sqrt{g_i g_{i+1}}} \\ \dfrac{J_{n,n+1}}{Y_0} = \sqrt{\dfrac{\pi w}{2 g_n g_{n+1}}} \end{cases} \qquad (i=1,2,\ldots,n-1) \qquad (1.15)$$

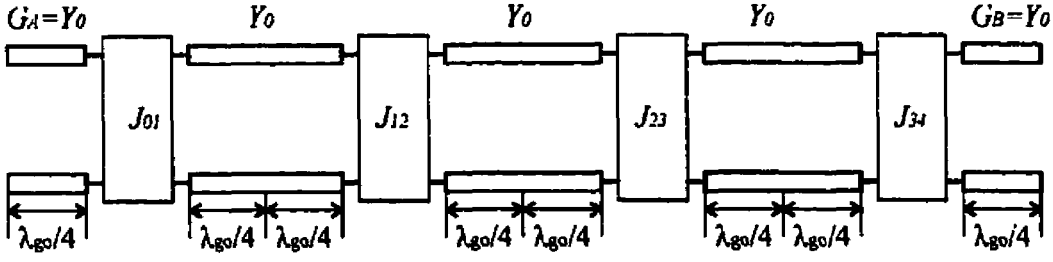

(a) cascaded J-inverter topology

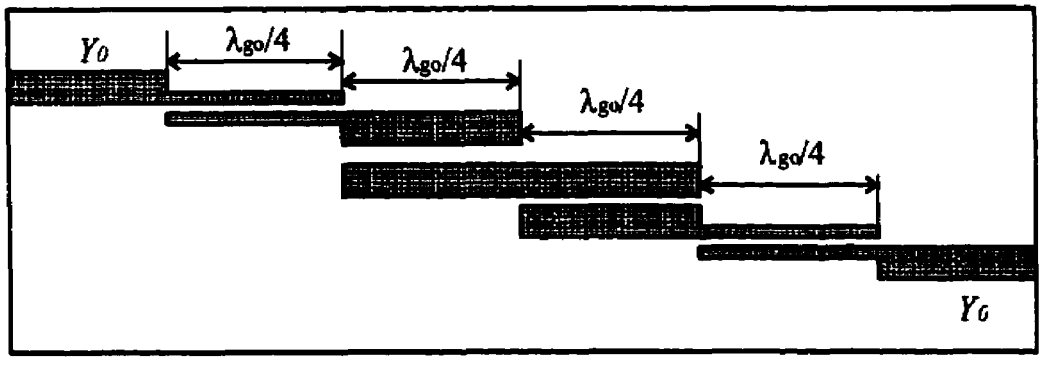

(b) microstrip band-pass filter layout

Figure 1.9 Equivalent topology and layout of a 3-stage microstrip bandpass filter

Figure 1.9(a) depicts the cascaded topology of a 3-stage transmission line band-pass filter, in which each line length between two adjacent J-inverter networks is equal to the

half-wavelength ($\lambda_{g0}/2$) at the central frequency (ω_0). Figure 1.9(b) illustrates the top-view of this 3-stage filter layout using the parallel-coupled microstrip line structure. To carry out the synthesis and design of such a filter, we can at first determine the values of each J-inverter susceptance ($J_{i,i+1}$) from the specified bandwidth (w) through Equation (1.15). According to Equation (1.12) and (1.13), we can then derive the even/odd characteristic impedances, Z_{0e} and Z_{0o}. Finally, the dimension of each coupled microstrip line section as in Figure 1.9 can be found from the design curves of Z_{0e} and Z_{0o} via strip/slot widths, calculated based on the two-dimensional (2-D) static or fullwave algorithm.

1.5 Purpose and Content of This Research Work

Following the well-maturated filter design theory described above, a large amount of printed and integrated microstrip or other transmission line filters have been studied and developed in the past decades for microwave and millimeter-wave integrated circuits and subsystems. This research work will be done towards the development of high-quality microstrip integrated low-pass and band-pass filters, which are realized on the basis of an aperture compensation technique and a newly proposed broad band-pass filtering mechanism.

As detailed in Section 1.2, the microstrip low-pass filter in general consists of several cascaded low- and high-impedance line sections. By widening its strip width in the relatively thin substrate, it is very easy to formulate the microstrip line with low impedance close to $10\ \Omega$ and realize a good equivalent quasi-lumped shunt capacitance. However, it seems problematic to construct the high-impedance microstrip line by simply reducing its strip width. In this case, the ohmic loss may be sharply raised as the strip width is narrowed down. Also, it may lead to the difficulty in precision fabrication of its strip conductor as well as parasitic effects caused by the strip configuration or

thickness. Meanwhile, the same problem may happen in the design of a parallel-coupled microstrip line (PCML) band-pass filter. To realize a tight coupling between two-coupled strips, the usual way is to reduce both strip and slot widths but it brings the rise-up of its conductance loss and also the difficulty in the formulation of extremely slot/strip widths.

In this research, an aperture compensation technique is proposed and applied for the innovative realization of low-loss microstrip line (ML) with the high characteristic impedance and the parallel-coupled microstrip line (PCML) with the tight coupling. With the use of a fullwave EM software developed in our laboratory, their electrical characteristics are investigated in terms of their equivalent circuit models. After the microstrip line section with backside aperture is characterized into a series inductive reactance and two shunt capacitive susceptance, a 5-stage microstrip lowpass filter is formulated and its filtering behavior is optimally designed by using the commercial HP Momentum software. A low-pass filter sample is then fabricated and measured based on the overall dimension of the optimized filter.

With the help of backside aperture on the ground plane, the coupling degree of the parallel-coupled microstrip line (PCML) structure is characterized into an equivalent J-inverter network and is found to rise up as the aperture width increases. By transforming the extracted circuit model into the scattering matrix, at first, we show that a single PCML structure with backside aperture itself can achieve a 2-pole band-pass electrical behavior relying on its extremely strong coupling. By inserting a uniform microstrip line between the two PCML parts, a novel multi-pole, ultra-broadband and miniaturized microstrip band-pass filter is proposed and its operating mechanism is discussed in terms of a unified equivalent circuit topology. By implementing a fullwave simulation over its whole layout with the use of the HP Momentum software, its optimized electrical behavior is well achieved with the bandwidth of about *70%* and

insertion loss lower than *–18dB*. This attractive filtering feature we predicted in theory is then confirmed by our measured results from a fabricated filter sample.

To realize a broadband microstrip band-pass filter with adjustable bandwidth (*BW*) and good harmonic suppression, a pair of capacitively open-end stub is introduced at the central location of the line resonator in such a way that its second-order resonant frequency is made to shift down towards its fundamental resonant frequency. After its filtering behavior is physically investigated under different stub lengths, a 4-pole broad microstrip bandpass filter is then optimally designed with much lower return loss (*<-20dB*) inside the broad passband and deep/wide upper-rejection band. The measured frequency response is obtained to verify our prediction in a wide frequency range.

REFERENCES:

(I.1) G. L. Matthaei, L. Young, and E. M. T. Jones, *Microwave Filters, Impedance-Matching Networks, and Coupling Structures*, Artech House, Norwood, 1980.

(I.2) T. Edwards, "Chapter 8: Passive MICs" in *Foundations for Microstrip Circuit Design*, (2nd Ed.), John Wiley & Sons, 1991.

(I.3) K. C. Gupta, R. Garg, I. Bahl and P. Bhartia, *Microstrip Lines and Slotlines*, (2nd Ed.), Artech House, Boston,1996.

CHAPTER II
APERTURE COMPENSATION TECHNIQUE: CONCEPT AND CHARACTERISTICS

2.1 INTRODUCTION

In this chapter, our discussion will be focused on the fundamental operating mechanism of an aperture compensation technique and its several attractive electrical features in making up a high-impedance microstrip line (ML) and also a tightly parallel-coupled microstrip line (PCML). First of all, the basic electrical performance of traditional ML and PCML, such as their characteristic impedance and conductance losses will be investigated on a basis of closed-form design equations. By introducing a backside aperture on the ground plane, we will then illustrate the electrical characteristics of the ML and PCML with different aperture dimensions in terms of their equivalent circuit models. It is realized with the help of the EM software developed by Lei Zhu and Ke Wu in our laboratory. In this case, a so-called "short-open calibration" (SOC) procedure is applied to extract effectively the circuit model parameters from the three-dimensional (3-D) method of moments (MoM) algorithm through the definition of two calibration standards, *short and open elements*.

2.2 TRADITIONAL MICROSTRIP LINE (ML)

Figure 2.1 depicts the cross-section of a traditional microstrip line with electrically finite conductor thickness (t), in which the signal conductor strip with width (W) is etched or formed on the top interface of a dielectric substrate with infinitely extended ground plane at its bottom interface. Due to its features such as low-cost mass manufacture, low profile, light weight and easy-to-realize integration, the microstrip

line structure has been widely used in the design of microwave and millimeter-wave integrated circuits (MMICs) and subsystems. In the following, we will illustrate its electrical characteristics through its three distinct parameters: effective dielectric constant (ε_{reff}), characteristic impedance (Z_0) and conductor/dielectric loss attenuation coefficients (α_c & α_d), which may be derived from several closed-form design equations under different dimensions and frequency ranges.

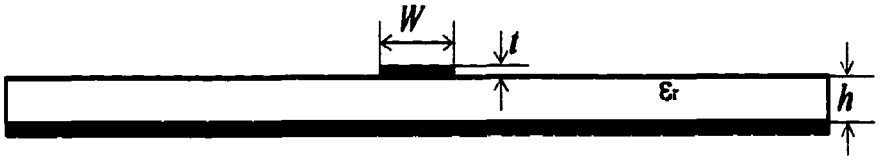

Figure 2.1 Cross-section of traditional microstrip line

Equation (2.1) and (2.2) are two closed-form equations used for characterization of its characteristic impedance (Z_0) and effective dielectric constant (ε_{reff}) as a function of its several dimensions under the quasi-static assumption,

$$Z_{0m} = \begin{cases} \dfrac{60}{\sqrt{\varepsilon_{re}}} \ln\left(\dfrac{8h}{W_e} + 0.25\dfrac{W_e}{h}\right) & \left(\dfrac{W_e}{h} \le 1\right) \\ \dfrac{120\pi}{\sqrt{\varepsilon_{re}}}\left\{\dfrac{W_e}{h} + 1.393 + 0.667 \ln\left(\dfrac{W_e}{h} + 1.444\right)\right\}^{-1} & \left(\dfrac{W_e}{h} \ge 1\right) \end{cases} \tag{2.1}$$

$$\varepsilon_{re} = \frac{\varepsilon_r + 1}{2} + \frac{\varepsilon_r - 1}{2} \begin{cases} \left(1 + 12\dfrac{h}{W_e}\right)^{-\frac{1}{2}} + 0.04\left(1 - \dfrac{W_e}{h}\right)^2 & \left(\dfrac{W_e}{h} \le 1\right) \\ \left(1 + 12\dfrac{h}{W_e}\right)^{-\frac{1}{2}} & \left(\dfrac{W_e}{h} \ge 1\right) \end{cases} \tag{2.2}$$

where W_e represents the effective strip width of the strip conductor by evaluating the effect of conductor thickness (t) and can be expressed as below.

$$\frac{W_e}{h}=\frac{W}{h}+\frac{1.25t}{\pi h}\begin{cases}\left(1+\ln\dfrac{4\pi W}{t}\right) & \left(\dfrac{W}{h}\le\dfrac{1}{2\pi}\right)\\ \left(1+\ln\dfrac{2h}{t}\right) & \left(\dfrac{W}{h}\ge\dfrac{1}{2\pi}\right)\end{cases} \tag{2.3}$$

Next, we will focus our attention here on the issue of evaluating quantitatively the total transmission loss for a uniform microstrip line with different strip width (W). In this case, this transmission loss is mainly attributed to the conductor strip loss and dielectric substrate loss, respectively, which are usually expressed as the two attenuation coefficients: α_c and α_d (dB/m). Equation (2.4) and (2.5) are the two closed-form equations used for effective evaluation of the two loss factors as a function of the microstrip line dimensions.

$$\alpha_c=\begin{cases}1.36A\dfrac{R_s}{hZ_{0m}}\dfrac{32-(W_e/h)^2}{32+(W_e/h)^2} & \left(\dfrac{W_e}{h}\le 1\right)\\ 6.1\times10^{-5}A\dfrac{R_sZ_{0m}\varepsilon_{re}}{h}\left[W_e\Big/h+\dfrac{0.667W_e/h}{W_e/h+1.444}\right] & \left(\dfrac{W_e}{h}\ge 1\right)\end{cases} \tag{2.4}$$

$$\alpha_d=\begin{cases}4.34\times120\pi\omega\varepsilon_0\varepsilon_r\tan\delta\dfrac{\varepsilon_{re}-1}{\sqrt{\varepsilon_{re}}(\varepsilon_r-1)} & \left(\dfrac{W}{h}\le\dfrac{1}{2\pi}\right)\\ 27.3\dfrac{\varepsilon_r}{\varepsilon_r-1}\dfrac{\varepsilon_{re}-1}{\sqrt{\varepsilon_{re}}}\dfrac{\tan\delta}{\lambda_0} & \left(\dfrac{W}{h}\ge\dfrac{1}{2\pi}\right)\end{cases} \tag{2.5}$$

where

$$A=1+\frac{h}{W_e}\begin{cases}\left(1+\dfrac{1.25}{\pi}\ln\dfrac{2h}{t}\right) & \left(\dfrac{W}{h}\le\dfrac{1}{2\pi}\right)\\ \left(1+\dfrac{1.25}{\pi}\ln\dfrac{4\pi W}{t}\right) & \left(\dfrac{W}{h}\ge\dfrac{1}{2\pi}\right)\end{cases} \tag{2.6}$$

Figure 2.2 illustrates the calculated characteristic impedance (Z_0) and effective dielectric constant (ε_{reff}) as a function of strip width (W) under the assumed strip thickness t=*0.1* and *0.7mil*, respectively. It can be well observed that Z_0 tends to gradually rise up as W decreases from *30.0mil* to *5.0mil* and rapidly go up as an approximately exponential function of W as W is further reduced smaller that *5.0mil*. Meanwhile, the parameter, ε_{reff}, seems to slightly fall down as W decreases since the electric field distribution underneath the strip conductor is oriented towards the upper air region and/or dielectric interface. On the other hand, it always needs to be considered in the static or fullwave characterization of a high-impedance microstrip line with narrow strip width (W) that the conductor thickness affects its transmission properties.

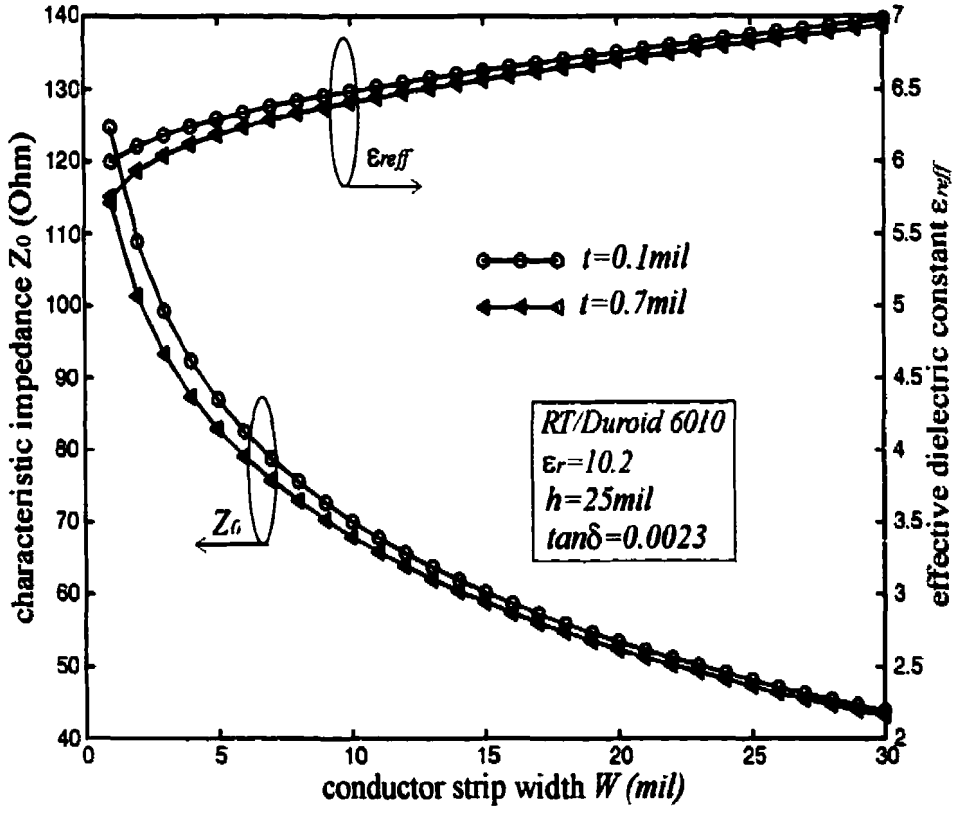

Figure 2.2 Characteristic impedance (Z_0) and effective dielectric constant (ε_r) as a function of strip width (W) under the strip thickness t=0.1mil & 0.7mil.

From Figure 2.2, we can clearly find that both Z_0 and ε_{reff} tends to go down slightly as the conductor thickness (t) increases from *0.1mil* to *0.7mil*. Especially in the case of a very narrow width (*W=1mil*), Z_0 falls down from *124.7 Ohm* to *114.2 Ohm* and ε_{reff} is slightly decreased from *5.99* to *5.75* as *t* increases from *0.1mil* to *0.7mil*. We can further imagine that the existence of finite conductor thickness (*t*), the rapid incremental of Z_0 and the strip configuration at its two edges may lead to some difficulties in the realization of a high-impedance microstrip line with the specified characteristic impedance. On the other hand, the obtained maximum Z_0=*125 Ohm* is still far away from the value regarding to the large equivalent series inductance, which is required in the design of microstrip lowpass filter as discussed in Chapter I.

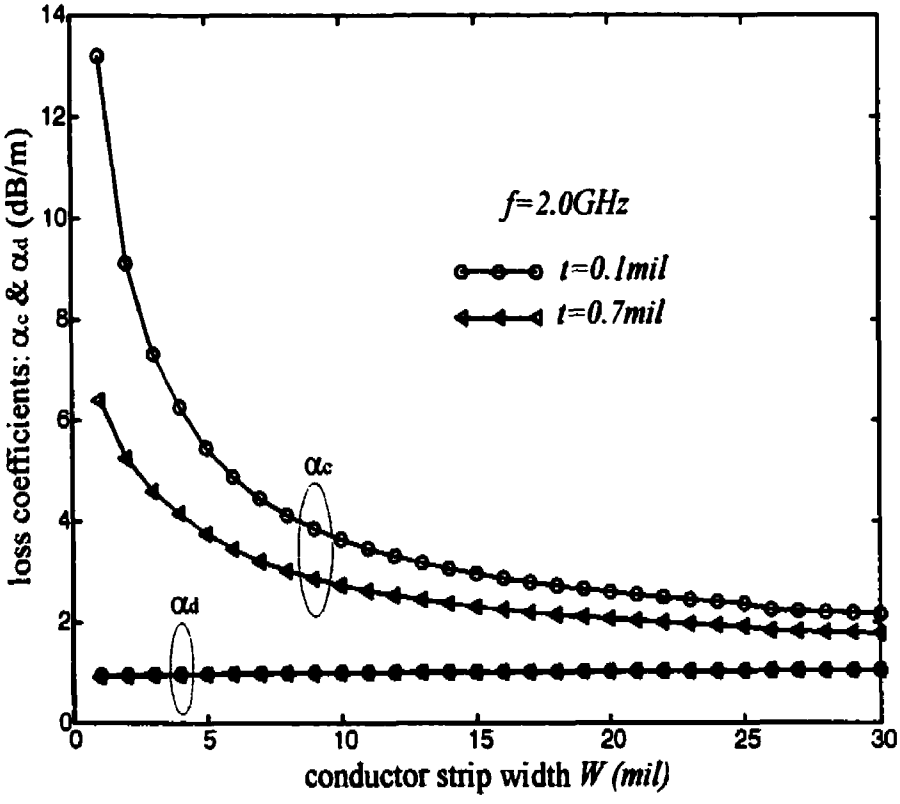

Figure 2.3 Loss attenuation coefficients (α_c and α_d) as a function of strip width (*W*) at the operating frequency, f=2.0GHz, in this example.

Figure 2.3 illustrates the calculated conductor and dielectric substrate losses (α_c & α_d) as a function of strip width (W) at the operating frequency of f=*2.0 GHz* in this example. First of all, we can observe from our calculated results that the conductor loss coefficient (α_c) is definitely higher than its dielectric counterpart (α_d) in the low and high frequency and gains a rapid shift-up as W decreases. Also, the conductor loss tends to gradually fall down as the strip thickness (t) is raised from *0.1mil* to *0.7mil*. Accordingly, we can speculate that the conductor loss may be reduced to a great extent by thickening the strip conductor.

However, it may bring out the difficulty in achieving the high characteristic impedance (*150 ~ 300 Ohm*) of a microstrip line, which may be required in the design of microstrip lowpass filter with a sharply changed high-rejection behavior. On the other hand, both conductor and dielectric substrate losses rise up slightly as the frequency (f) increases but the former seems always higher than the latter regardless of operating frequency and strip dimension. Until now, it can be well understood that the total transmission loss of a uniform microstrip line with high impedance is mainly contributed by its conductor loss. In the following, an aperture compensation technique is proposed to construct a low-loss and high-impedance microstrip line with relatively large strip width (W).

2.3 APERTURE-COMPENSATED MICROSTRIP LINE (AC-ML)

Figure 2.4 shows the cross-section of the proposed aperture-compensated microstrip line (AC-ML) to be characterized here for the effective enhancement of its characteristic impedance under the condition of a low conductor loss. By removing a certain part of its ground plane underneath the strip conductor, the capacitive coupling between the strip conductor and ground plane may be softened to a great extent so that the high-impedance microstrip line can be designed. It can be understood that its

characteristic impedance (Z_0) can achieve an extremely high level by extending further its aperture width according to the specified series inductance in the filter design.

In the meantime, the existence of such a backside aperture allows an easy realization of a much low conductor loss since its strip width may be kept much larger than its strip thickness (t) and also comparable to the substrate thickness (h). Unfortunately, no available two-dimensional (2-D) EM software to date is developed for static or fullwave characterization of this AC-ML transmission line structure with backside aperture in terms of its characteristic impedance (Z_0) and effective dielectric constant (ε_{reff}).

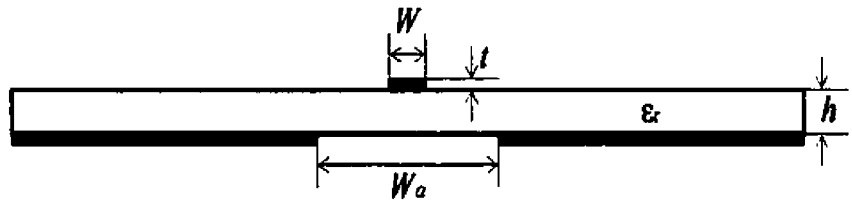

Figure 2.4 Cross-section of aperture-compensated microstrip line (AC-ML)

In this work, a fullwave three-dimensional (3-D) method of moments (MoM) algorithm will be applied for characterization of a two-port AC-ML circuit with finite line length, which is excited at its two sides by the low-impedance microstrip lines without backside aperture. Furthermore, a numerical de-embedded procedure, called by "short-open calibration (SOC)", is carried out to extract or de-embed effectively its equivalent circuit model or network, which can account for all the physical effects such as the frequency dispersion and the discontinuity happened at the interface between two adjacent microstrip line sections.

Figure 2.5(a) illustrates the geometrical layout of the two-port aperture-compensated microstrip line (AC-ML) structure with two external microstrip lines. Figure 2.5(b) depicts its unified equivalent circuit model with the parameters of a series inductive reactance (jX_L) and two shunt capacitive susceptances (jB_L). Especially, in the case of

extremely low frequency (f) or electrically much short line length (l_L), these parameters can be perfectly perceived as the quasi-lumped series inductance (L) and quasi-lumped shunt capacitance (C), respectively.

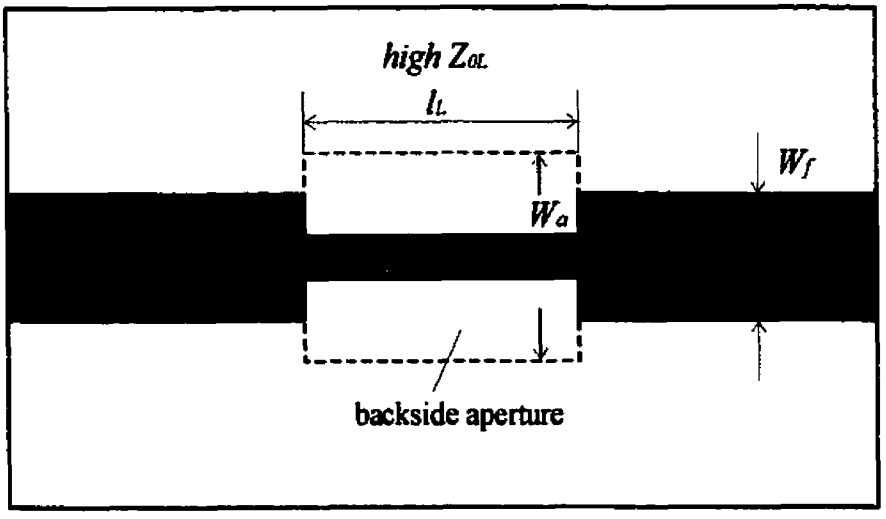

(a) geometrical layout

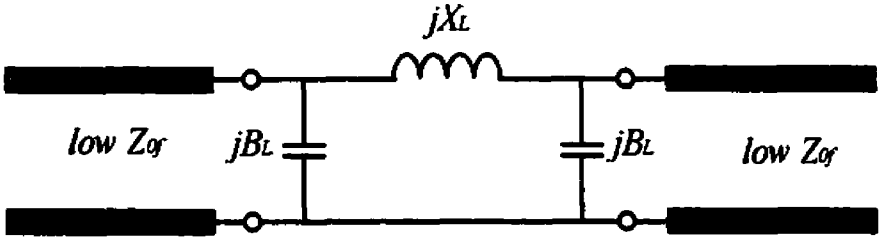

(b) equivalent circuit model

Figure 2.5 Geometrical layout and its equivalent circuit model of an aperture-compensated microstrip line (AC-ML) structure to be studied.

In the following, our discussion will start with the theoretical investigation of its quasi-lumped electrical properties over low frequency range in which its total line length is electrically much shorter than the guided wavelength ($l_L \ll \lambda_g$). Next, the circuit model parameters are effectively transformed into their equivalent 3-D defined characteristic impedance in order to clearly illustrate its high impedance with the help of the backside

aperture on the ground plane. Furthermore, its frequency-distributed electrical properties will be studied on a basis of extracted circuit model parameters (jX_L & jB_L) over a wide frequency range.

At the low frequency (f=*1.0GHz* in this case), equivalent series inductive reactance (jX_L) and two shunt capacitive susceptances (jB_L) can be characterized as their corresponding quasi-lumped series inductance and shunt capacitance (L & C). Figure 2.6(a) and (b) depict the equivalent circuit parameters as a function of the backside aperture width (W_a) versus different line length (l_L=*0.6, 1.2, 1.8, 2.4, 3.0mm*), obtained from the above-mentioned MoM-based EM software.

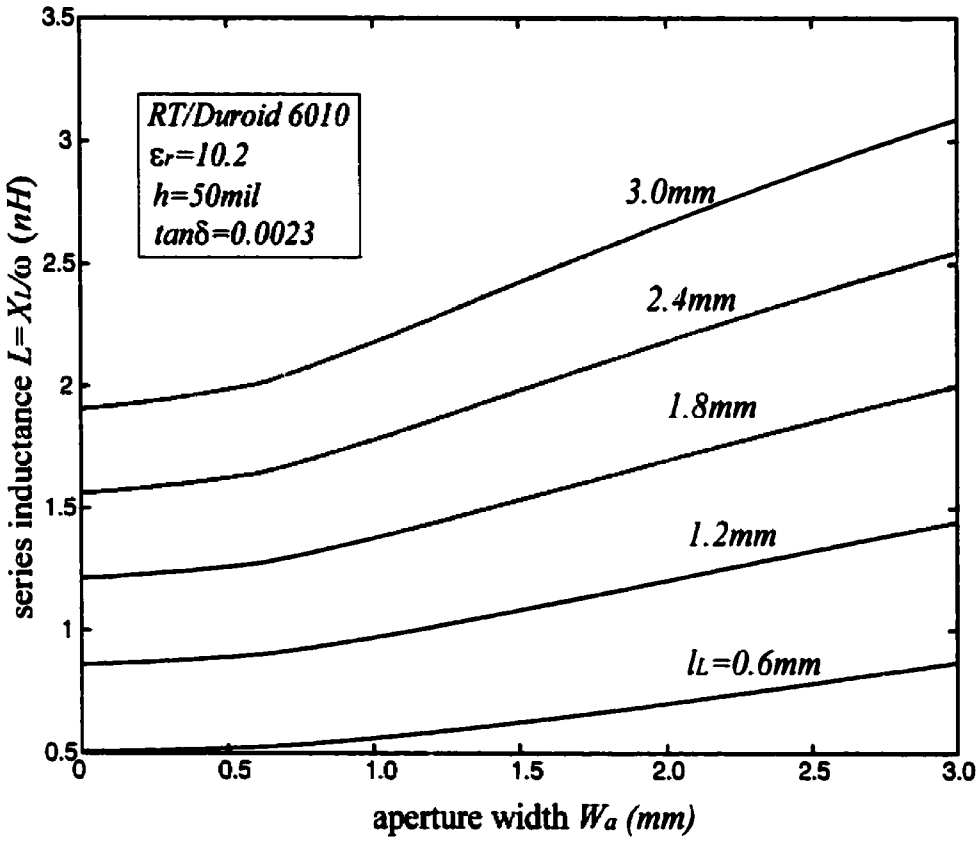

(a) series inductance

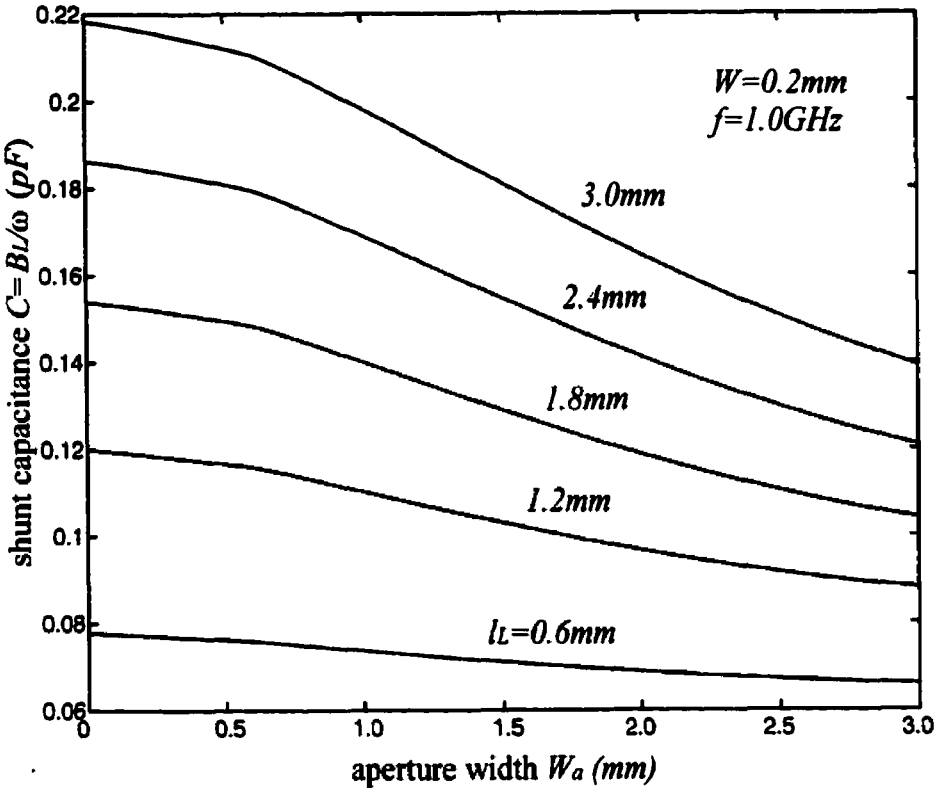

(b) shunt capacitance

Figure 2.6 Extracted equivalent series inductance ($L=X_L/\omega$) and shunt capacitance ($C=B_L/\omega$) as a function of aperture width (W_a).

First of all, we can find from Figure 2.6(a) that the series inductance (L) is changed in an approximately linear increment with the line length (l_L). It can be explained that the equivalent series inductance of a conductor line is linearly proportional to its total line length. The calculated shunt capacitance (C) tends to shift up as l_L increases, showing the existence of an additional quasi-lumped circuit parameter for a transmission line.

Now, our attention is being directed towards the electrical characteristics of a backside aperture according to the purpose of this research. As the aperture width (W_a) is enlarged to the order of the strip width (W), the quasi-lumped series inductance (L) seems to be slowly incremental and the quasi-lumped shunt capacitance (C) is at the

high level. As W_a is further increased beyond the range of *2~3W*, *L* rises up in a linear manner and C rapidly falls down. By observing closely Figure 2.6(a) and (b), we can then quantitatively find that *L* is raised by *65%* and *C* is reduced by *40%* for all the five cases as W_a increases from *0* to *3.0mm*. At l_L=*2.4mm*, *L* is seen to rise up from *1.56* to *2.55nH* while C drops from *0.19* to *0.12pF*.

Now, a very effective extraction technique is developed to derive the characteristic impedance (Z_0) and effective dielectric constant (ε_{reff}) of the uniform AC-ML transmission line from the calculated circuit parameters, jX_L and jB_L, of a two-port AC-ML structure with finite line length (l_L). Strictly speaking, the calculated jX_L and jB_L, as illustrated in Figure 2.6(a) and (b), represent its total electrical properties of such a two-port AC-ML structure. These circuit parameters also include the parasitic discontinuity effects happened at the interface between the microstrip feed line and AC-ML line in addition to the actual transmission property of the uniform AC-ML line.

The key issue is how to separate completely the two groups of circuit parameters, corresponding to the AC-ML and the parasitic discontinuity, respectively, in order to de-embed or extract the circuit parameters of the uniform AC-ML line. A two-port AC-ML structure with different line lengths, l_a and l_b, will be employed to undertake this task under the assumption that the parasitic discontinuity effect at the interface is kept unchanged regardless of the AC-ML line length.

(a) layout (b) equivalent circuit model

Figure 2.7 Layout and equivalent circuit model of an AC-ML with line length (l_a)

Figure 2.7 depicts the layout and its equivalent circuit model of a two-port AC-ML structure with a short line length, l_a, with reference to Figure 2.5. Its network parameters, jX_{La} and jB_{La}, have been accurately characterized with the use of the SOC technique in the 3-D MoM and they are plotted in Figure 2.6(a) and (b). These parameters include the electrical characteristics of the parasitic interface discontinuity and also the uniform AC-ML line with a short line length (l_a). This short AC-ML acts as a standard element and allows us extracting the circuit parameters of the uniform AC-ML line from the characterization of a long AC-ML structure. It is realized by comparing the two equivalent networks, regarding to the AC-ML with two line lengths.

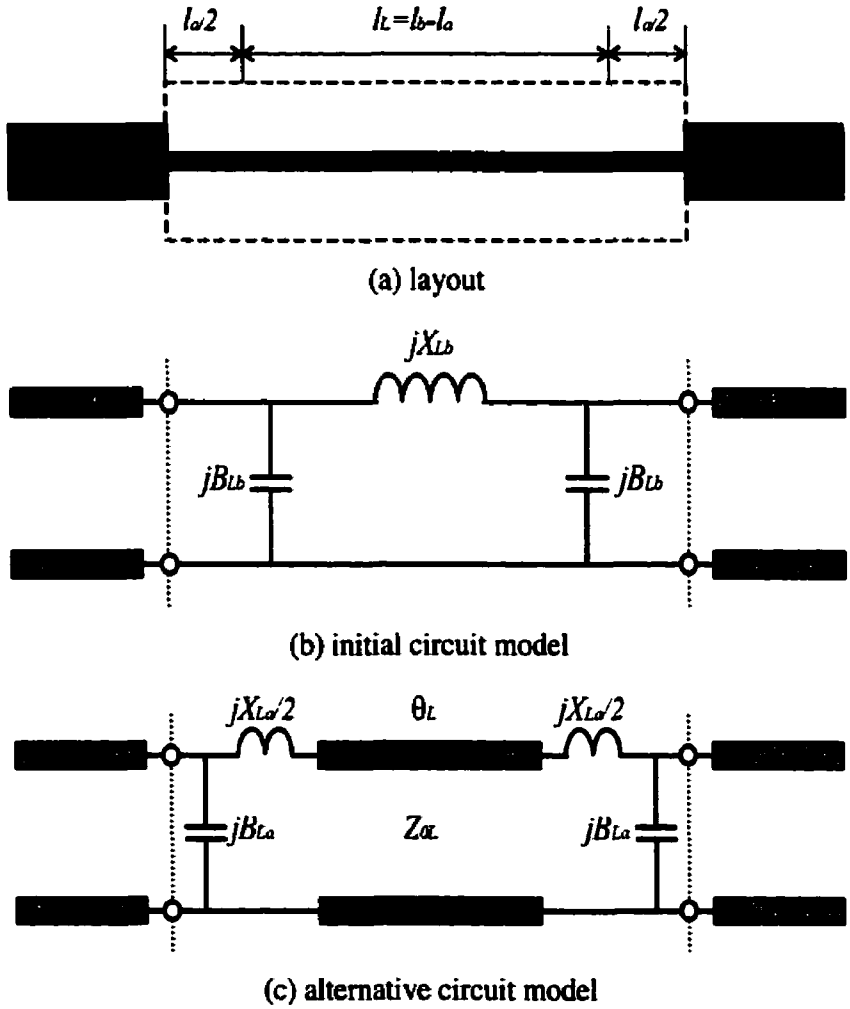

Figure 2.8 Layout and equivalent circuit model of an AC-ML with line length (l_b)

Figure 2.8(a) and (b) illustrate the layout and its initial equivalent circuit model of a two-port AC-ML structure with a long line length, L_b ($>L_a$). The difference between two line lengths, $l_L=l_b-l_a$, represents the line length of the uniform AC-ML line of our interest, located at the central part in Figure 2.8(a), which is used for parameter extraction of the transmission properties of the AC-ML line.

Figure 2.8(c) is its alternative equivalent circuit model arranged for carrying out the extraction procedure. This model is made up of two half parts of a short AC-ML networks as in Figure 2.7(b) at its two sides and a uniform transmission line with the characteristic impedance (Z_{0L}) and electrical line length (θ_L) at its central part. Because of the equivalence of these two different equivalent networks for an identical AC-ML structure, the interrelation between two groups of circuit parameters, as depicted in Figure 2.8(a) and (b), can be analytically derived. This relation allows us expressing Z_0 and ε_{reff} as a function of equivalent series reactance (jX_{La} & jX_{Lb}) and shunt susceptance (jB_{La} & jB_{Lb}).

Due to the symmetry of these two-port networks as shown in Fig. 2.8(b) and (c), we can divide the whole initial or improved network into two identical parts at their central or symmetrical location. Under the odd or even excitation impressed at the two ports of these networks, their central location represents the perfect short- or open-circuit terminal. So, the half part of the two networks in Fig. 2.8(b) and (c) can be used to express the interrelation between the parameters of these two networks under their identity or equivalence. At the case of odd excitation (short-circuit),

$$jB_{Lb}+\frac{1}{jX_{LB}/2}=jB_{La}+\frac{1}{jX_{La}/2+jZ_0\tan(\theta/2)} \tag{2.7a}$$

On the other hand, the second equation can be obtained at the case of even excitation (open-circuit),

$$jB_{Lb} = jB_{La} + \frac{1}{jX_{La}/2 + Z_0 / j\tan(\theta/2)} \qquad (2.7b)$$

In final, we can analytically derive a pair of closed-form equations as below, linking the two network parameters together.

$$Z_0 \tan(\theta_{0L}/2) = \frac{X_{Lb}}{2-(B_{Lb}-B_{La})X_{Lb}} - \frac{X_{La}}{2} \quad \text{(odd excitation)} \qquad (2.8a)$$

$$Z_0 / \tan(\theta_{0L}/2) = \frac{1}{(B_{Lb}-B_{La})} - \frac{X_{La}}{2} \quad \text{(even excitation)} \qquad (2.8b)$$

where

$$\theta_{0L} = \frac{2\pi f \sqrt{\varepsilon_{reff}}}{c} l_L \qquad (c\text{: light speed}) \qquad (2.9)$$

With the use of these equations, we can derive the equivalent transmission properties of the AC-ML line with the finite line length, l_L, with reference to the 3-D MoM extracted network parameters as in Figure 2.6(a) and (b).

Table 2.1 illustrates the equivalent characteristic impedance (Z_0) and effective dielectric constant (ε_{reff}) of the AC-ML line versus aperture width (W_a). In this case, the short and long line lengths are chosen as l_a=*0.6mm* and l_b=*3.0mm*, respectively, so that the uniform AC-ML line length is equal to l_L=*2.4mm*.

In the case of W_a=*0.2mm*, both Z_0 and ε_{reff} is very close to those obtained from 2-D static definition of a uniform microstrip line (ML) and their difference is about 5.0%. This result provides a good verification on the AC-ML transmission parameters, obtained from Equation (2.8) and Equation (2.9).

Table 2.1 MoM-extracted characteristic impedance (Z_o) and effective dielectric constant (ε_{reff}) of AC-ML line versus aperture width (W_a) with those of 2-D static ML ($W=0.2mm$, $f=1.0GHz$, $l_a=0.6mm$ and $l_b=3.0mm$)

	2-D static	3-D MoM definition							
$W_a(mm)$	0.0	0.2	0.6	1.0	1.4	1.8	2.2	2.6	3.0
$Z_{oL}(ohm)$	76.645	73.871	77.426	83.623	91.252	99.544	108.13	116.79	125.35
ε_{reff}	6.4721	6.8256	6.8905	6.8967	6.7677	6.5116	6.1755	5.8085	5.4481

From Table 2.1, we can well observe that Z_o rises up slowly and then in a very rapid manner as W_a increases. In the meantime, ε_{reff} tends to fall down slowly and then rapidly in the opposite variation with Z_o. From Figure 2.2, we can find that Z_o is increased to a limited value of about *115.0Ohm* at the expense of a high conductor loss as discussed before even though the strip width (W) is reduced to the value of *0.1mil=0.0025mm*.

Also, we can see here that Z_o achieves the high value of about *125Ohm* at the fixed $W=0.2mm$ under the wide aperture ($W_a=3.0mm$). It can be well understood that the ohmic loss is much lower than that for the ML with $W=0.1mil$ and also its Z_o can be greatly raised by extending further the aperture width (W_a). On the other hand, ε_{reff} goes down from *6.83* to *5.45* as W_a increases from *0.2 to 3.0mm*, showing that the EM field is gradually distributed into the air region as the aperture is widened.

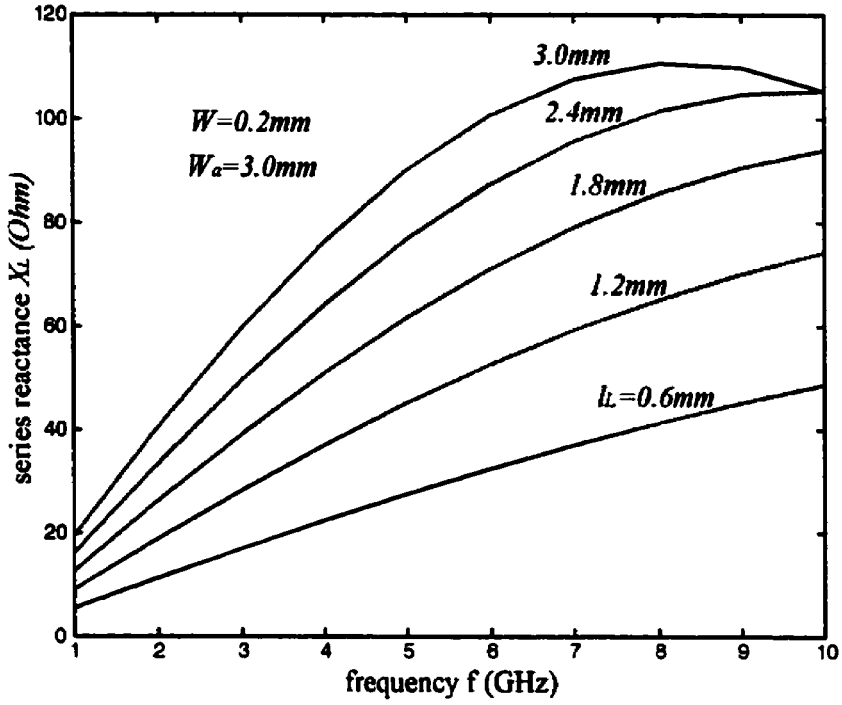

(a) series reactance (jX_L)

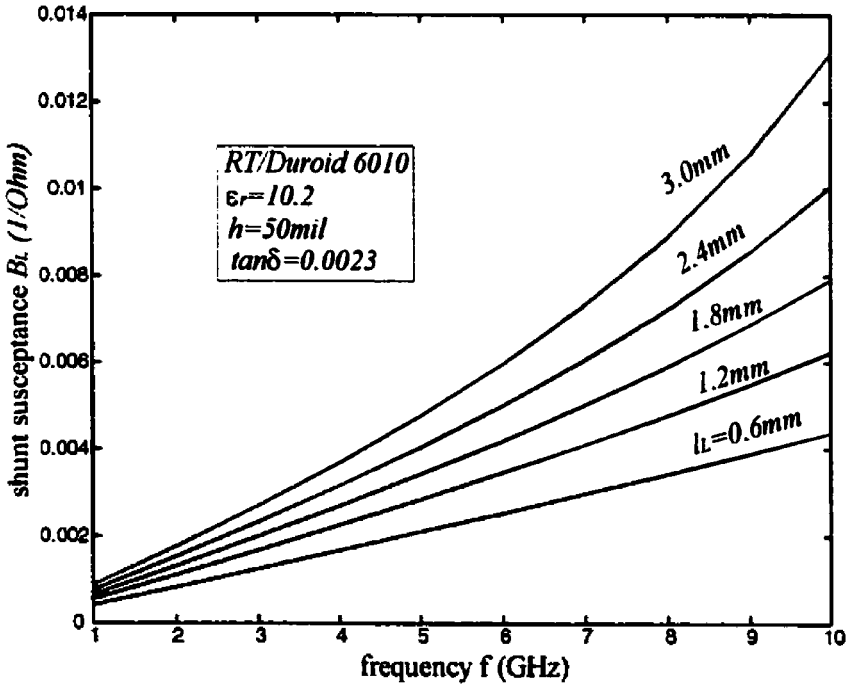

(b) shunt susceptance (jB_L)

Figure 2.9 Extracted equivalent series reactance (jX_L) and shunt susceptance (jB_L) as a function of operating frequency (f) under the width: W_a=3.0mm.

Until now, we have studied the quasi-lumped or static circuit parameters of the proposed AC-ML structure at low frequency. In fact, its electrical property tends to be visibly frequency-distributed or dependent as the operating frequency increases. Figure 2.9(a) and (b) depict the extracted frequency-dependent series reactance (jX_L) and shunt susceptance (jB_L) versus line length (l_L) in the case of a wide aperture width (W_a=*3.0mm*) over a wide frequency range (*f=1.0* to *10.0 GHz*). At low frequency (<*4.0GHz*) as discussed above, jX_L goes up with l_L and increases linearly with *f*.

At the same time, jB_L slightly shifts up with l_L and also linearly increases with *f*. As frequency (*f*) increases beyond *4.0GHz*, we can observe from Figure 2.9(a) and (b) that both jX_L and jB_L tend to go down and up slightly in an incrementally nonlinear manner. This nonlinear variation represents the frequency-distributed electrical behavior of this AC-ML structure at high frequency and can be attributed to the fact that the line or aperture length (l_L) occupies a few portion of its operating guided wavelength. As a result, this nonlinear dispersion factor should be taken into account in the accurate design of low-pass filter because it may degrade the high-stop filtering behavior at the high frequency range to some extent.

2.4 Traditional Parallel-Coupled Microstrip Line (PCML)

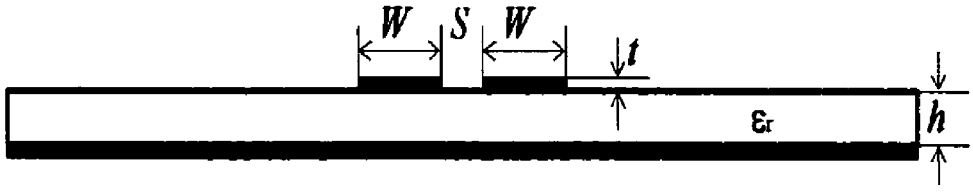

Figure 2.10 Cross-section of a parallel-coupled microstrip line (PCML)

Figure 2.10 depicts the cross-section of a traditional parallel-coupled microstrip line (PCML), in which two strip conductors with the identical width (*W*) are separately placed and coupled together in a close proximity through a small space gap with the

width (S). This PCML structure has widely been utilized as a basic element in the design of several microstrip integrated circuits such as microstrip band-pass filter and directional coupler.

Because of the EM coupling of two strip conductors, the PCML can support two independent quasi-TEM propagation modes with two different characteristic impedances. In the symmetrical PCML discussed here, these two modes are called as even and odd quasi-TEM modes, respectively, due to even and odd symmetry of their field configuration with respect to the central or symmetrical plane of this PCML. As usual, its electrical property can approximately but effectively be evaluated with the help of their characteristic impedances, e. g., Z_{0e} & Z_{0o}.

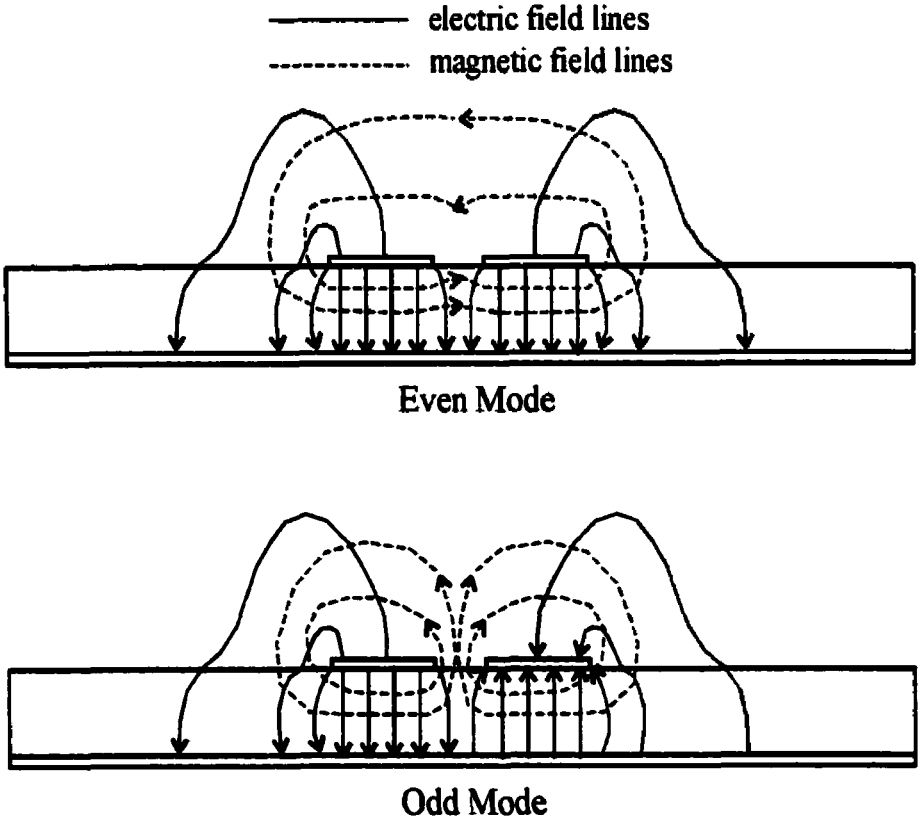

Figure 2.11 Electric and magnetic filed configuration of even and odd modes for a parallel-coupled microstrip line (PCML).

Figure 2.11 illustrates electric and magnetic field configurations of the even and odd quasi-TEM modes for a PCML line. Due to the strongly capacitive coupling degree between either of two strip conductors and the infinite ground plane, a large portion of electric field is confined in an almost equal manner over the dielectric region underneath two strip conductors as shown in Figure 2.11. In the case of the even mode, the electric field lines are oriented from both strip conductors to the ground plane in the form of an even symmetrical configuration. In the case of the odd mode, however, the electric field lines at the left-hand part have an orientation from its strip conductor to the ground plane, while those at the right-hand part have a reverse orientation from the ground to the other strip conductor.

Also, we can find from Figure 2.11 that the magnetic field lines in both cases are always distributed in the orthogonal orientation with the electric field lines. On the other hand, we can well imagine that the central plane between two strip conductors represent the perfectly magnetic wall and electric wall, respectively, in the case of even and odd modes.

The analysis of this PCML structure in general starts with the static or fullwave modeling of its characteristic impedances (Z_{0e} & Z_{0o}) and effective dielectric constant (ε^{e}_{reff} & ε^{o}_{reff}) for the two modes. To simplify the whole analysis procedure and also look into the electrical properties of a uniform PCML line, a group of close-formed design equations has been well developed in the early stage and will be employed here to investigate initially its two-dimensional (2-D) electrical behavior. These equations are deduced under the static assumption and derived in terms of a variety of equivalent mode capacitances for the two quasi-TEM modes.

By looking at the field configuration of even mode as shown at the top of Figure 2.11, it can be understood that the even-mode capacitance (C_e) consists of three capacitances,

$$C_e = C_p + C_f + C_f^{'} \tag{2.10}$$

in which, C_p denotes the parallel plate capacitance between the strip conductors and the ground plane and C_f is the fringe capacitance at the outer edge of a single uniform microstrip line.

$$C_p = \varepsilon_0 \varepsilon_r W/h \tag{2.11}$$

$$2C_f = \sqrt{\varepsilon_{reff}}/(cZ_o) - C_p \tag{2.12}$$

In Equation (2.10), the term $C_f^{'}$ stands for an additional capacitance contributed by the existence of the other microstrip line in proximity and can also be expressed in a closed-form equation [Ref. II.1],

$$C_f^{'} = \frac{C_f}{1 + A(h/S)\tanh(10S/h)}\left(\frac{\varepsilon_r}{\varepsilon_{reff}}\right)^{0.25} \tag{2.13}$$

where

$$A = \exp[-0.1\exp(2.33 - 1.5W/h)]$$

Meanwhile, the odd-mode capacitance (C_o) can be decomposed into five constituents,

$$C_e = C_p + C_f + C_f^{'} + C_{gd} + C_{ga} = 0.5C_{os} + C_{cps} \tag{2.14}$$

The term C_{os} denotes the odd-mode capacitance of a coupled stripline with the same strip and gap widths as the PCML line, e. g., W & h can be expressed in a closed-form as in [Ref. II.1],

$$C_{as} = 4\varepsilon_0\varepsilon_r \frac{K(k_o)}{K(k_o')} \tag{2.15}$$

Here, $K(k_o)$ and $K(k_o')$ denote the elliptic function and its complement with two variants of k_o and $k_o' = \sqrt{1-k_o^2}$, respectively, and their ratio $K(k_o)/K(k_o')$ can be written down,

$$\frac{K(k_o)}{K(k_o')} = \frac{\pi}{ln\left[2\left(1+\sqrt{k_o'}\right)/\left(1-\sqrt{k_o'}\right)\right]} \quad (0<k<0.707) \tag{2.16a}$$

$$\frac{K(k_o)}{K(k_o')} = \frac{ln\left[2\left(1+\sqrt{k_o}\right)/\left(1-\sqrt{k_o}\right)\right]}{\pi} \quad (0.707<k<1) \tag{2.16b}$$

where

$$k_o = tanh\left(\frac{\pi W}{4h}\right) coth\left[\frac{\pi}{4}\left(\frac{W+S}{h}\right)\right] \tag{2.17}$$

Alternatively, the term C_{cps} in Equation (2.14) represents the capacitance of the corresponding coplanar stripline (CPS) in the half space.

$$C_{cps} = \varepsilon_0 \frac{K(k')}{K(k)} \qquad \left(k = \frac{S}{S+2W}\right) \tag{2.18}$$

Thereafter, the even- and odd-mode characteristic impedances, Z_{0e} & Z_{0o}, can be expressed in the closed-form equations as below in terms of the above-obtained capacitances, C_e & C_o, as well as those in the air space ($\varepsilon_r=1$), C_{e0} & C_{o0}.

$$Z_{0e} = \left(c\sqrt{C_e C_{e0}}\right)^{-1} \tag{2.19a}$$

$$Z_{0o} = \left(c\sqrt{C_o C_{o0}}\right)^{-1} \tag{2.19b}$$

Otherwise, the effective dielectric constants (ε^{e}_{reff} & ε^{o}_{reff}) for the two modes can also be obtained from the above capacitances by using the relations,

$$\varepsilon^{e}_{reff} = C_e / C_{e0} \tag{2.20a}$$

$$\varepsilon^{o}_{reff} = C_o / C_{o0} \tag{2.20b}$$

Figure 2.12(a) and (b) depict the calculated characteristic impedances (Z_{0e} & Z_{0o}) and effective dielectric constant (ε^{e}_{reff} & ε^{o}_{reff}) of the even and odd modes as a function of *W/h*. As *W/h* increases at the fixed *S/h*, Z_{0e} & Z_{0o} tend to rapidly fall down and ε^{e}_{reff} & ε^{o}_{reff} appear to slightly go up. As *S/h* increases, we can observe that Z_{0e} & Z_{0o} are shifted down and up, respectively, in an oppositely variant manner. Since the difference of Z_{0e} & Z_{0o} points to the coupling characteristic of two coupled lines, the above results illustrate that the coupling strength of the PCML can be enhanced to a great extent by reducing the slot width (*S*) and the strip width (*W*) for a given dielectric substrate.

However, some potential parasitic effects such as the conductor loss and strip thickness and/or configuration may become too large to be ignored as *W* and *S* decreases to an extremely small extent. As detailed in the case of a microstrip line, these parasitic effects adversely affect the electrical characteristic of this PCML and also bring up the difficulty in the fabrication issue.

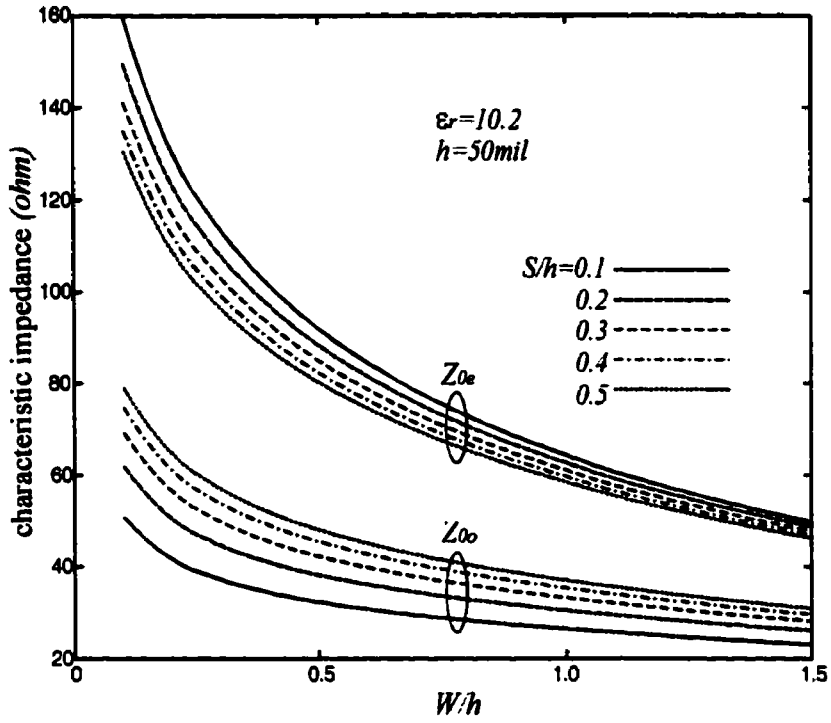

(a) characteristic impedance

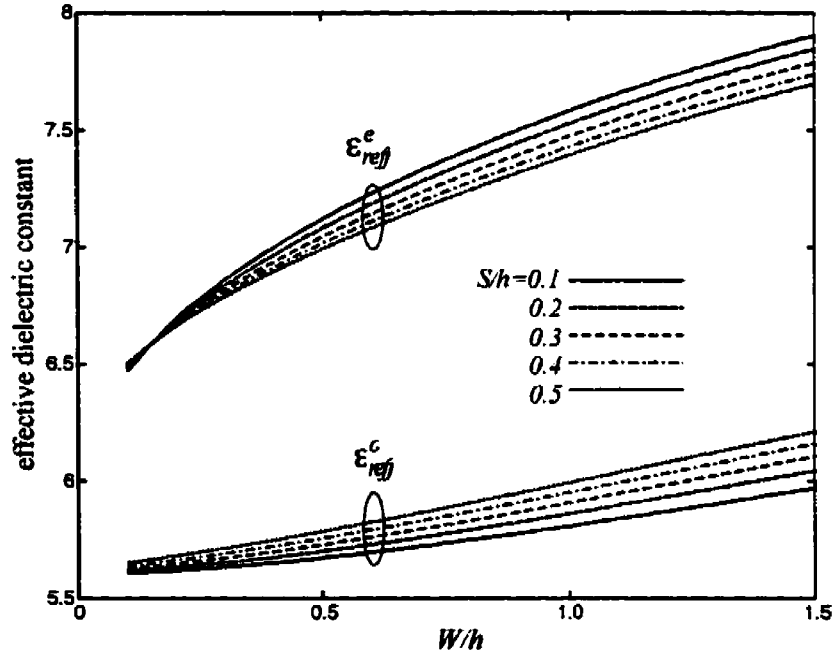

(b) effective dielectric constant

Figure 2.12 Characteristic impedance and effective dielectric constant of the even- and odd-modes as a function of *W/h*.

2.5 Aperture-Compensated Parallel-Coupled Microstrip Line (AC-PCML)

It has been well known that a tight coupling between the two coupled lines of the PCML is always required in the design of broadband band-pass filters and broadband directional couplers. Due to its potentially high conductor loss and also difficulty in fabrication mentioned above, the traditional PCML structure is probably difficult to be directly used for carrying out such a task as a key element in those planar integrated circuits. An alternative procedure proposed here is to enhance this coupling by removing out a partial portion of the ground plane to form a backside aperture underneath the coupled strip conductors. This aperture allows reducing effectively the extremely strong coupling happened between the two parallel plates, representing the strip conductors and the ground plane, respectively. As a result, it can be physically imagined that the coupling between the two strip conductors gains a great enhancement.

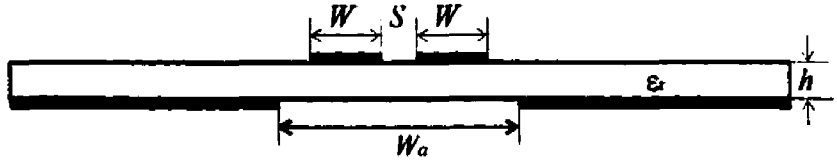

(a) cross-section

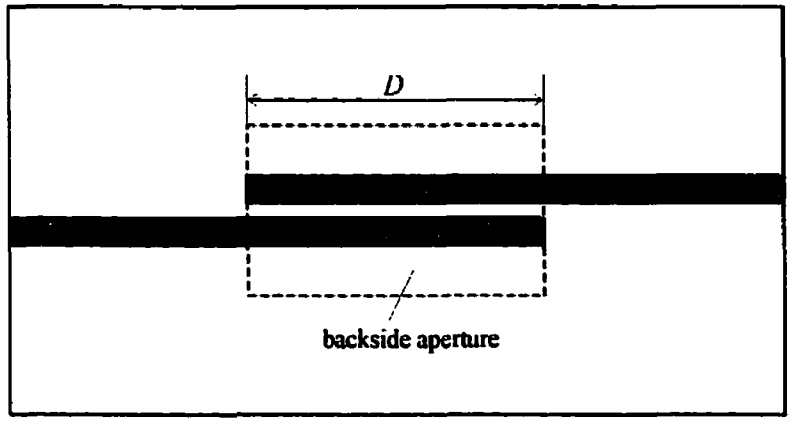

(b) top-view

Figure 2.13 Cross-section and top-view of the aperture-compensated parallel-coupled microstrip line (AC-PCML) structure to be studied.

In the following, its coupling characteristics will be investigated and discussed on a basis of calculated circuit parameters, obtained from the EM software developed by Lei Zhu and Ke Wu. Figure 2.13(a) depicts the cross-section of the aperture-compensated parallel-coupled microstrip line (AC-PCML) structure to be studied, in which a backside aperture with the width (W_a) is placed underneath two strip conductors. Figure 2.13(b) is the top-view of the two-port AC-PCML structure terminated by two external microstrip lines with the uniform strip width (W). Basically, the uniform AC-PCML line can be characterized with the use of even- and odd-mode approach discussed above. But, it prefered to take into account the whole 3-D AC-PCML layout as in Figure 2.13(b) in the accurate analysis due to the potentially serious discontinuity effect existing at the interface between the external lines and coupled-line with a backside aperture.

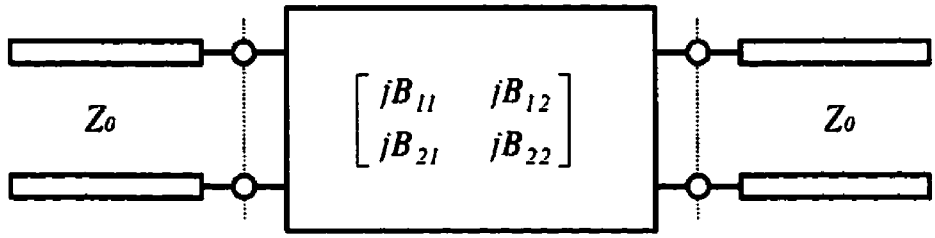

(a) Y-matrix model

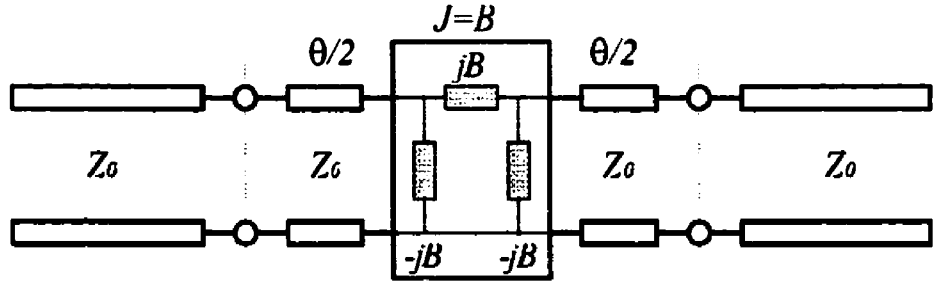

(b) J-inverter model

Figure 2.14 Two sets of unified equivalent circuit model used for characterization of the two-port AC-PCML structure

To undertake this task, the above-mentioned EM software in our laboratory is used here to extract effectively the unified equivalent circuit model of such an AC-PCML structure from the fullwave MoM calculations. This unified model is formed without any pre-assumption and can account for all the physical effects happened in the two-port 3-D AC-PCML structure such as the coupling behavior of two uniform coupled lines with backside aperture and the interface discontinuity effect between the external microstrip lines and AC-PCML line.

Figure 2.14(a) depicts the equivalent two-port admittance- (Y-) matrix circuit model of this AC-PCML structure. Due to its geometrical symmetry, there are in fact only two independent model parameters, $Y_{11}=Y_{22}$ and $Y_{12}=Y_{21}$. In this case, the strip width (W) is kept as a partial fraction of its dielectric substrate (h) and wavelength (λ), so that the conductor loss can be achieved at a very low level. The other loss factor in this structure may be radiation-related, mainly caused by the backside aperture. Fortunately, this radiation-related loss seems so small that it can be ignored in this structure due to much low excitation efficiency from the coupled-strip conductors to backside aperture.

As a result, the loss-related parameters will be completely ignored in the following in order to focus our attention on the AC-PCML's coupling characteristics. In Figure 2.14, the Y-matrix is simplified into its related lossless matrix in terms of its susceptance parameters, $jB_{11}=jB_{22}$ and $jB_{12}=jB_{21}$. Each susceptance parameter can be accurately extracted or de-embedded with the use of the SOC calibration procedure self-contained in the fullwave MoM algorithm.

Under the equivalence of two networks or models for the two-port identical AC-PCML structure, the initial Y-matrix model can effectively be transformed into the J- or K-inverter network, which has been extensively employed in the synthesis and design of planar and waveguide band-pass filters.

Figure 2.14(b) is the improved unified J-inverter circuit model with the parameters of a J-inverter susceptance (J) at the central part and two equivalent electrical line lengths ($\theta/2$) at the two sides. The susceptance (J), proportional to the capacitively coupling, allows us accurately and efficiently designing the traditional multi-stage band-pass filter in terms of an equivalent cascaded circuit topology mentioned in Chapter I.

On the other hand, the line length ($\theta/2$) represents the phase factor of the frequency-distributed coupled lines and is utilized to make up a half- or partial portion of each line resonator in the microstrip bandpass filter. For the symmetrical two-port structure here, the relation between these two equivalent circuit networks can easily be built up in a pair of closed-form equations as below, where Yo is the characteristic admittance of external microstrip lines, transforming the Y-matrix into the J-inverter network.

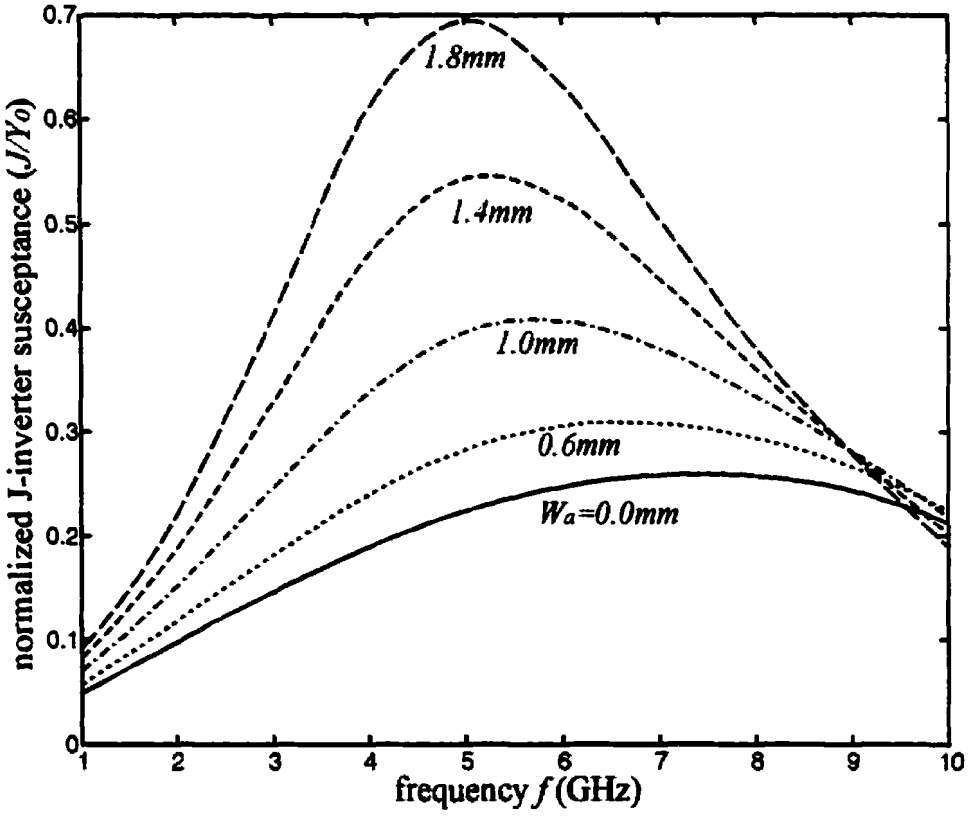

(a) J-inverter susceptance

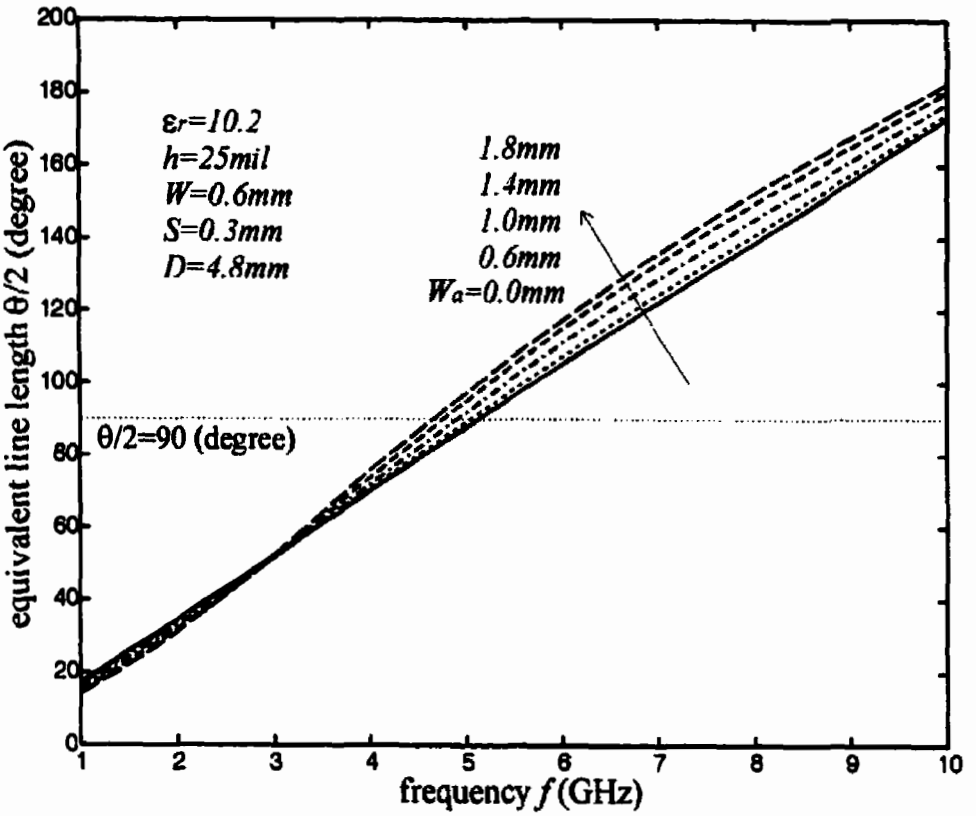

(b) equivalent electrical line length

Figure 2.15 Normalized J-inverter susceptance (J/Y_0) and equivalent electrical line length ($\theta/2$) of an AC-PCML structure with different W_a.

$$\frac{J}{Y_0} = \frac{Y_0 \sin(\theta/2) + B_{11}\cos(\theta/2)}{B_{12}\sin(\theta/2)} \tag{2.21a}$$

$$\theta = -\tan^{-1}\left(\frac{2Y_0 B_{11}}{Y_0^2 - B_{11}^2 - B_{12}^2}\right) \tag{2.21b}$$

With the use of the above EM theory and software, coupling characteristics of this two-port AC-PCML structure will be investigated under different aperture width (W_a) over a wide frequency range. Figure 2.15(a) and (b) depict the SOC-extracted normalized J-inverter susceptance (J/Y_0) and two equivalent electrical line lengths ($\theta/2$) of the AC-

PCML with the line length (D=*4.8mm*) under different aperture width (W_a=*0, 0.6, 1.0, 1.4, 1.8mm*) in a frequency range of *1.0* to *10.0GHz*.

It should be specified here that the extracted J-inverter parameters take into account the entire frequency-related or dynamic electrical behavior existing in the AC-PCML structure. It indicates that these parameters include the frequency-distributed coupling characteristics of two coupled lines over a wide frequency range and also the quasi-lumped parasitic discontinuity effects at the interface between the AC-PCML section and two external microstrip lines.

From Figure 2.15(a), we can observe that the normalized J/Y_0 tends to rise up to some extent at the beginning and then appears to fall down gradually as the frequency increases regardless of different backside aperture width (W_a). In the case of W_a=*0mm* that corresponds to a traditional PCML structure without any backside aperture, its J/Y_0 seems to increment at a very slow pace with frequency and the maximum value is found about *0.27* around f=*7.0GHz*. As the aperture width (W_a) is gradually widened from *0* to *1.8mm*, the incremental pace of J/Yo as a function of the frequency becomes much faster at frequency lower than *5.0GHz* and the maximum value shifts up to a great degree from *0.27* to *0.70*. These results show that the aperture compensation technique proposed here allows us achieving a much tighter coupling with the help of the backside aperture.

On the other hand, it can be seen from Figure 2.15(b) that the equivalent line length ($\theta/2$) goes up in an approximately linear function with frequency, showing the actual phase factor of this AC-PCML structure. In addition to the phase factor of the aperture-compensated coupled lines, this electrical length accounts for the amount contributed by the parasitic quasi-lumped interface discontinuity effect mentioned above. By looking at the extracted parameters in Figure 15(a) and (b) simultaneously, we can find out that the maximum J/Y_0 basically locates close to the frequency where $\theta/2$=90 degree for all

the five cases. It provides an alternative reason why the quarter-wavelength coupled-microstrip line has been extensively employed in the past decades in the design of broad bandpass filters and directional couplers due to its strongest coupling. Otherwise, the frequency of the maximum *J/Yo* is found to slightly shift down as W_a is widened, illustrating that the average effective dielectric constant (ε_{reff}) is reduced to some extent due to the field distribution underneath the strip conductor towards the air region.

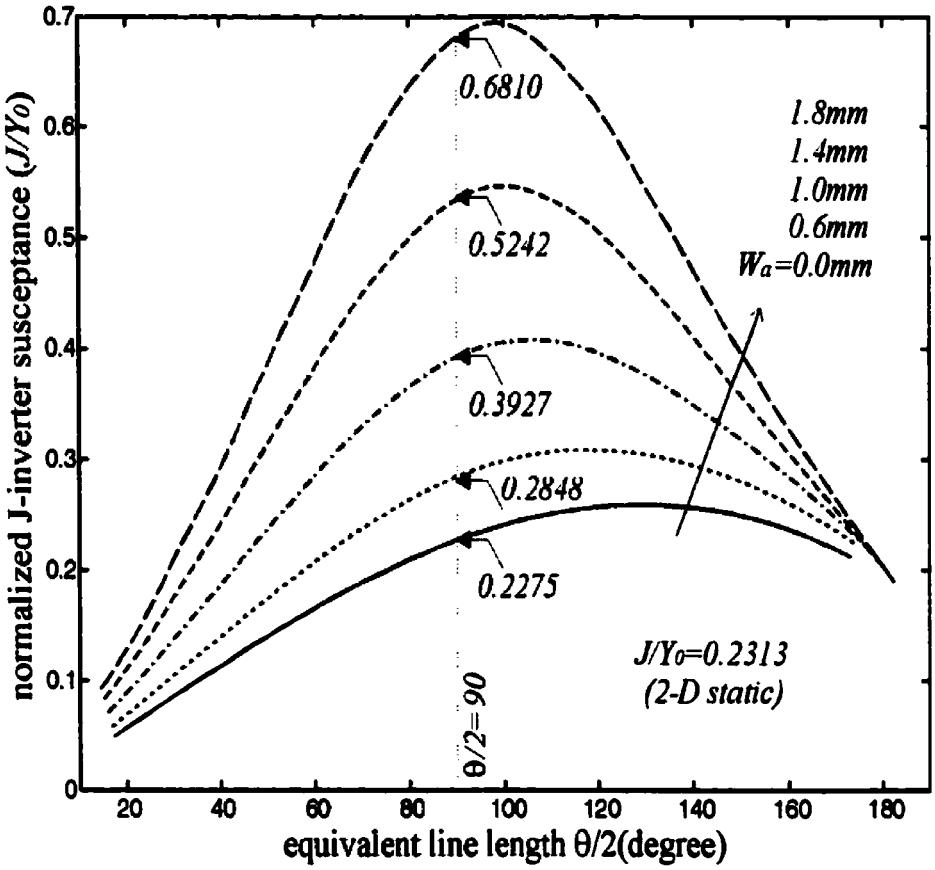

Figure 2.16 Normalized J-inverter susceptance (*J/Yo*) as a function of equivalent electrical line length (θ/2)

To illustrate further the coupling characteristics of this AC-PCML structure, the frequency-dependent curves in Figure 2.15(a) and (b) are plotted again in order to

generate a direct relation between the two parameters, J/Y_0 and $\theta/2$. In the case of $\theta/2$=90 degree, we can find that the parameter J/Y_0 is increased from *0.2275* to *0.6810* as W_a increases from *0* to *1.8mm*. Specifically, the calculated J/Y_0=*0.2275* at W_a=*0mm* is very close to the 2-D static value, J/Y_0=*0.2313*, obtained from Equation (1.12) and Equation (1.13), well verifying our extracted model parameters. In this case, the even- and odd-mode characteristic impedances can be solved from Equation (2.19), that is, Z_{0e}=*60.55ohm* and Z_{0o}=*37.42ohm*, respectively. Also, it can be observed from Figure 2.16 that the maximum J/Y_0 corresponds to the equivalent line length a little larger than $\theta/2$=*90* degree. It is mainly attributed to the parasitic shunt capacitive effect at the interface discontinuity.

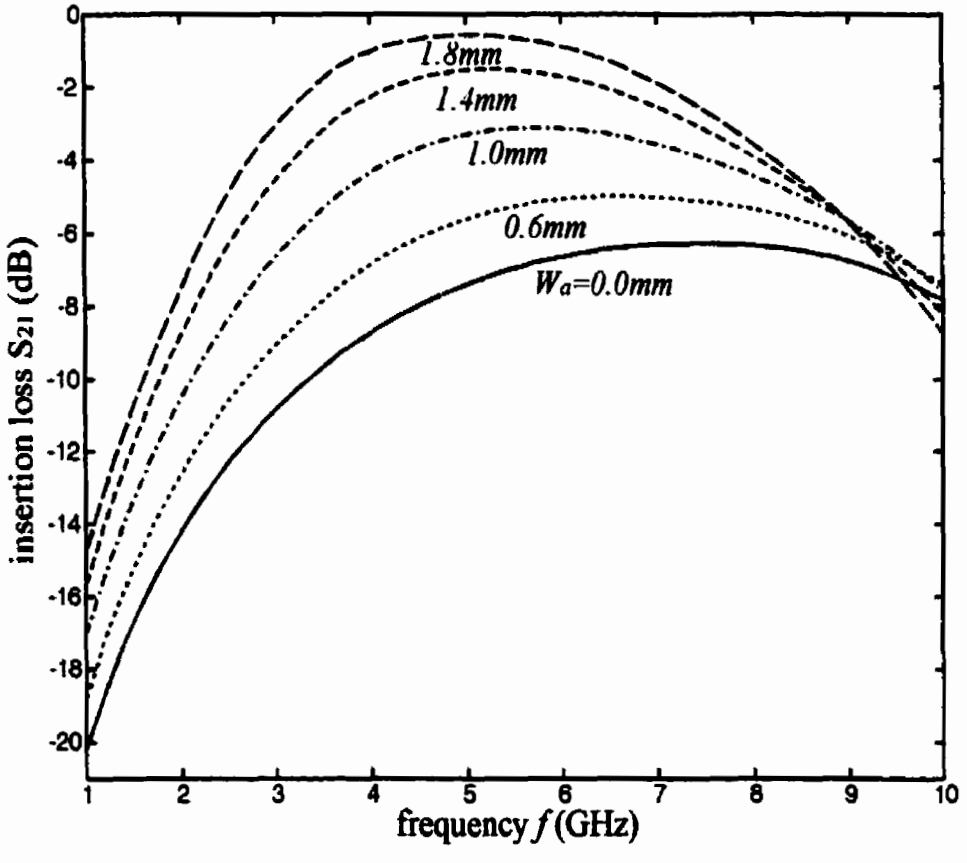

Figure 2.17 Calculated insertion loss (S_{21}) as a function of frequency (f) under different aperture width (W_a).

Figure 2.17 shows a frequency-dependent insertion loss (S_{21}) of this AC-PCML structure under different W_a, which is derived in terms of a closed-form Equation (2.22), according to the calculated J-inverter parameter (J/Y_0) as plotted in Figure 2.15(a). It can be seen that S_{21} gradually shifts up as W_a increases over a wide frequency range. These results provide an easy-to-understand view in support of our claim that the aperture compensation technique can really enhance the coupling of a parallel-coupled microstrip line (PCML).

$$S_{21}(dB) = 10 \times \log_{10}\left\{1 - \left[\frac{1 - J/Y_0}{1 + J/Y_0}\right]^2\right\} \tag{2.22}$$

2.6 CONCLUSION

In this chapter, we start with the physical description and static characterization of traditional high-impedance microstrip line (ML) and parallel-coupled microstrip line (PCML) in terms of several relevant closed-form equations. With the help of calculated parameters, we demonstrate their distinct drawbacks in the design of high-quality microstrip integrated filters, such as high conductor loss, difficulty in fabrication and parasitic effects from conductor thickness and/or configuration.

To overcome these potential problems, an aperture compensation technique is proposed and developed by forming a backside aperture underneath the strip conductors towards the build-up of a novel type of single or coupled microstrip line, called by "aperture-compensated microstrip line" (AC-ML) and "aperture-compensated parallel-coupled microstrip line" (AC-PCML), respectively. From our calculations, we exhibit that this technique allows us not only realizing the high impedance for a single microstrip line but also greatly enhancing the coupling for a parallel-coupling microstrip line. In the

following chapters, the proposed AC-ML and AC-PCML structures will be applied for innovative design of low-loss lowpass and band-pass microstrip filters.

REFERENCES:

(II.1) K. C. Gupta, R. Garg, I. Bahl and P. Bhartia, *Microstrip Lines and Slotlines*, (2nd Ed.), Artech House, Boston, 1996.

(II.2) T. Edwards, "Chapter 8: Passive MICs" in *Foundations for Microstrip Circuit Design*, (2nd Ed.), John Wiley & Sons, 1991.

(II.3) S. B. Cohn, "Parallel-coupled transmission-line-resonator filter," *IRE Trans. Microwave Theory Tech.*, vol.MTT-6, pp.223-231, Apr. 1958.

(II.4) L. Zhu and K. Wu, "Unified equivalent-circuit model of planar discontinuities suitable for field theory-based CAD and optimization of M(H)MIC's", *IEEE Trans. Microwave Theory Tech.*, vol.MTT-47, no.9, Part I, pp.1589-1602, Sept. 1999.

(II.5) L. Zhu, H. Bu, K. Wu and M. Stubbs, "Unified CAD model of microstrip line with backside aperture for multilayer integrated circuits," *2000 IEEE MTT-S Int. Microwave Symp. Dig.*, vol.2, pp.981-984, Boston, June 11-18, 2000.

(II.6) L. Zhu, H. Bu and K. Wu, "Aperture compensation technique for innovative design of ultra-broadband microstrip bandpass filter," *2000 IEEE MTT-S Int. Microwave Symp. Dig.*, vol.1, pp.315-318, Boston, June 11-18, 2000.

CHAPTER III

APERTURE-COMPENSATED MICROSTRIP LINE (AC-ML) FOR DESIGN OF LOW-LOSS MICROSTRIP LOW-PASS FILTER

3.1. INTRODUCTION

In Chapter II, a novel aperture-compensated microstrip line (AC-ML) structure has been proposed for the realization of several attractive electrical features such as low conductor loss, high characteristic impedance and softer fabrication tolerance. With the help of SOC-extracted circuit model parameters in different aperture dimensions, we have showed that this AC-ML can achieve high-valued characteristic impedance by forming a wide backside aperture underneath the strip conductor.

In this chapter, we will focus our attention on the use of this AC-ML structure as an equivalent series inductance element for innovative design of low-loss microstrip low-pass filter. A five-stage low-pass filter is characterized and designed in an efficient manner with the use of its two initial and improved equivalent circuit models. Afterwards, the fullwave EM software, *HP Momentum*, is utilized to simulate the whole circuit layout of this low-pass filter and optimize its electrical performance for the lowest return loss over the low-pass band of concern. Finally, a low-pass filter sample is fabricated and measured to verify the predicted low-pass behavior derived from its equivalent circuit models and also full-wave EM simulation.

3.2 LAYOUT AND UNIFIED CIRCUIT MODEL

Figures 3.1(a) and (b) depict the schematic layout of two classes of the proposed microstrip low-pass filters with two or three aperture-compensated microstrip line (AC-

ML) sections, which are classified as the capacitive-input and inductive-input low-pass filters, respectively. In these two cases, the backside aperture is formed on the infinitely extended ground plane underneath each narrow strip conductor to realize the wanted high-impedance microstrip line that gives rise to a strong series inductance required in the design of a lowpass filter.

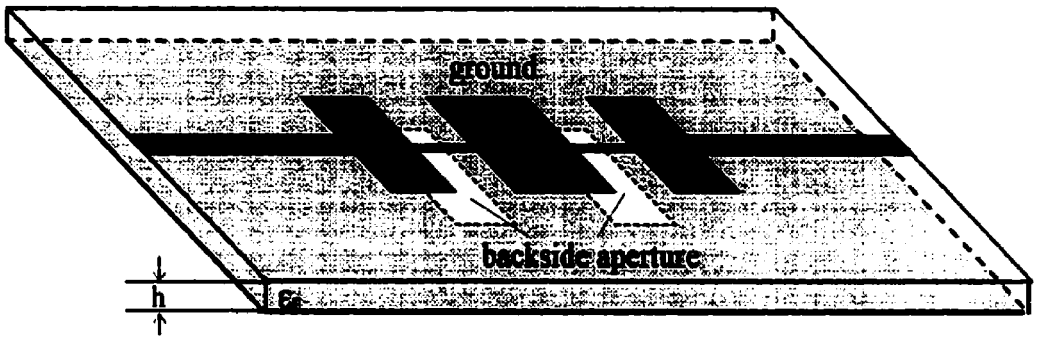

(a) capacitive-input class

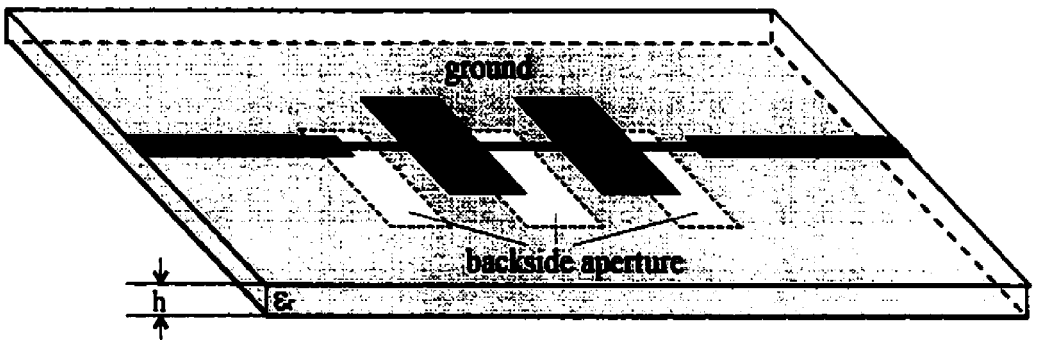

(b) inductive-input class

Figure 3.1 Schematic layout of two classes of microstrip lowpass filters using the aperture-compensated microstrip line (AC-ML) structure.

As detailed above, the high-impedance behavior of this AC-ML structure is realized by weakening significantly the strip-to-ground coupling with the help of the backside aperture. As a result, these microstrip low-pass filters using the AC-ML structure have much lower conductor loss, higher Q factor and larger series inductance than these

traditional counterparts that usually have an extremely narrow strip width. On the other hand, the low-impedance microstrip line can be easily formulated in a traditional manner by widening the strip width towards the build-up of an equivalent shunt capacitance element, required in both lowpass filters as shown in Figure 3.1(a) and (b).

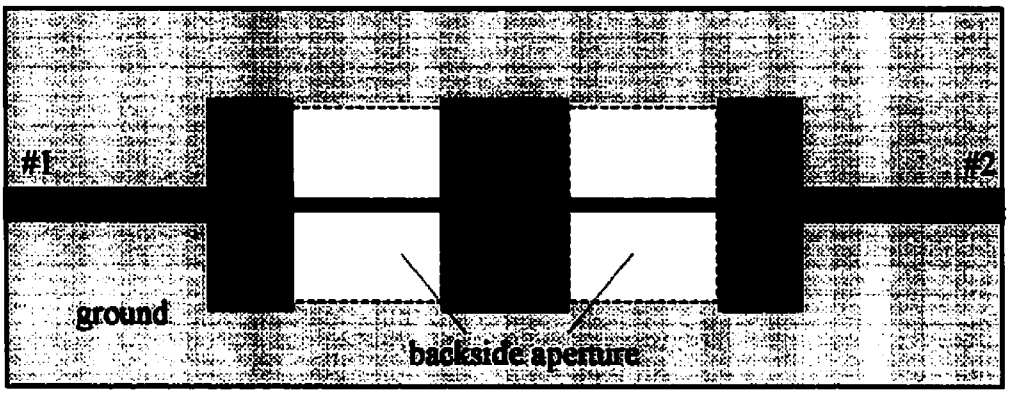

(a) top-view

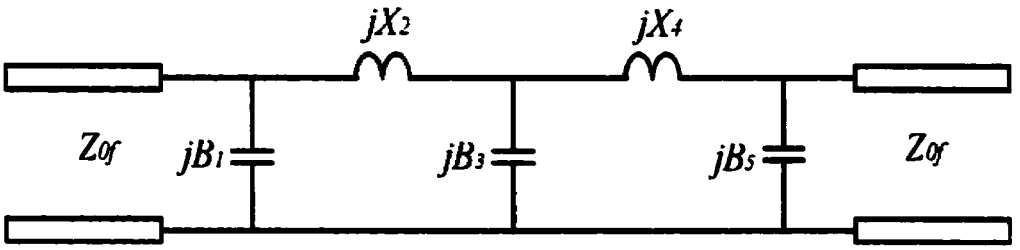

(b) initial circuit model

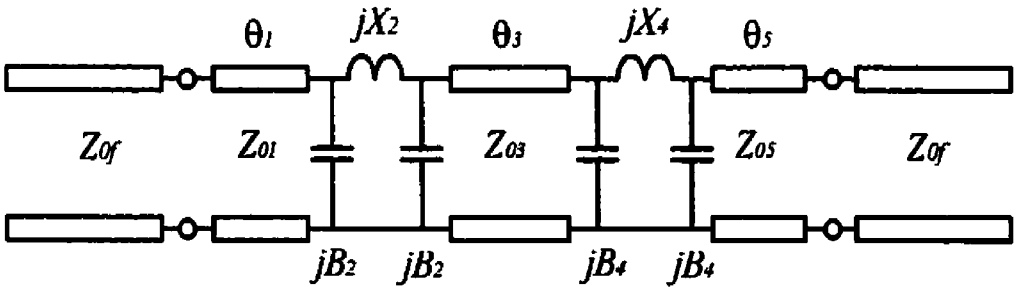

(c) improved circuit model

Figure 3.2 Top-view and its two equivalent circuit models of a five-stage AC-ML low-pass filter.

Here, our extensive study will be carried out on the characterization of the capacitive-input lowpass filter as illustrated in Figure 3.1(a). Figure 3.2(a) shows the top-view of this five-stage lowpass filter launched by two *50 Ohm* external lines. According to the synthesis procedure introduced in Chapter I, we start with the description of its equivalent cascaded circuit model with the circuit elements of lumped series inductance (L) and lumped shunt capacitance (C).

Figure 3.2(b) describes its initial equivalent circuit model under the assumption of perfect microstrip lumped-element circuits. The shunt capacitive elements (jB_1, jB_3, jB_5) correspond to the microstrip line (ML) sections with wide strip width while the series inductive elements (jX_2, jX_4) to the aperture-compensated microstrip line (AC-ML) sections with narrow strip width. Strictly speaking, the shunt capacitive elements (jB_1, jB_3, jB_5) should be wholly made up of the wide ML section as well as the parasitic fringe shunt capacitive elements of its adjacent AC-ML section.

The initial model allows us designing efficiently a low-pass filter on a basis of the matured synthesis procedure as introduced in Chapter I. Because of its approximate pre-assumption of extremely low operation frequency, this model is only available at low frequency range and is not able to take into account all the frequency-distributed effect happening at high frequency range. To overcome this problem, we will formulate an alternative circuit model with frequency-distributed circuit parameters.

Figure 3.2(c) depicts an improved equivalent circuit model of this filter with a cascaded topology, made up of uniform transmission line sections and admittance matrices. Each ACML section is here characterized as an equivalent π-network matrix with a frequency-distributed series reactance (jX_2 or jX_4) and two identical shunt susceptances (jB_2 and jB_4). In Chapter II, the discontinuity effect at the interface between two adjacent ML and AC-ML sections has been well considered in the circuit parameters of the AC-ML. As a result, each ML section can simply be characterized as the uniform

transmission line section with the parameters of characteristic impedance (Z_{01}, Z_{03} or Z_{05}) and electrical line length (θ_1, θ_3 or θ_5) as shown in Figure 3.2(c).

3.3 Unified Circuit Model of AC-ML Structure

To simplify the description of the AC-ML's layout dimension and circuit parameters, Figure 3.3 re-plots the layout and equivalent circuit model of this two-port AC-ML structure. With the use of the SOC calibration procedure self-contained in the fullwave MoM algorithm, all the circuit parameters in Figure 3.3(b) can be effectively extracted over the wide frequency range of interest. To obtain the lumped circuit parameters of the AC-ML section as required in the initial circuit model in Figure 3.2(b), the operating frequency is selected to achieve an extremely low value (f=*1.0 GHz* in this case).

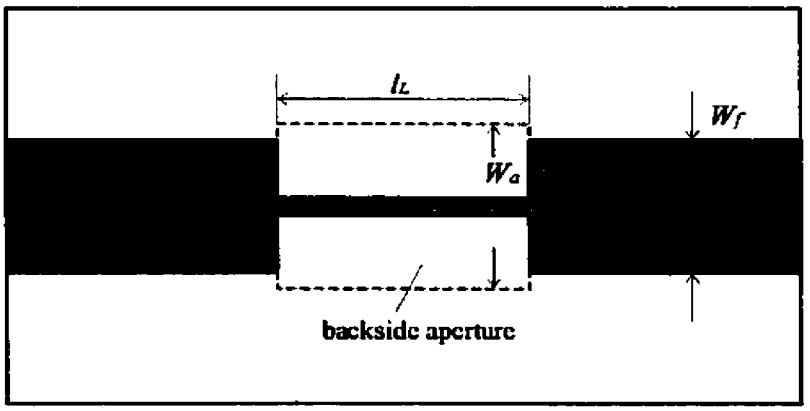

(a) layout

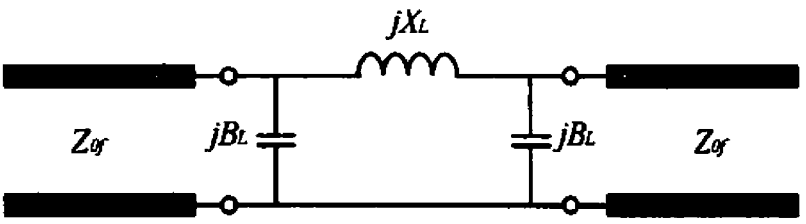

(b) equivalent circuit model

Figure 3.3 Layout and equivalent circuit model of the two-port AC-ML section.

Accordingly, these lumped circuit parameters can simply be derived from the calculated series reactance (jX_L) and shunt susceptance (jB_L) in its unified equivalent circuit model as illustrated in Figure 3.3(b). On the other hand, the wide ML section can effectively be expressed as a single equivalent shunt capacitance in terms of a closed-form function with its guided-wavelength and characteristic impedance using Equation (1.7).

Figure 3.4(a) and (b) depict the extracted series reactance (jX_L) and shunt susceptance (jB_L) of the AC-ML's equivalent circuit model versus the aperture length (l_L) under the fixed strip width ($W=0.2mm$) and fixed aperture width ($W_a=3.0mm$) over the frequency range ($f=1.0$ to $10.0GHz$). The solid lines represent the frequency-distributed or dynamic circuit parameters extracted at different frequencies, while the dashed lines are those corresponding to the lumped or static series inductance and shunt capacitance parameters obtained at the low frequency ($f=1.0GHz$).

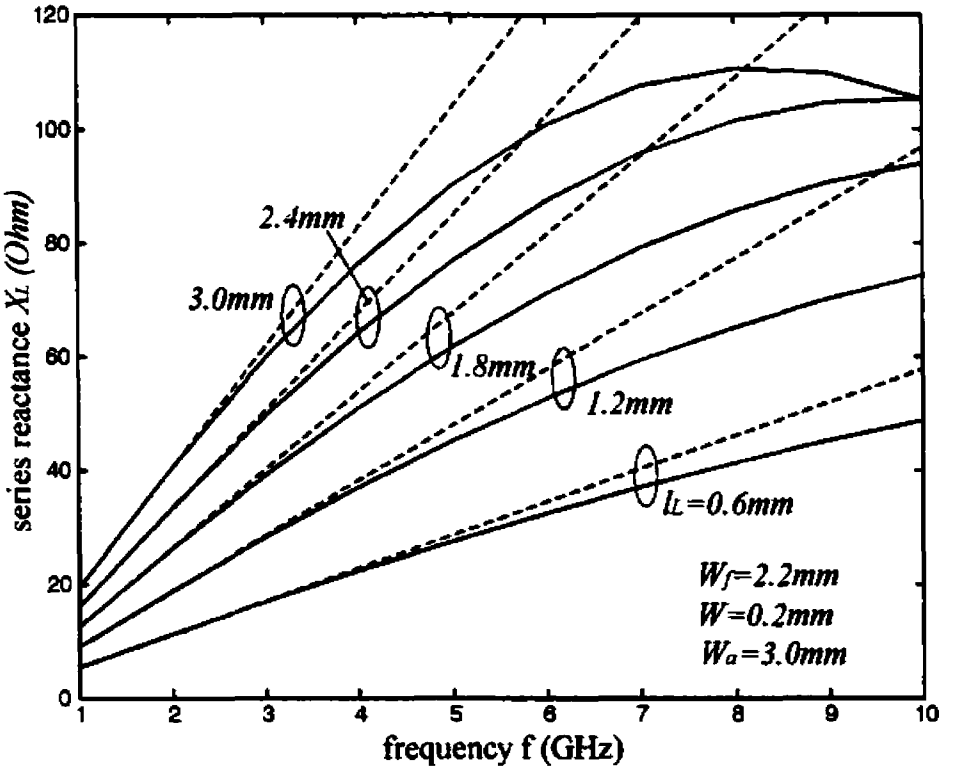

(a) series reactance (jX_L)

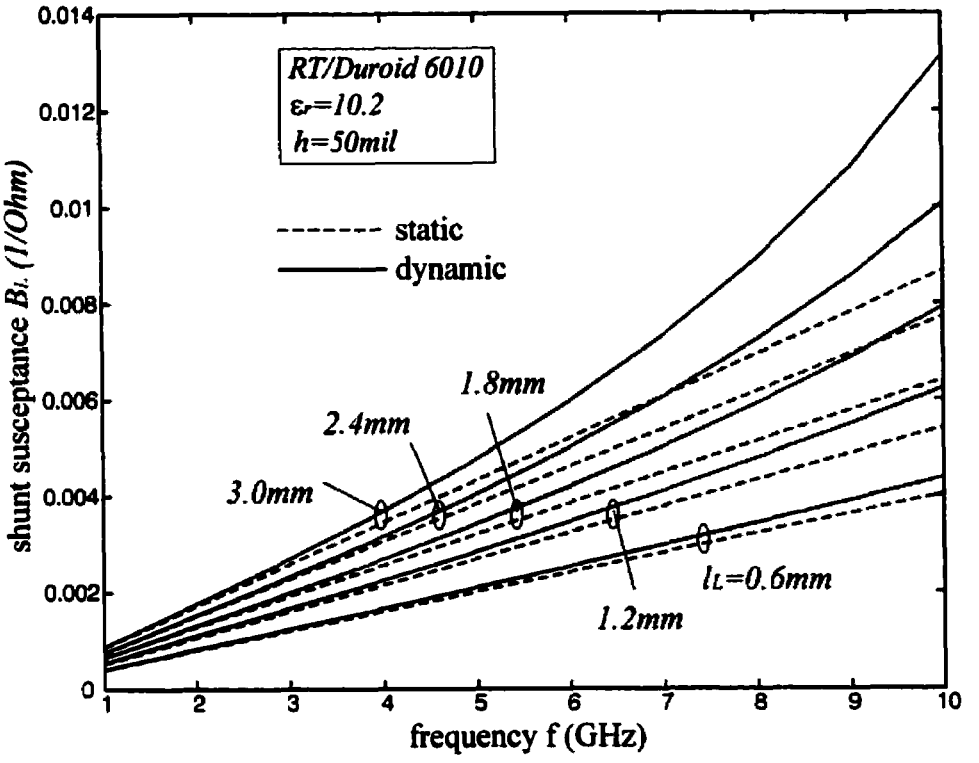

(b) shunt capacitance (jB_L)

Figure 3.4 Extracted series inductance (jX_L) and shunt capacitance (jB_L) as a function of operating frequency: static case (dashed line) and dynamic case (solid line).

At low frequency, the extracted dynamic circuit parameters (jX_L and jB_L) show an approximately linear increase with frequency and very close to those in the static case, thus exhibiting a good lumped-element electrical behavior. By looking at the dashed lines in Figure 3.4(a), it can well be seen that the equivalent static inductance (X_L/ω) shifts up rapidly and gains a significant enhancement by roughly three times higher as l_L increases from *0.6mm* to *3.0mm*. At the meantime, the equivalent static shunt capacitance (B_L/ω) tends to rise up slightly, showing that the shunt capacitive effect of the AC-ML section gradually appears to increment as l_L increases.

As the frequency increases, X_L goes up in a slowly nonlinear function and then tends to slightly fall down in the case of the extended aperture length, especially at l_L=*3.0mm*,

thereby showing that the frequency-distributed parasitic effects increases to a visible level at the high frequency. Otherwise, B_L goes up in an accelerated speed with the frequency as l_L is further extended to *3.0mm*.

It can be observed in the following discussion that the existence of such a parasitic shunt capacitive element will definitely damage the actual series inductance of the long AC-ML section at high frequency. With the use of these circuit parameters, the filter layout will be characterized and designed based on its two equivalent circuit models as in Figure 3.2(b) and (c).

3.4 Circuit Model Based Synthesis and Optimization

The initial equivalent circuit model as illustrated in Figure 3.2(b) is utilized to carry out the first-round synthesis design of the electrical filtering behavior of the five-stage microstrip low-pass filter as shown in Figure 3.2(a). For the Chebyshev-type low-pass filter as discussed in Chapter I, the series inductance (jX_2 and jX_4) and shunt capacitance (jB_1, jB_2 and jB_3) can be determined under the designated maximum insertion loss from Figure 1.2 and Table 1.1. They can be expressed in terms of their corresponding lumped circuit parameters (g_i) in the prototype lowpass filter, through Equation (1.6).

Furthermore, the related frequency response of this filter can be characterized by multiplying the ABCD matrix of its initial circuit model in Figure 3.2(b) as in Equation (3.1) and then transforming its final ABCD matrix into its scattering matrix as in Equation (3.2) for a symmetrical two-port network.

$$\begin{bmatrix} a & b \\ c & d \end{bmatrix} = \begin{bmatrix} 1 & 0 \\ jB_1 & 1 \end{bmatrix} \cdot \begin{bmatrix} 1 & jX_2 \\ 0 & 1 \end{bmatrix} \cdot \begin{bmatrix} 1 & 0 \\ jB_3 & 1 \end{bmatrix} \cdot \begin{bmatrix} 1 & jX_4 \\ 0 & 1 \end{bmatrix} \cdot \begin{bmatrix} 1 & 0 \\ jB_5 & 1 \end{bmatrix} \tag{3.1}$$

$$S_{22} = S_{11} = \frac{a - d + b/Z_{0f} - cZ_{0f}}{a + d + b/Z_{0f} + cZ_{0f}}$$

$$S_{12} = S_{21} = \frac{2}{a + d + b/Z_{0f} + cZ_{0f}} \tag{3.2}$$

where Z_{0f} is the characteristic impedance of two external microstrip lines.

Next, the frequency response of this low-pass filter is analyzed and designed by employing the improved circuit model, as depicted in Figure 3.2(c), which can account for all the frequency-distributed electrical behavior existing in the overall filter layout. As opposed to its initial circuit model, this improved model accurately represents the AC-ML section as a unified equivalent network with the parameters of a series reactance (jX_L) and two shunt susceptances (jB_L). Meanwhile, this model effectively perceives the ML section as an equivalent uniform line section with low impedance (Z_{01}, Z_{03} or Z_{05}), as illustrated in Figure 3.2 (c). Under no pre-assumption in obtaining the related circuit model parameters, this model is supposed to be able to undertake an efficient and accurate design procedure on the basis of an equivalent cascaded network topology.

In the case of a five-stage Chebyshev-type low-pass filter to be studied here, we can simplify the model configuration by reducing the finite number of independent circuit parameters in Figure 3.2(c) such that $Z_{05}=Z_{03}=Z_{01}$, $\theta_5=\theta_1$, $jX_4=jX_2$ and $jB_4=jB_2$. As a result, the optimization procedure can be implemented with the determinant of only five unknown parameters of Z_{01}, θ_1, θ_3, jX_2 and jX_4.

In this case, the final ABCB matrix of this filter can be obtained by multiplying several ABCD matrices of five sections or networks in Figure 3.2(c), that is, uniform transmission line section and Y-admittance matrix as below. Furthermore, its

corresponding insertion loss (S_{21}) and return loss (S_{11}) can be derived based on a matrix transformation equation as in Equation (3.2). Until now, the frequency response of this five-stage lowpass filter can be characterized based on two different circuit models in terms of Equation (3.1) to Equation (3.3).

$$\begin{bmatrix} a & b \\ c & d \end{bmatrix} = \begin{bmatrix} \cos\theta_1 & jZ_{01}\sin\theta_1 \\ j\sin\theta_1/Z_{01} & \cos\theta_1 \end{bmatrix} \cdot \begin{bmatrix} 1-B_2X_2 & jX_2 \\ jB_2(1-B_2X_2) & 1-B_2X_2 \end{bmatrix}$$

$$\cdot \begin{bmatrix} \cos\theta_3 & jZ_{01}\sin\theta_3 \\ j\sin\theta_3/Z_{03} & \cos\theta_3 \end{bmatrix} \cdot \tag{3.3}$$

$$\begin{bmatrix} 1-B_2X_2 & jX_2 \\ jB_2(1-B_2X_2) & 1-B_2X_2 \end{bmatrix} \begin{bmatrix} \cos\theta_1 & jZ_{01}\sin\theta_1 \\ j\sin\theta_1/Z_{01} & \cos\theta_1 \end{bmatrix}$$

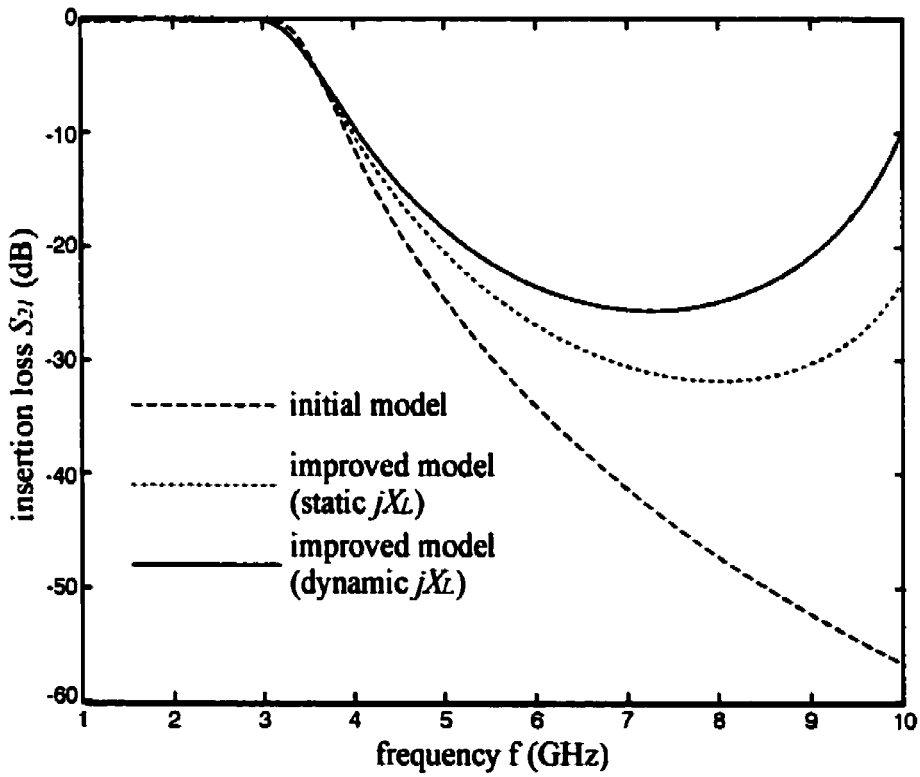

(a) insertion loss (S_{21})

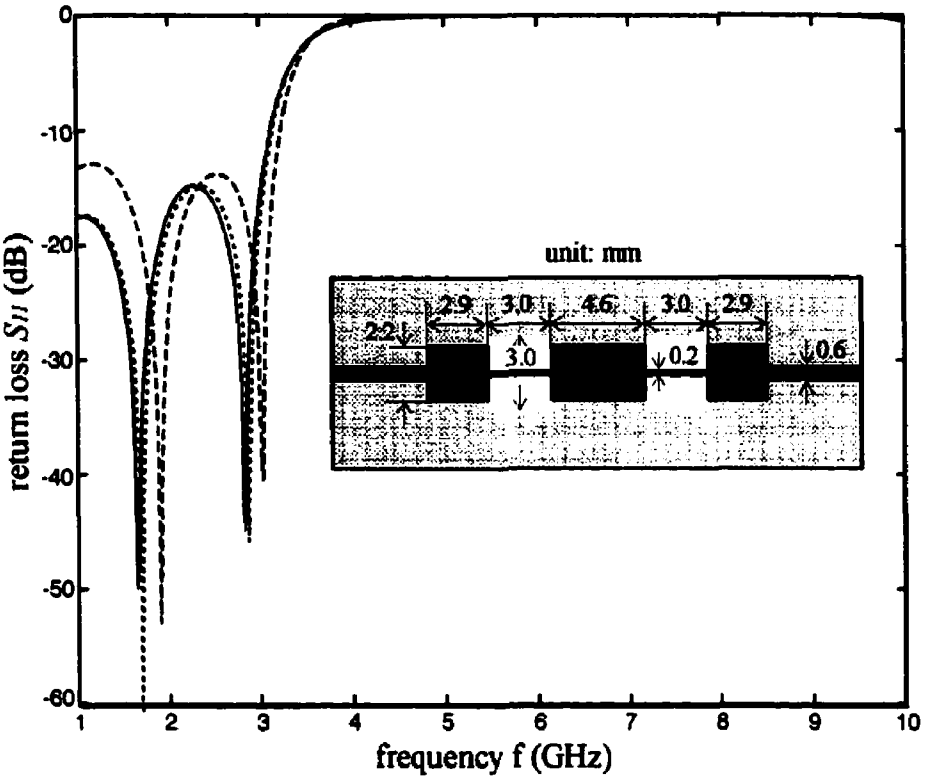

(b) return loss (S11)

Figure 3.5 Predicted frequency response of a five-stage microstrip low-pass filter, obtained from two equivalent circuit models as in Figure 3.2(b) and (c).

Figure 3.5(a) and (b) represent the three groups of the optimized insertion loss (S_{21}) and return loss (S_{11}) over the frequency range (*f=1.0* to *10.0 GHz*). The optimized filter layout with detailed dimensions is shown in the central part of Figure 3.5(b). By looking at the predicted results from the initial circuit model in Figure 3.5(a), the insertion loss (S_{21}) achieves the flat pass configuration at frequencies lower than *3.0 GHz* and then gradually falls down in a monotonously changed manner as the frequency further increases.

Otherwise, the return loss (S_{11}) can be seen from Figure 3.5(b) to achieve *–12 dB* in the low-pass band (< *3.0 GHz*) and then to rise up rapidly towards its maximum value of *0-dB* in its a high-stop band. Due to the assumption of lumped parameters in this initial

model, the predicted results completely ignore all the frequency-distributed electrical characteristics so that the disturbed frequency response can't be completely observed even at high frequency.

In fact, the AC-ML or ML sections with finitely extended line length are definitely subject to parasitic frequency dispersion as the frequency increases to the range where their line lengths are comparable to the guide-wavelength. With the use of our improved circuit model, its frequency response is again characterized by using the calculated static and dynamic circuit parameters of the AC-ML section, which are illustrated in Figure 3.4 (a) and (b). From 3.5(a) and (b), we can observe that both predicted results have almost the same low-pass behavior as those of the initial model at low frequency, and then seem to be increasingly disturbed and degraded at high frequencies.

In the static case, the minimum S_{21} shifts up significantly to about *–32.0 dB* at the higher frequencies, which exhibits its parasitic frequency dispersion attributed by the uniform line section with high impedance. In the dynamic case, its minimum S_{21} is further raised to *–26.0 dB* at the high-stop band, which is additionally contributed by the frequency-distributed circuit parameters of each AC-ML section accounted in the improved model. By comparing the three groups of predicted frequency response, it can be understood that the initial circuit model is only valid at low frequency range. By contrast, the improved circuit model with extracted dynamic circuit parameters may be utilized over the wide frequency range of concern due to its consideration of all the high-frequency dispersion effect.

3.5 FULLWAVE EM SIMULATION

To further investigate the electrical behavior of the filter in theory, the commercial software HP Momentum is used here to implement the fullwave simulation of the whole

filter layout as illustrated in Figure 3.2(a). This software has been well developed on a basis of the 2.5-D fullwave method of moments (MoM) algorithm and has gained a wide application in the numerical simulation and characterization of a large variety of planar integrated passive circuits. This software allows automatic meshing based on the operating frequency for a pre-designated frequency range and also different mesh configurations such as non-uniform rectangular and triangular meshes.

Since the numerical EM simulation is carried out over the whole layout of a given planar circuit, the predicted results can account for all the physical effects such as frequency dispersion, each discontinuity part and also the inter-coupling effects between two adjacent discontinuity parts. Basically, we can derive the much more accurate results by increasing the mesh number and also choosing the non-uniform meshes at the sharply changed section of the layout. However, it will definitely generate few problems such as the long CPU (*Computer Processing Unit*) time and large occupied memory when it is utilized for fullwave simulation of electrically large planar circuits.

Also, this software has been extensively applied for EM optimization of practical planar circuits due to no other software available for efficient synthesis design of these circuits. In this case, the targeted frequency response is achieved in a very time-consuming multi-round searching manner by determining a number of unknown dimension parameters, e. g. strip width/length and aperture width/length in this filter layout. In this work, the optimization procedure is implemented in the HP Momentum based simulation by slightly adjusting the limited number of dimensions at the starting of the filter layout configuration, obtained from the above equivalent circuit model.

Figure 3.6 depicts the predicted and optimized frequency response of such a low-pass filter using the HP Momentum software over the same frequency range as in Figure 3.5. Two groups of simulated curves correspond to slightly different aperture lengths (D)

and central microstrip line lengths (L), that is, *D=3.0mm & L=4.2mm* (TraceA) and *D=2.9mm & L=4.6mm* (TraceB), as illustrated in Figure 3.6. Looking at the predicted results in Figure 3.5 and Figure 3.6 together, we can observe that they are in good agreement with each other over the frequency range (*f=1.0* to *10.0 GHz*). Especially, the minimum insertion loss (S_{21}) achieve *–27.2 dB* and *–27.5 dB*, respectively, in the Momentum based optimization as opposed to *–26.0 dB* obtained from its improved circuit model as in Figure 3.5.

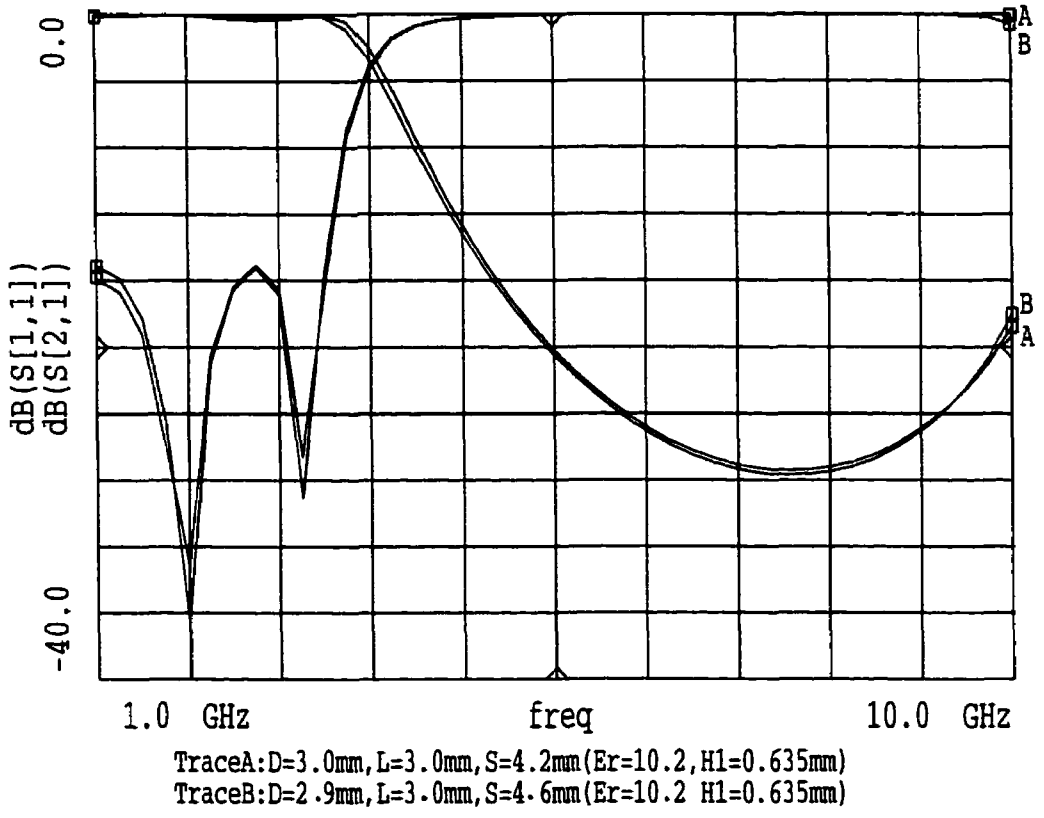

Figure 3.6 Predicted and optimized frequency response of the five-stage microstrip low-pass filter obtained from the HP Momentum software.

Otherwise, the maximum return loss (S_{11}) over the low-pass band is found about *–15.0 dB*, showing the satisfactory low-pass filter behavior. These predicted results obtained from the fullwave commercial EM software not only provide a good verification on the

efficient circuit model based design procedure and also show the actual filtering performance of the proposed AC-ML's lowpass filter.

3.6 MEASUREMENTS AND DISCUSSION

Finally, a filter sample is fabricated according to the filter dimensions in the case of TraceB in Figure 3.6 and then measured to compare with the predicted results shown above. Figure 3.7(a) and (b) illustrate the upper-layer and bottom-layer configuration of this lowpass filter, respectively, arranged for etching fabrication of two sides of a single dielectric substrate: RT/Duroid 6010. The two backside apertures at the bottom layer are formed at the same location as the two narrow microstrip lines in order to build up the high-impedance AC-ML section. To measure its frequency response over the wide frequency range, the two external microstrip lines with *50 Ohm* are electrically connected with the two-port coaxial lines of the HP Network Analyzer.

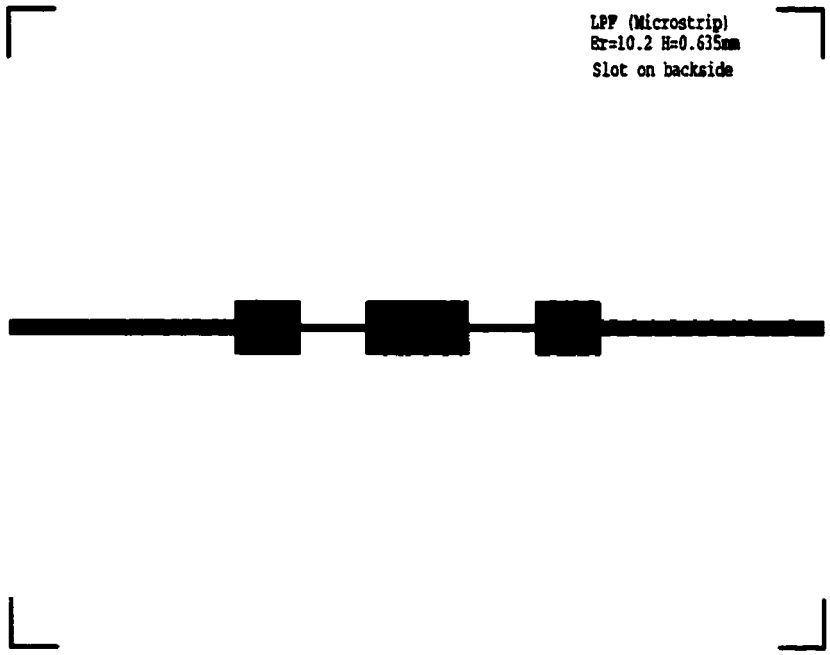

(a) upper-layer

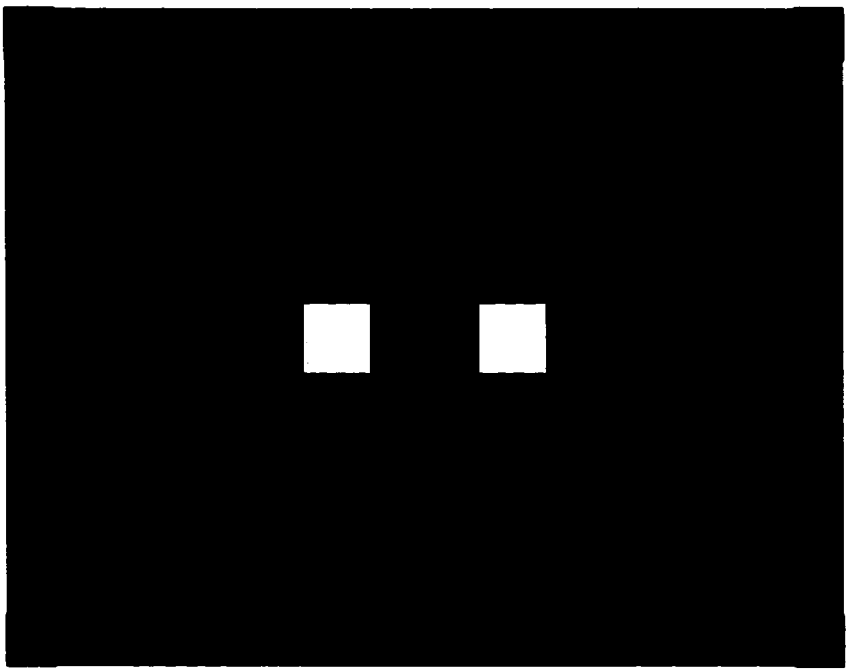

(b) bottom-layer

Figure 3.7 Upper- and bottom-layer configration of a five-stage microstrip lowpass filter arranged for etching fabrication.

The calibration procedure is carried out with the use of a simple full two-port option. In this case, the three calibration standards, that is, coaxial open-circuit, short-circuit and matched load, are utilized to calibrate the two coaxial terminals. Meanwhile, the two coaxial terminals are linked together to obtain its transmission and isolation performance. After such a calibration procedure, the two-port low-pass filter sample is connected to the two terminals and its frequency response can be eventually measured by using the two-port calibrated date saved in the HP Network Analyzer.

Figure 3.8 shows our measured frequency response (S_{11} & S_{21}) of the fabricated low-pass filter sample, exhibiting the almost same filtering behavior as those obtained from the improved circuit model and the fullwave Momentum software over the wide frequency range. From Figure 3.8, it can be seen that the maximum return loss (S_{11}) in

the low-pass band is about *–16 dB* and the minimum insertion loss (S_{21}) in the high-stop band achieves about *–26.0 dB*. By comparing all the three groups of frequency response in Figure 3.5, 3.6 and 3.8, we can further find that the measured results are much closer to those from the HP Momentum rather than those from circuit model.

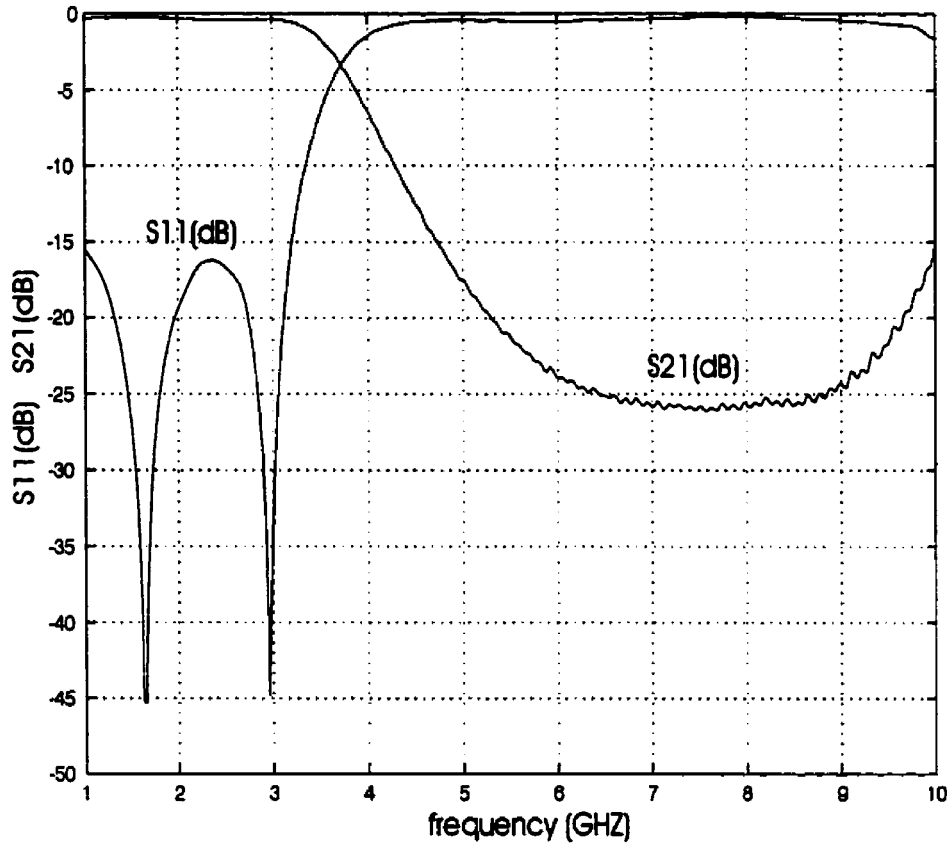

Figure 3.8 Measured frequency response of the five-stage microstrip lowpass filter sample using the HP Network Analyzer.

Especially, the predicted and measured cut-off frequency between the lowpass band and high-stop band under the 3dB-down definition of S_{21} can be derived from Figure 3.5, 3.6 and 3.8 as *3.45*, *3.71* and *3.68 GHz*, respectively. Also, some ripple configuration can be observed from the measured S_{21} at high frequency and they may be attributed to the one-step calibration procedure over such a wide frequency range.

3.7 CONCLUSION

In this Chapter, the aperture-compensated microstrip line (AC-ML) structure has been applied as a low-loss high-impedance transmission line for the innovative design of a multi-stage microstrip low-pass filter. Its initial electrical filtering behavior is characterized with the use of its unified equivalent circuit models under the matured and efficient network-based synthesis procedure. The whole filter layout is then simulated and designed in terms of the HP Momentum software and the optimized electrical behavior is achieved by slightly adjusting the filter dimension. Finally, a filter sample is fabricated and measured to verify our predicted results and also to show its actual low-pass behavior. From these results, it can well be understood that the proposed AC-ML structure allows realizing well high characteristic impedance with the help of the backside aperture under the low conductor loss. Therefore, it is our belief here that this AC-ML should gain a potentially wide application in the design of high-quality lowpass filters using the multilayered fabrication technology.

REFERENCES:

(III.1) T. Edwards, "Chapter 8: Passive MICs" in *Foundations for Microstrip Circuit Design*, (2nd Ed.), John Wiley & Sons, 1991.

(III.2) L. Zhu and K. Wu, "Unified equivalent-circuit model of planar discontinuities suitable for field theory-based CAD and optimization of M(H)MIC's", *IEEE Trans. Microwave Theory Tech.*, vol.MTT-47, no.9, Part I, pp.1589-1602, Sept. 1999.

(III.3) L. Zhu, H. Bu, K. Wu and M. Stubbs, "Unified CAD model of microstrip line with backside aperture for multilayer integrated circuits," *2000 IEEE MTT-S Int. Microwave Symp. Dig.*, vol.2, pp.981-984, Boston, June 11-18, 2000.

CHAPTER IV

APERTURE-COMPENSATED PARALLEL-COUPLED MICROSTRIP LINE (AC-PCML) FOR DESIGN OF BROADBAND MICROSTRIP BANDPASS FILTER

4.1 INTRODUCTION

Microstrip band-pass filter has been studied as one of building blocks in the design of microwave circuits and systems. With its easy-to-achieve coupling designated, a parallel-coupled microstrip line (PCML) has widely been used in multi-stage band-pass filters as capacitive coupling element between two adjacent line resonators. To realize a multi-pole and broad band-pass filter with a deep out-of-band rejection, a usual procedure is to reduce both of its strip and slot widths in order to achieve a tight coupling, and a large number of line resonators are required in this case. This may lead to a degradation of its filtering behavior, namely, low Q-factor and high insertion loss. Also, it may bring up some difficulties in the design procedure as well as fabrication process due to its sensitivity to strip/slot widths and conductor thickness/configuration.

On the other hand, the ultra-wideband (UWB) technology has stimulated an increasing interest for communication and radar applications over the past years. Nevertheless, it is difficult to design broadband active and passive circuits having the bandwidth of $BW>20\%$. In fact, the filter design procedure available to date was essentially established with (quasi-) lumped elements, and its design formulas were developed under the assumption of frequency-independent circuit parameters over a narrow frequency range around the center frequency. So, it seems difficult to apply this procedure in the design of band-pass filters with $BW>20\%$. This is because all the basic elements such as line resonator and coupling section are strongly frequency-distributed

in this case. In other words, their electrical characteristics are too frequency-dependent over a wide frequency range.

In this work, the aperture-compensated parallel-coupled microstrip line (AC-PCML) structure is applied as a tight coupling element for innovative design of novel ultra-broadband microstrip bandpass filters. First of all, the two-port AC-PCML is characterized into a unified equivalent J-inverter network with the use of SOC technique in the fullwave MoM algorithm as discussed above. Then, a novel multi-pole and broadband microstrip bandpass filter made with a single line resonator is originated by attaching a uniform line section between the two AC-PCML section. A closed-form equation is established to demonstrate the operating mechanism of the proposed filter.

To further realize design specifications such as low return loss, adjustable broad bandwidth and wide out-of-band rejection, a pair of capacitive open-ended stubs is introduced into the central location of the line resonator for effective suppression of its harmonic passband. Also, these two filters are further designed through the HP Momentum software and the predicted performance is verified by our own experiments.

4.2. Unified Circuit Model of A Single AC-PCML Structure

Figure 4.1(a) depicts the 3-D geometrical layout of the two-port AC-PCML structure with two external microstrip lines, in which a wide aperture is formed over its ground plane. As briefly studied in Chapter II, this PCML supposes to be able to achieve the much stronger coupling degree by narrowing the strip and slot widths to some extent at the same area as the backside aperture.

Figure 4.1(b) is its 2-D top-view arranged for allowing us understanding its geometry and also carrying out the MoM-SOC based modeling of its electrical behavior. As in

Chapter II, the SOC technique in the fullwave MoM algorithm is employed to characterize this two-port AC-PCML as its equivalent J-inverter circuit model defined at the two reference planes (R_1 & R_2).

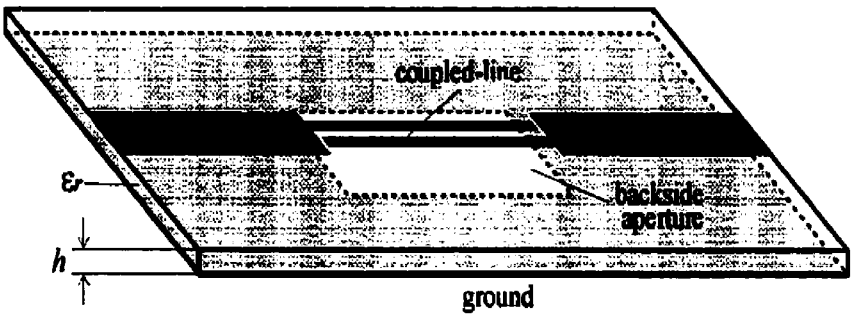

(a) geometrical layout

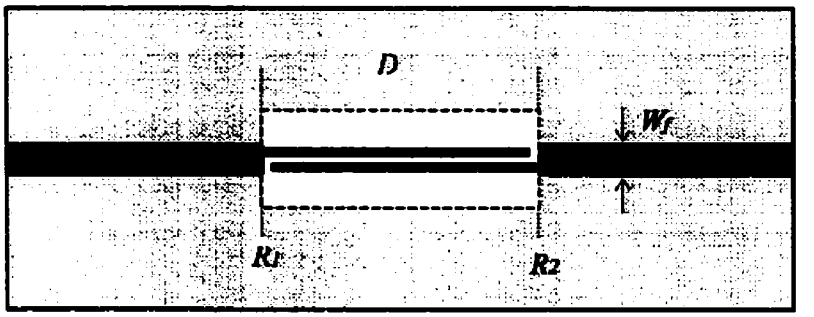

(b) top-view

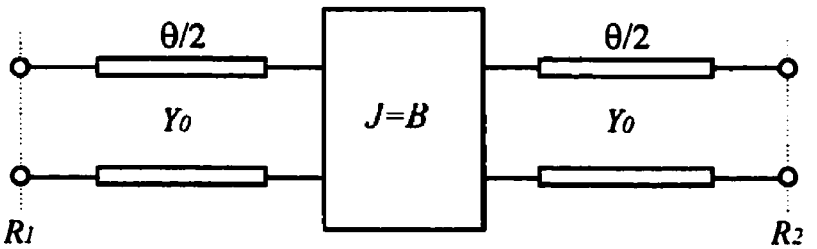

(c) J-inverter network

Figure 4.1 Geometry and unified equivalent circuit model of the two-port AC-PCML.

Figure 4.1(c) illustrates its unified equivalent J-inverter circuit model with the circuit parameters of a J-inverter susceptance (J) and two equivalent electrical line lengths ($\theta/2$), as depicted in Figure 2.14(b). Theses equivalent circuit parameters are accurately

extracted from the fullwave MoM calculation, and of course can account for all the complex discontinuity effects in this whole two-port AC-PCML structure including the interface between the uniform AC-PCML and the external microstrip line. To our knowledge, the J-inverter susceptance (J) can be utilized as the capacitively series coupling degree for the parallel-coupled transmission line.

Figure 4.2(a) shows the SOC-calibrated normalized J-inverter susceptance (J/Y_0) of the AC-PCML with different aperture widths W_a over an ultra-wide frequency range (f=*1.0* to *16.0 GHz*). This result indicates that the parameter (J/Y_0) basically varies in a periodical manner with frequency for all the three cases, thus exhibiting a frequency dispersion behavior of the parallel-coupled transmission lines. It can be conceptually interpreted that the frequency-distributed coupling between the two parallel-coupled strip conductors strongly depends on the electrical length of this PCML section, D/λ_{g0}.

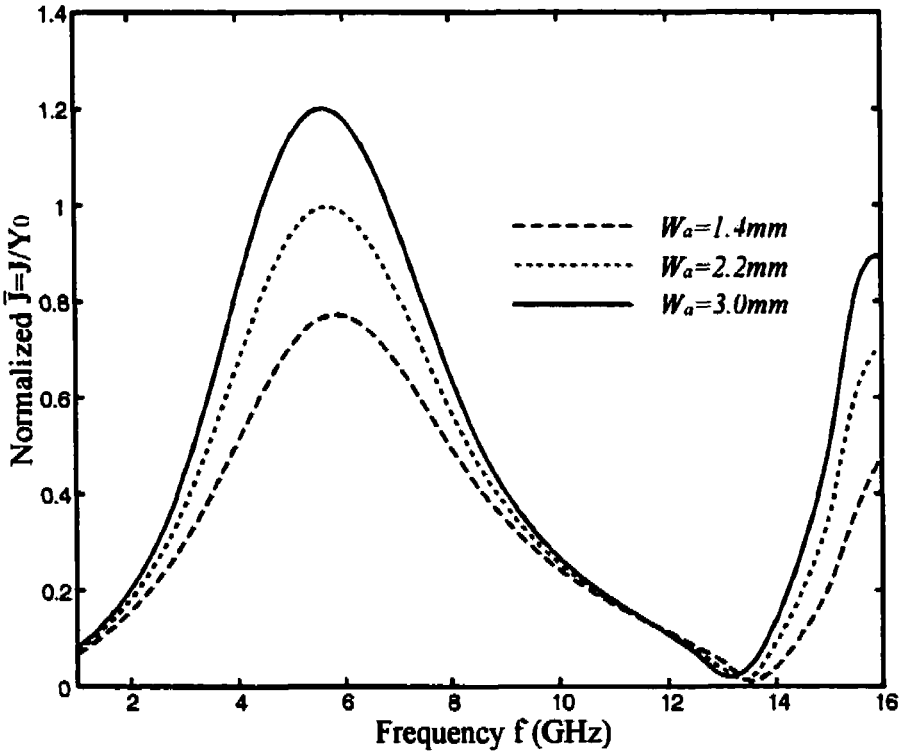

(a) normalized J-inverter suscepatnce

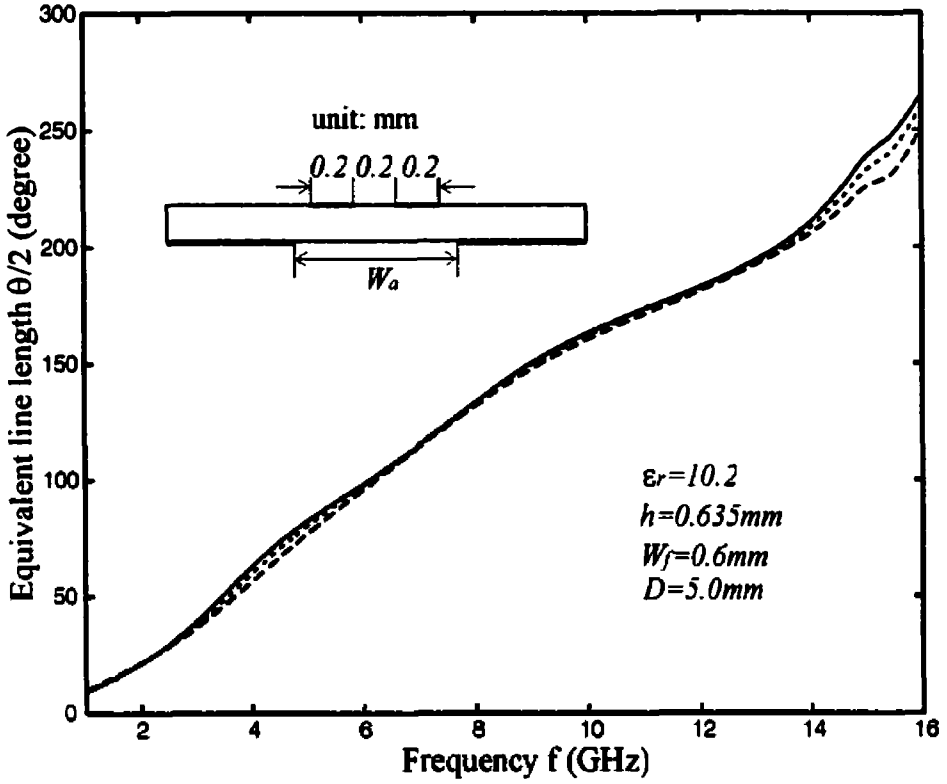

(b) equivalent electrical line length

Figure 4.2 SOC-calibrated J-inverter network parameters of the two-port AC-PCML with different aperture widths W_a=*1.4, 2.2, 3.0mm.*

The peak coupling (*J/Yo*) essentially appears around the operating frequencies where $D/\lambda_{g0} = (2n-1)/4$ and the null (*J/Yo*) is close to those where $D/\lambda_{g0} = n/2$ ($n = 1$ or *2*). The peak value of (*J/Yo*) raises significantly from *0.6* to *1.2* as W_a is widened from *1.4* to *3.0mm*, showing that its capacitively coupling strength can really gain a very effective enhancement with the help of a wide backside aperture. As opposed to the result as illustrated in Figure 2.15(a), we can further observe that the choice of narrow coupled-strip width (*W=0.2mm*) leads to the much tight peak coupling degree.

Figure 4.2(b) depicts the SOC-extracted equivalent electrical line length ($\theta/2$) of this AC-PCML structure. The parameter ($\theta/2$) can be observed as the frequency increases

from *1.0* to *16.0 GHz* to vary in the almost same configuration for all the three cases and rise up rapidly from *15* to *260* degree in an approximately linear manner. By looking at the frequency-dependent (J/Y_0) and ($\theta/2$) in Figure 4.2(a) and (b) together, we can further figure out that the peak (J/Y_0) happens at the proximity of the frequency for which $\theta/2=90$ or *270* degree while the null (J/Y_0) around that corresponds to $\theta/2=180$ degree. It gives an alternative explanation from our 3-D simulation why the quarter-wavelength parallel-coupled transmission line with the easy-to-achieve tight coupling has been widely utilized in the design of planar integrated bandpass filters.

Next, the J-inverter network with the extracted circuit parameters is further transformed into its scattering matrix to investigate its frequency-dependent electrical behavior. The return loss $|S_{11}|$ can be easily derived in terms of J-inverter susceptance (J) and the characteristic admittance (Y_0) of external microstrip lines on a basis of the circuit model as in Figure 4.1(c).

$$|S_{11}| = \frac{Y_0^2 - J^2}{Y_0^2 + J^2} \tag{4.1}$$

Interestingly, the operating frequency where $J/Y_0=1$ strictly corresponds to the pole location over a bandpass range. With the use of Equation(4.1), we can observe that the return loss S_{11} becomes extremely small at the frequency where the parameter (J/Y_0) is close to 1. This frequency-dependent periodicity of (J/Y_0) with the peak value close to 1 provides us with a hint to construct a novel microstrip bandpass filter which bandpass behavior can be formulated by an extremely tight coupling strength of the AC-PCML structure.

Figure 4.3 gives the predicted return/insertion losses of the PCML with the relatively wide aperture width of $W_a=2.2mm$ & *3.0mm*, through the use of extracted J-inverter

susceptance in Figure 4.2(a). The predicted results show clearly the perfectly bandpass filtering behavior with one-pole and two-pole frequency locations, respectively. This initial result demonstrates that the frequency-distributed J-inverter susceptance itself can generate its own frequency passband around the operating frequencies where the normalized (*J/Yo*) achieves its maximum value and is close to 1. In the meantime, it can be understood from the $|S_{11}|$ curves in Figure 4.3 that the small (*J/Yo*) at the high frequency can be utilized to formulate a wide high-stop band.

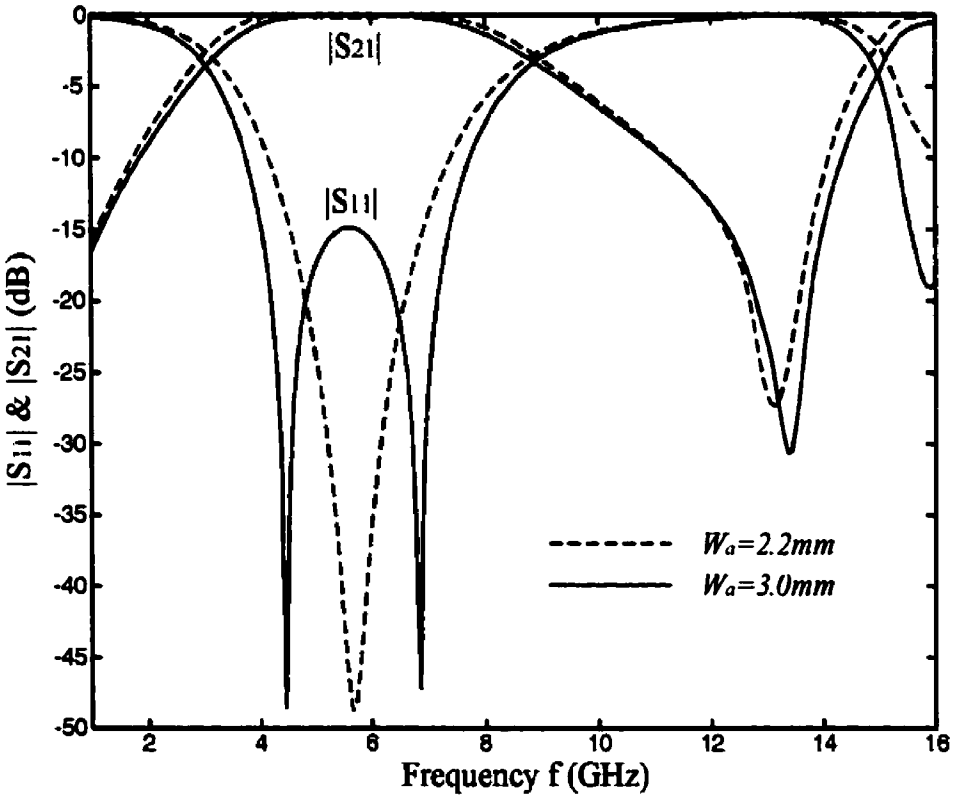

Figure 4.3 Predicted insertion and return losses (S21 & S11) of the two-port AC-PCML calculated from the extracted J-inverter susceptance plotted in Figure 4.2(a).

To realize the bandpass behavior with the sharply changed configuration, our following research task will be focused on the original proposal and extensive investigation of a new class of multi-pole microstrip bandpass filters with the size miniaturization and

broad pass bandwidth. It is achieved by utilizing the PCML's J-inverter susceptance as well as the first- and second-order resonant modes in a microstrip line resonator.

4.3. Concept and Model-Based Design of Prototype Bandpass Filter

Figure 4.4 (a) depicts the schematic layout of the prototype microstrip bandpass filter proposed here. In this filter structure, a single uniform microstrip line section with the same strip width as that of external microstrip line is arranged at the central location and is sandwiched between two sections of identical AC-PCML. This filter structure is formed for achieving ultra-broadband and multi-pole bandpass filtering behavior.

The central uniform line section has the length of about one quarter-wavelength at the central frequency and acts as a partial section of the equivalent line resonator located between such two AC-PCML sections. According to the above discussion on the single AC-PCML structure, we can deduce that the total filter length is slightly shorter than three times its quarter-wavelength, that is, $0.5\lambda_{g0}<(D+L+D)<0.75\lambda_{g0}$, where λ_{g0} is the guided-wavelength of the microstrip line at the central frequency.

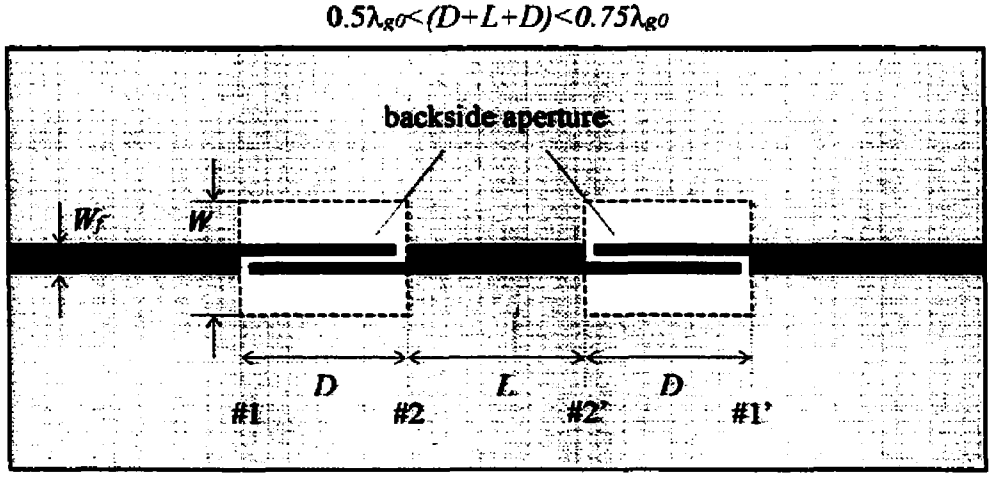

(a) layout

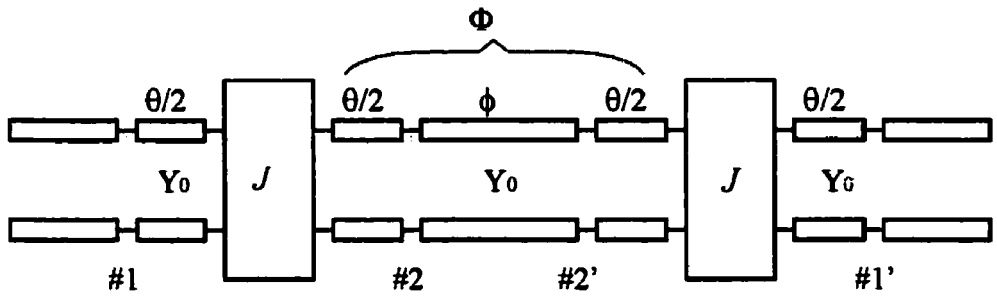

(b) equivalent circuit model

Figure 4.4 Schematic layout and its equivalent circuit topology of the proposed multi-pole bandpass filter with a single uniform line resonator.

Figure 4.4(b) presents its complete equivalent circuit topology, arranged for gaining physical insight into its operating mechanism and also allowing the efficient circuit network based optimization of this proposed filter. As described above, the AC-PCML section is characterized as a J-inverter susceptance (J) and two electrical lengths ($\theta/2$), representing its series capacitive coupling and equivalent phase shifts, respectively. On the other hand, the central uniform line can be perceived as an additional phase factor (ϕ) so that the total electrical length (Φ) should be made up of three separate parts, that is, $\Phi=\theta/2+\phi+\theta/2$, to form an electrically equivalent line resonator. This line resonator is formulated here to generate two additional bandpass poles from its first- and second-order resonant modes, corresponding to the cases of $\Phi=180$ and *360 degree*.

To investigate its frequency-dependent electrical behavior, let's start with the characterization of its two-port equivalent cascaded circuit topology as shown in Figure 4.4(b). On the basis of a transmission line theory, the input admittance (Y_{in}) at one termination (#1), looking into its opposite termination (#1'), can be easily deduced and expressed as a closed-form function of J, Y_0 and Φ such that

$$Y_{in} = \frac{J^2\left(Y_0^2 + jJ^2 \tan\Phi\right)}{Y_0\left(J^2 + jY_0^2 \tan\Phi\right)} \tag{4.2}$$

Accordingly, its reflection coefficient (S_{11}) at #1 can be further simplified as follows to help a better understanding of its fundamental filtering performance.

$$S_{11} = \frac{j\left(Y_0^4 - J^4\right)\cdot tan(\Phi)}{2J^2Y_0^2 + j\left(Y_0^4 + J^4\right)\cdot tan(\Phi)} \tag{4.3}$$

Considering the fact that the band-pass pole is usually defined as a frequency point where $|S_{11}|=0$ or $|S_{11}|$ achieves a minimum value, it is understood from Equation (4.3) that there exist multiple poles of frequency where $\Phi = 180^0$, $\Phi = 360^0$ and $J = Y_0$. The former two poles correspond to the first- and second-order resonant frequencies and we can find in the following that the frequency spacing between them basically forms a desired ultra-broad bandwidth of the filter. The latter one or two poles are contributed by highly enhanced J-inverter susceptance ($J=Y_0$) and they need to be arranged around the central operating frequency through suitable choice of the line length (L) in Figure 4.4(a).

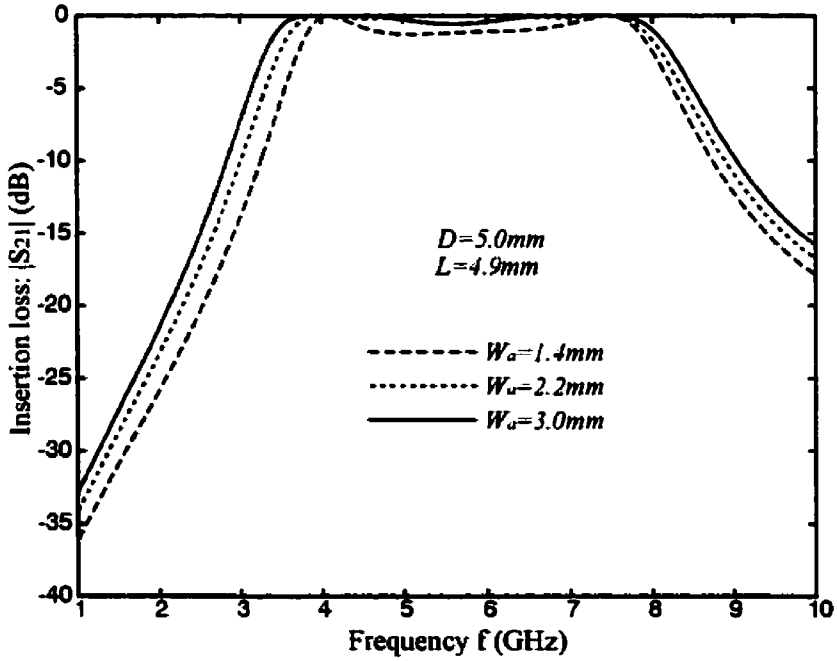

(a) insertion loss $|S_{21}|$

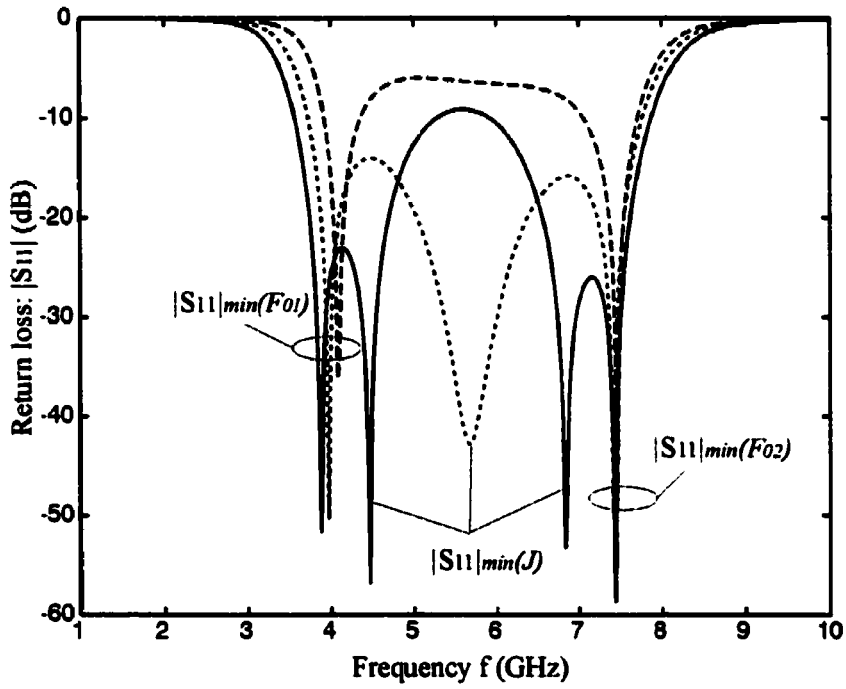

(b) return loss $|S_{11}|$

Figure 4.5 Predicted frequency response of the filter layout as described in Figure4.4 with different aperture widths W_a.

Figure 4.5(a) and (b) describe the predicted frequency response of the microstrip bandpass filter with the aperture length of $D=5.0mm$ and the central line length of $L=4.9mm$ over the frequency range ($f=1.0$ to 10.0 GHz). These results are obtained from Equation (4.3) via three groups of extracted J-inverter network parameters in Figure 4.2 and utilized here to exhibit the bandpass behavior inside its dominant passband. In the case of a relatively narrow aperture width ($W_a=1.4mm$), only two poles can be observed. They appear at the half- and full-wavelength resonant frequencies, marked by F_{01} and F_{02} and correspond to those of $\Phi = 180^0$ and $\Phi = 360^0$, respectively.

The maximum J in this case is found from Figure 4.2(a) to attain about $0.8Y_0$, indicating a relatively weak coupling. This leads to a worse bandpass behavior with the maximum

return loss of $|S_{11}|$=-6.0dB between two resonant frequencies (F_{01} and F_{02}) in the absence of any additional pole brought by the condition: $J=Y_0$.

As W_a is widened to 2.2mm, $|S_{11}|$ rapidly falls down and its entirely frequency-dependent pattern is separated into two parts with respect to an additional pole (minimum value) around the central location. Meanwhile, $|S21|$ gradually rises up close to its 0-dB level in the frequency range sandwiched between F_{01} and F_{02}. With reference to Figure 4.2(a), this additional pole is physically generated by the maximum value of its normalized J-inverter susceptance where J is close to Y_0. As W increases further to 3.0mm, it can be observed from Figure 4.5(b) that one pole is split into two poles at the two sides of the central frequency within the passband.

Due to the maximum $J>Y_0$ in this case, the two frequencies where $J=Y_0$ can be found from Figure 4.2(a) and they lead to the emergence of these two additional poles via Equation (4.3). Unfortunately, the return loss $|S_{11}|$ shifts up slightly in the central location that degrades its whole band-pass behavior due to its extremely enhanced coupling degree, e. g. $J>>Y_0$. Nevertheless, this problem can be solved by suitably adjusting the backside aperture width of the AC-PCML to meet the requirement of its J-inverter susceptance in optimization procedure.

So far, the operating mechanism of the proposed multi-pole bandpass filter with a single line resonator has been explained on the basis of equivalent J-inverter circuit theory and its filtering behavior has been characterized by a closed-form equation. Next, our interest is to optimally design its frequency response in order to achieve the much low return loss over the frequency passband.

Figure 4.6 gives the optimized results of the filter having the same dimension as in Figure 4.4(a) except a different aperture width (W_a=2.5mm). In this case, we find out that $J=1.05Y_0$ (maximum) effectively reduces the return loss $|S11|$ to –17.0 dB from

about *-9.0 dB* as illustrated in Figure 4.5(b) for the case of W_a*=3.0mm*. Similarly, the four poles also appear within the pass band, allowing the design of ultra-broad and flat bandpass electrical behavior with an insertion loss of $|S_{21}|$*>-0.2dB* within the broad frequency passband (*f=3.8* to *7.8 GHz*).

Otherwise, we can clearly observe from the predicted frequency response over a wide frequency range (*1.0* to *16.0 GHz*) in Figure 4.6 that a parasitic harmonic passband with a very narrow bandwidth appears around *f=11.8 GHz*. This is contributed by the third-order resonant frequency of the central uniform line resonator and degrades its high-stop filtering behavior. This problem will be solved through the attachment of a pair of open-end microstrip stubs in the shunt form.

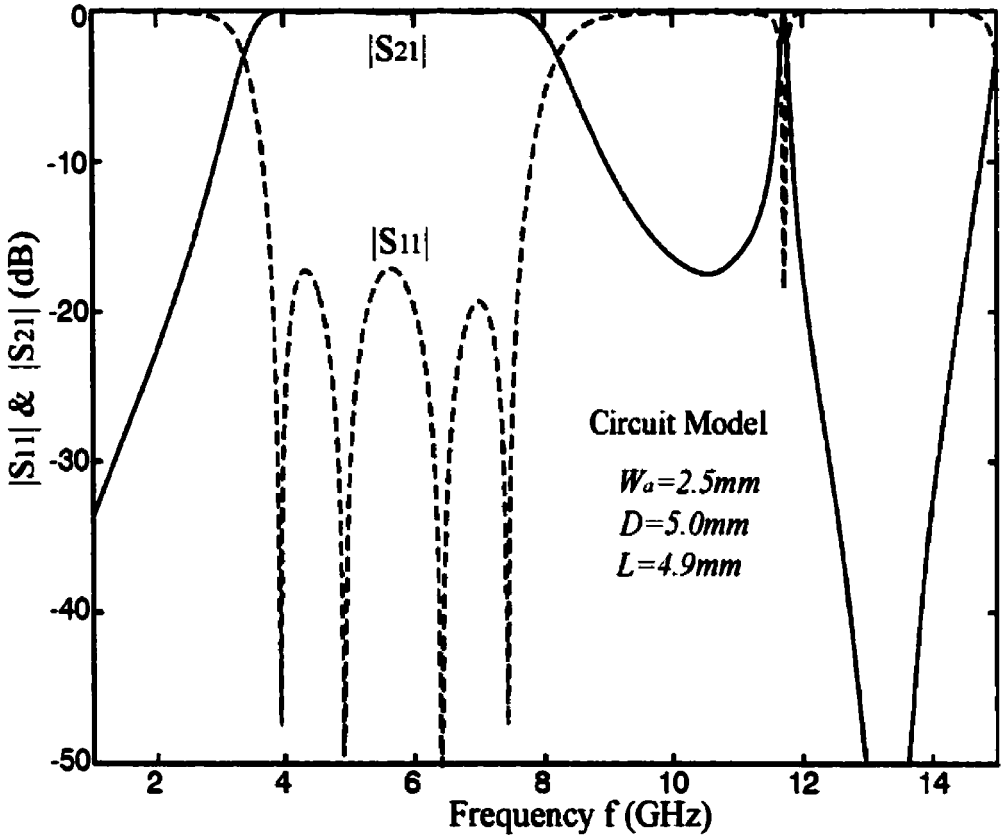

Figure 4.6 Optimized frequency response of the prototype multi-pole bandpass filter.

4.4 FULLWAVE CHARACTERIZATION OF PROTOTYPE BANDPASS FILTER

To verify our predicted results from its equivalent circuit model, the commercial *HP Momentum software* is utilized for fullwave EM characterization of the entire filter layout and optimal design of its ultra-broad bandpass behavior under the designated goal of much low return loss within the dominant frequency passband. Due to its ability in automatically choosing the mesh number and freely choosing the rectangular and/or triangular mesh configuration, this EM software is very powerful for accurate simulation of the entire filter layout at the cost of long CPU time and large CPU memory.

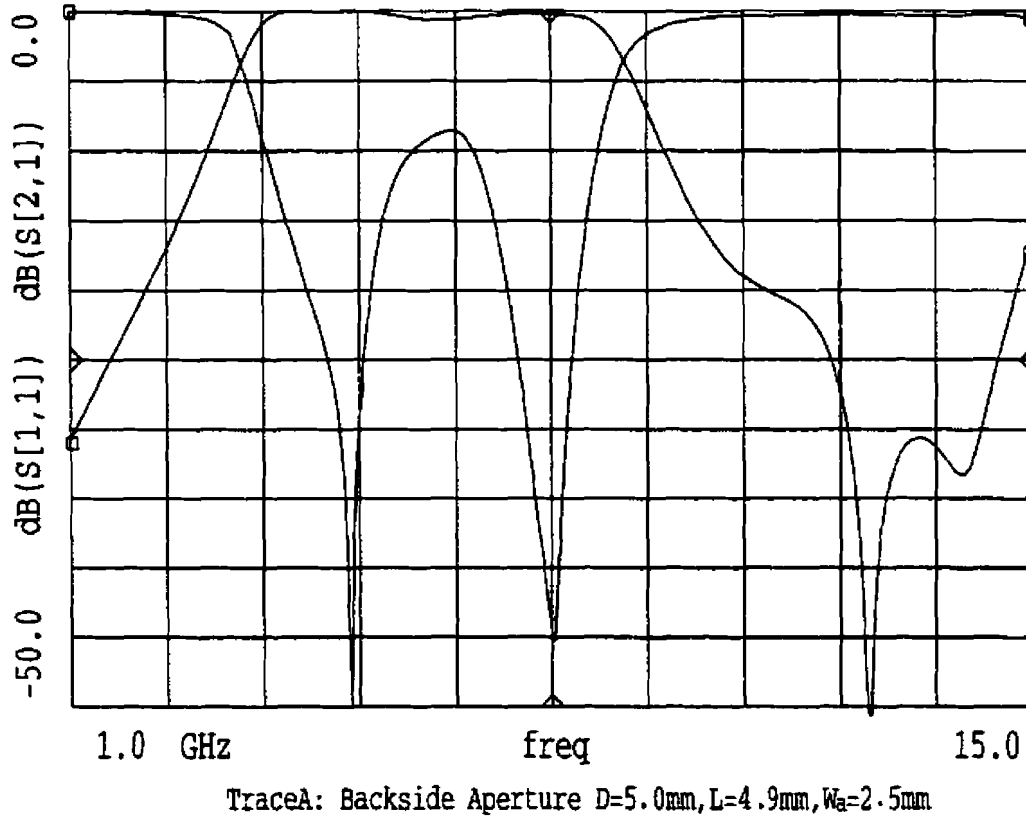

Figure 4.7 Predicted frequency response of the prototype bandpass filter with the same aperture width (W_a=*2.5mm*) as in Figure 4.4, from the HP Momentum.

As for the filter layout as illustrated in Figure 4.6, it takes us about 4 to 5 hours per frequency so that the simulation of its frequency response over the wide frequency range (*1.0* to *15.0 GHz*) is completed by spending about two days or 40 to 50 hours. It is basically caused by an increasingly large number of non-uniform rectangular and triangular meshes, which are separately chosen to represent the electric current density over the strip conductor and the equivalent magnetic current density over the backside aperture, respectively, at the two different layers.

Figure 4.7 shows the predicted frequency response of this microstrip bandpass filter with the completely same dimension as that optimized with its circuit model as illustrated in Figure 4.4, in which W_a=*2.5mm*. This result is obtained from the HP momentum software and illustrates the reasonably similar configuration to that in Figure 4.6, over the wide frequency range.

However, we can observe some visible difference between them. The lower and upper cutoff frequencies of the dominant passband are found from Figure 4.7 about *3.7* and *9.0 GHz* as compared with *3.8* and *7.8 GHz* in Figure 4.6, showing the slight shift-up of its passband. Furthermore, its return loss (S_{11}) just achieves the maximum value of about *–8.2 dB* with only two poles within the passband.

By looking at the three groups of model-based frequency responses in Figure 4.5(b), it may be attributed to the too tight coupling of the AC-PCML section. It is caused by the free choice of non-uniform mesh configuration over the two-coupled strip conductors in the HP Momentum rather than our model based software. In this case, the electric or magnetic current density along the transverse orientation of these two narrow strip conductors or backside aperture can be accurately simulated to take into account the AC-PCML's coupling behavior. Otherwise, the parasitic harmonic pass-band appears so small to be ignored in this simulation.

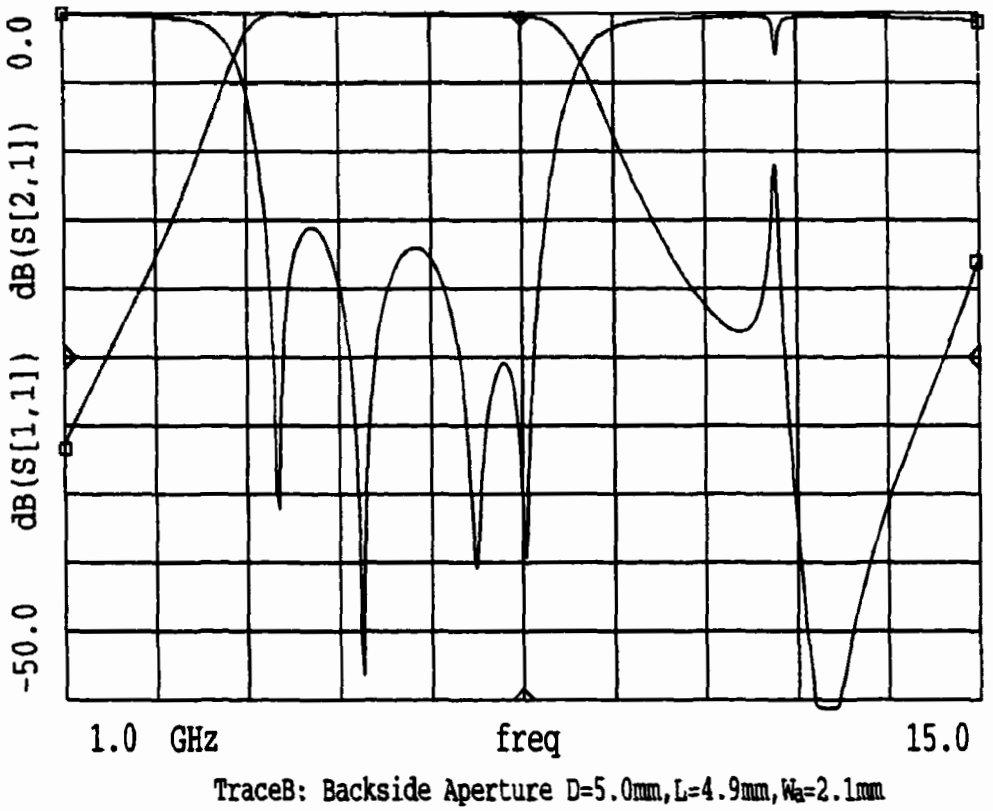

Figure 4.8 Optimized frequency response of this bandpass filter with aperture width (W_a=*2.1mm*).

Next, the optimization design is carried out by suitably adjusting the aperture width (W_a) towards the realization of much low return loss with the dominant passband. In our simulation, we find that the return loss (S_{11}) inside the pass-band at first falls down and then rises up again with three or four poles as W_a is narrowed. Figure 4.8 is the optimized frequency response of this band-pass filter in the case of W_a=*2.1mm*, showing the very similar filtering behavior as in Figure 4.6. Here, we can clearly observe the four band-pass poles within the pass-band and a parasitic harmonic pass-band around *f=11.9 GHz*.

Also, its maximum S11 achieves about –16.0 dB much better than –8.2 dB in the initial simulated results as in Figure 4.7. In the following, we will focus our attention on a

possibility of suppressing the spurious harmonic passband by attaching a pair of capacitively open-end microstrip stub into the line resonator.

4.5 Concept and Model-Based Design of Improved Band-pass Filter

As well known in the microwave engineering, harmonic resonant frequencies of a uniform microstrip line resonator are approximately equal to two or three times of its fundamental resonant frequency. To implement the suitable adjustment of its resonant frequency spectrum, the non-uniform line resonator has been well found as one of the powerful candidates a few years ago by forming the strip configuration with changed width and/or attached stub.

In this case, a specific non-uniform microstrip line resonator, called by "stepped impedance resonator" (SIR), was presented and applied for the design of a parallel-coupled stripline bandpass filter with a wide upper stop-band and a good harmonic suppression. This line resonator is made up of cascaded transmission line sections having different characteristic impedance. This arrangement is made to shift up its first-order harmonic resonant frequency by suitably choosing the impedance ratio of two different line sections. As a result, this SIR allows realizing well a broad rejection-band between its fundamental and spurious harmonic pass-band in the filter.

According to the extensive characterization and physical investigation of the prototype bandpass filter in the above section, we can understand in depth that the first harmonic passband in our filter is attributed to the third-order resonant frequency of the line resonator. In the meantime, the useful dominant passband is formulated between the fundamental and second-order resonant frequencies. From the basic concept of the SIR bandpass filter, it is our purpose and also a critical point in the realization of a perfect bandpass filter to build up a non-uniform microstrip line resonator by separating at utmost its second- and third-order resonant frequencies.

$0.5\lambda_{g0}<(D+L+D)<0.75\lambda_{g0}$

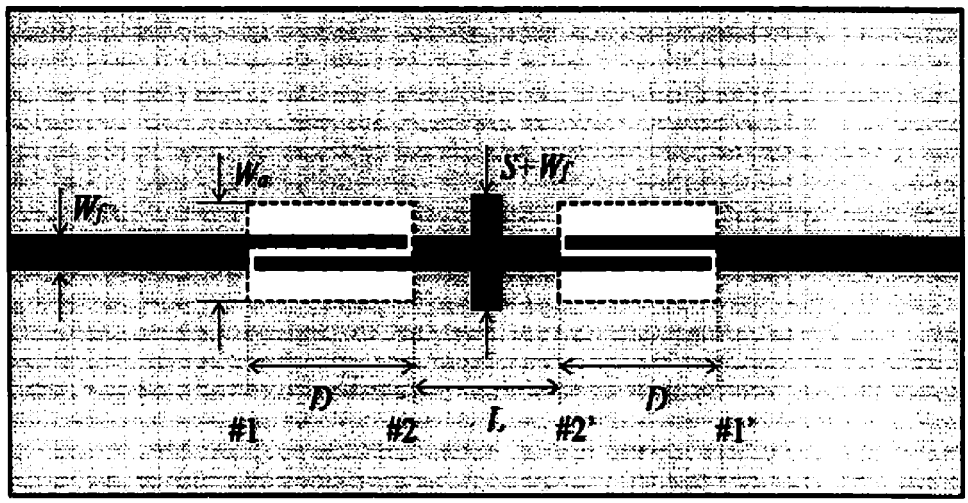

(a) layout

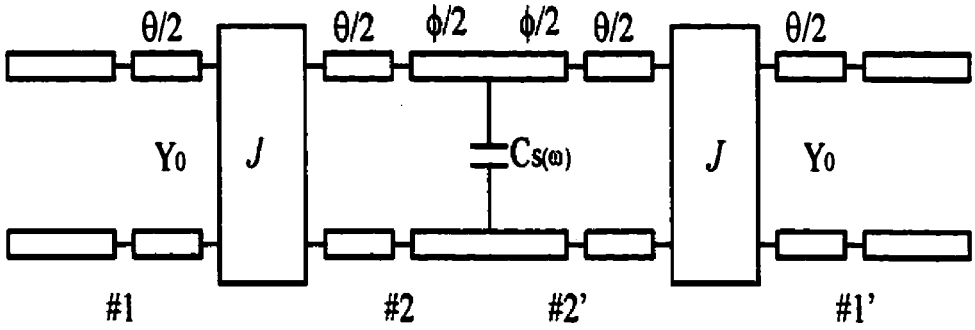

(b) equivalent circuit model

Figure 4.9 Schematic layout and its equivalent circuit topology of the improved Bandpass filter with a single capacitive-loaded line resonator.

Figure 4.9(a) depicts the schematic layout of an improved AC-PCML bandpass filter with a non-uniform line resonator at its central part. This line resonator is constructed by attaching in shunt a pair of capacitively open-end stubs at the central location of such a line section. Figure 4.9(b) is its equivalent circuit topology, in which such a pair of stubs can be perceived as an equivalent quasi-lumped shunt capacitance *Cs* at low frequency and a capacitively frequency-distributed shunt susceptance (jB_s) as the frequency increases to some extent.

To our knowledge, the central location of this line resonator represents strictly the perfect short- and open-circuit terminals for the first-/third-order (odd-order) resonant modes and for the second-/fourth-order (even-order) resonant modes, respectively. The attachment of such a pair of stubs is expected to lower effectively the second-/fourth-order or even-order resonant frequencies while the first-/third-order or odd-order resonant frequencies remain almost unchanged.

Following its equivalent circuit model as in Figure 4.9(b), we can characterize its overall frequency response over the wide frequency range in an explicit and efficient format. First of all, the input impedance (Y_a) at the location of an shunt susceptance (jB_s), looking into one terminal (*#1'*), can be obtained as a function of Y_0 and $(\phi+\theta)/2$,

$$Y_a = Y_0 \frac{J^2 + jY_0^2 \tan(\phi+\theta)/2}{Y_0^2 + jJ^2 \tan(\phi+\theta)/2} \tag{4.4}$$

By considering the shunt susceptance (jB_s), the final input impedance (Y_{in}) at the terminal (*#1*), looking into the opposite terminal (*#1'*) can be derived as below,

$$Y_{in} = \frac{J^2[Y_0 + j(Y_a + jB_s)\tan(\phi+\theta)/2]}{Y_0[(Y_a + jB_s) + jY_0 \tan(\phi+\theta)/2]} \tag{4.5}$$

Accordingly, the return loss (S_{11}) and insertion loss (S_{21}) can be solved in terms of a simple function of Y_{in} and Y_0. On the other hand, the first-/third-order (odd-order) and the second-/fourth-order (even-order) resonant frequencies of such a non-uniform line resonator can be obtained under the condition of the perfectly short-circuit and open-circuit terminals at the central location depicted above. They are satisfied with the following simple equations under the assumption of the AC-PCML's coupling degree, e. g., $J=0$.

$$\phi + \theta = n\pi \qquad \text{(odd-order modes: } n=1, 3\text{)} \qquad (4.6)$$

$$\phi + \theta = n\pi - tan^{-1}\left(\frac{B_s}{Y_0}\right) \qquad \text{(even-order modes: } n=2, 4\text{)} \qquad (4.7)$$

From Equation (4.6) and (4.7), we can understand well that the attached stubs reduce the second- and fourth-order resonant frequencies as the capacitive susceptance (jB_s) increases and hardly give any influence on the first- and third-order resonant frequencies. Next, we make a further investigation on this resonant behavior according to the simulated frequency response of the whole filter layout with different stub length (S) under the weakly coupled case.

Figure 4.10(a) and (b) depict the predicted frequency response of the filter layout with a fixed aperture as shown in Figure 4.9(a) versus three different stub lengths. They are obtained on the basis of an equivalent circuit topology as in Figure 4.9(b) for a relatively weak coupling, e. g., $J<<Y_0$, which is arranged to demonstrate the complete frequency spectrum of the first four resonant modes for the non-uniform microstrip line resonator. First of all, we observe that the first- and third- (odd) resonant frequencies, F_{01} and F_{03}, remain stationary even though the stub length is extended to a great extent, which can be interpreted from Equation (4.6).

Also, it is well valid in theory because the central location corresponds to a perfect short circuit with an extremely large admittance. Second, the second- and fourth- (even) resonant frequencies, F_{02} and F_{04}, are found to simultaneously fall down towards the first- and third-order counterparts as the stub length (S) is extended. As a result, the rejection band of interest can successfully be tuned from *4.2 GHz* to *7.0 GHz* while the fundamental pass bandwidth drops down significantly from *3.2 GHz* to *0.8 GHz*. Thus, the attachment of such a pair of capacitive stubs brings a possibility of realizing a broad bandpass filter with a good harmonic suppression as well as easy-to-tune broad

frequency bandwidth around *15%* to *70%*, which can be roughly estimated from Figure 4.10.

Further, we can predict from its much low return loss characteristic $|S_{11}|<-20\ dB$ in a weakly coupled case of the stub length $S=4.8mm$ that the capacitive shunt stubs may allow us to greatly alleviate the strict requirement of an extremely tight coupling. It indicates us that such a compact bandpass filter can be designed with relatively narrow bandwidth ($BW<70\%$) and wide upper stop-band by using the relatively weakly coupling, e. g., $J<Yo$.

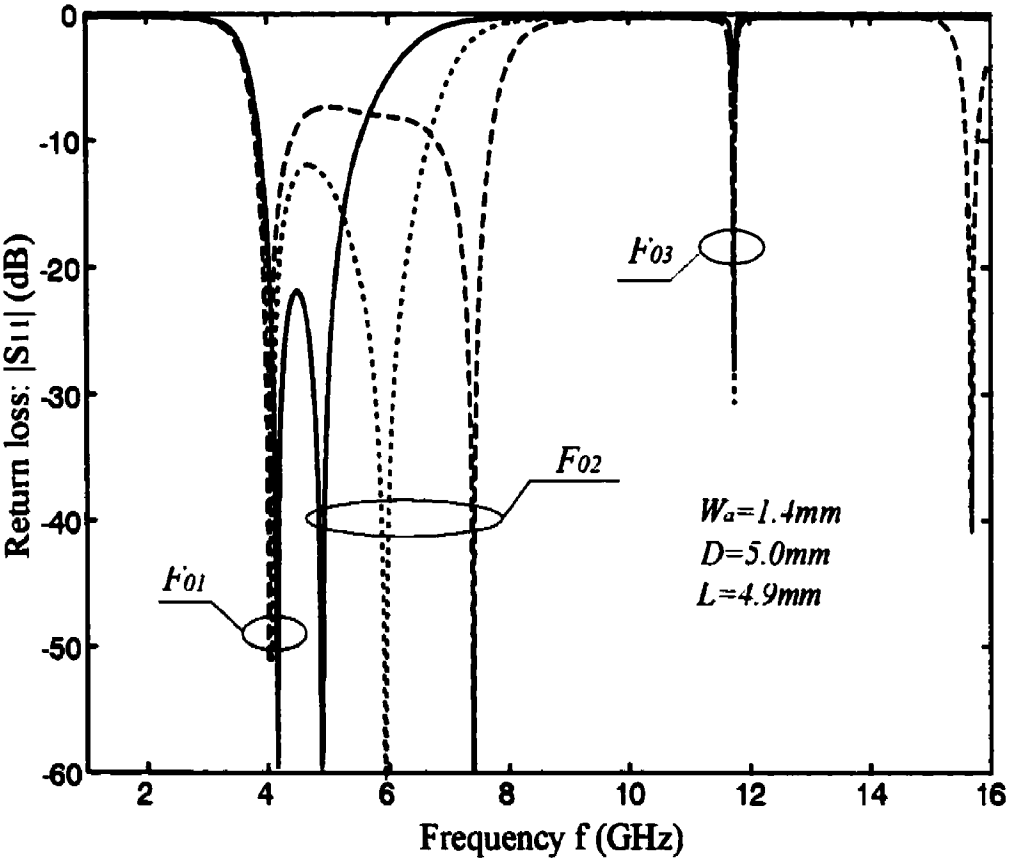

(a) return loss (S_{11})

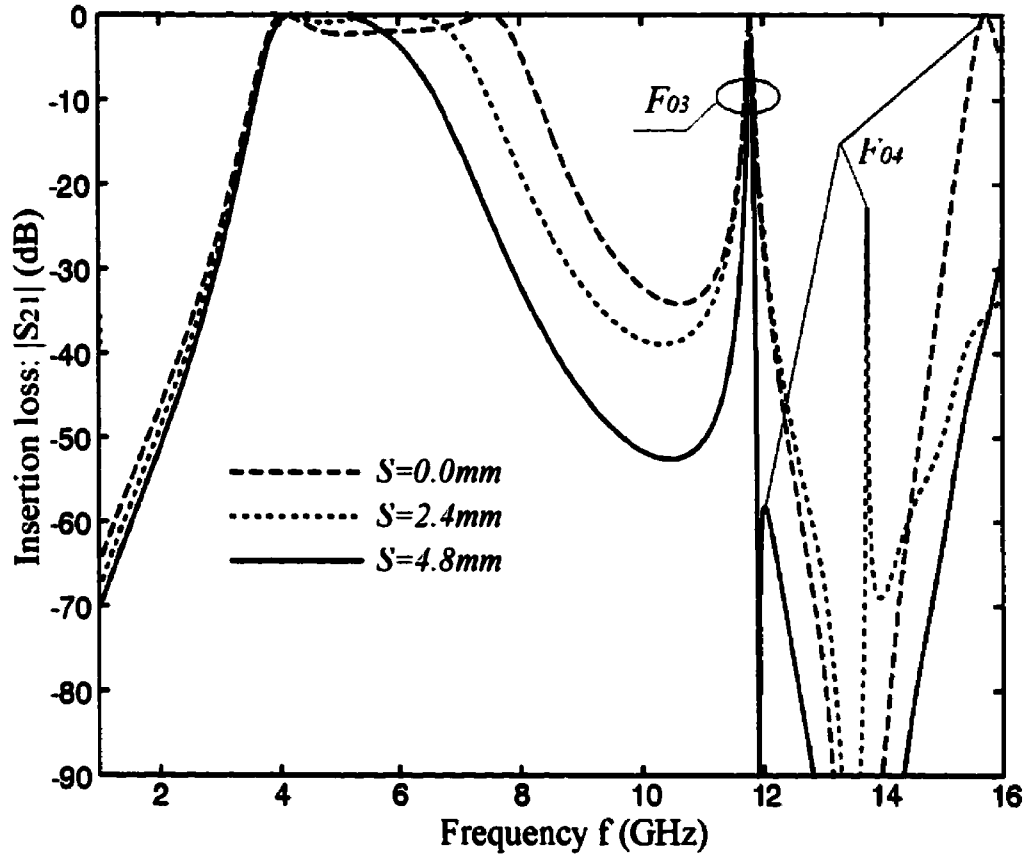

(b) insertion loss (S_{21})

Figure 4.10 Predicted frequency response of the filter layout with different stub length.

Now, let's turn to the optimal design of a four-pole band-pass filter with a single stub-loaded resonator through the equivalent circuit as in Figure 4.9(b), towards the realization of much low return loss within the dominant pass-band and also good harmonic pass-band suppression at the upper-band.

Figure 4.11 presents the optimized frequency response of this stub-loaded bandpass filter with the stub length (S=*2.08mm*) over a wide frequency range (*1.0* to *15.0 GHz*). It shows us an excellent broad band-pass behavior with the bandwidth of about *60%* and the return loss of $|S_{11}| < -30$ *dB*. Also, the four-poles can be clearly observed from Figure 4.11. In this case, a spurious harmonic pass-band with an extremely narrow

bandwidth appears around *f=14.0* GHz, exhibiting a much wider up-band of rejection with the bandwidth of *BW= 100%*, regarding to its central operating frequency *fo=6.0 GHz*.

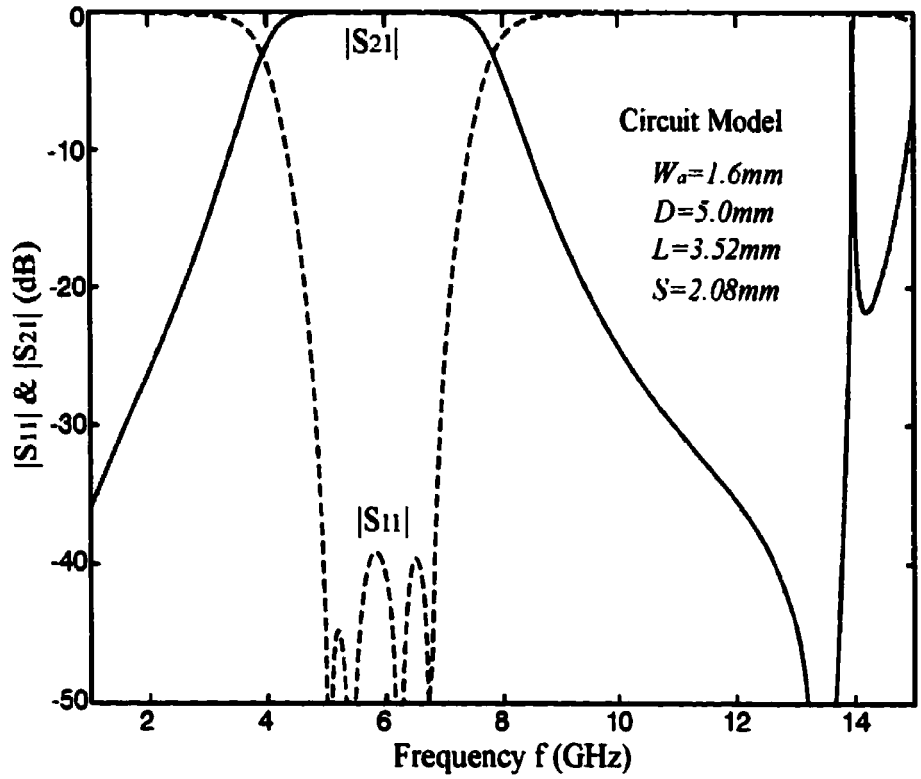

Figure 4.11 Optimized frequency response of the filter layout with the stub length (*S=2.08mm*).

4.6 Numerical & Experimental Investigation of Improved Bandpass Filter

To develop this band-pass filter with such attractive electrical features, HP Momentum software is further utilized to simulate this entire filter layout by considering all the inter-coupling effects and also field distribution over the coupled-strip conductor with narrow width. The optimization design is then carried out towards the goal of much return loss within the broad pass and wide up-band rejection by suitably adjusting the central line length (*L*), stub length (*S*) and aperture width (W_a) in a slightly and

simultaneously varied manner. In this case, our optimization procedure starts with the whole dimension of this filter layout as illustrated in Figure 4.11, except the backside aperture width (W_a=*1.4mm*), and then determines the layout dimension for filter fabrication.

In the above model-based characterization and optimization of this band-pass filter using its equivalent circuit model as illustrated in Figure 4.9(b), the microstrip four-port cross-junction discontinuity at the central location of this filter is completely ignored, thereby leading to somewhat unavoidable influence on its predicted electrical behavior. After some numerical simulation is initially implemented using the HP momentum software, we find that the stub length (S) and the line length (L) should be simultaneously selected a little long and short as opposed to those as shown in Figure 4.11. Such a choice is made to achieve the low return loss within the passband in the HP Momentum simulation.

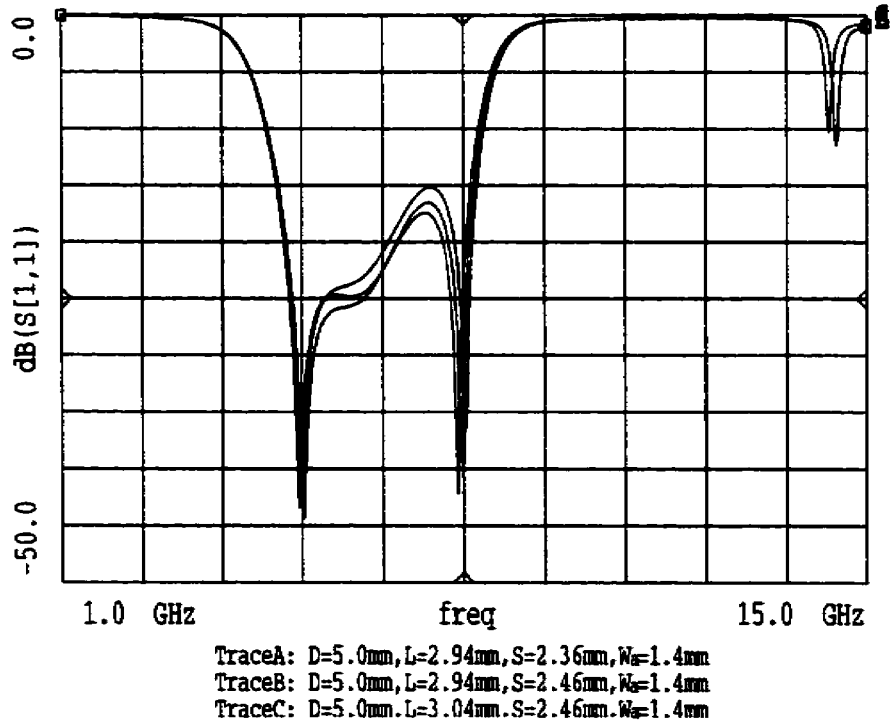

(a) return loss (S_{11})

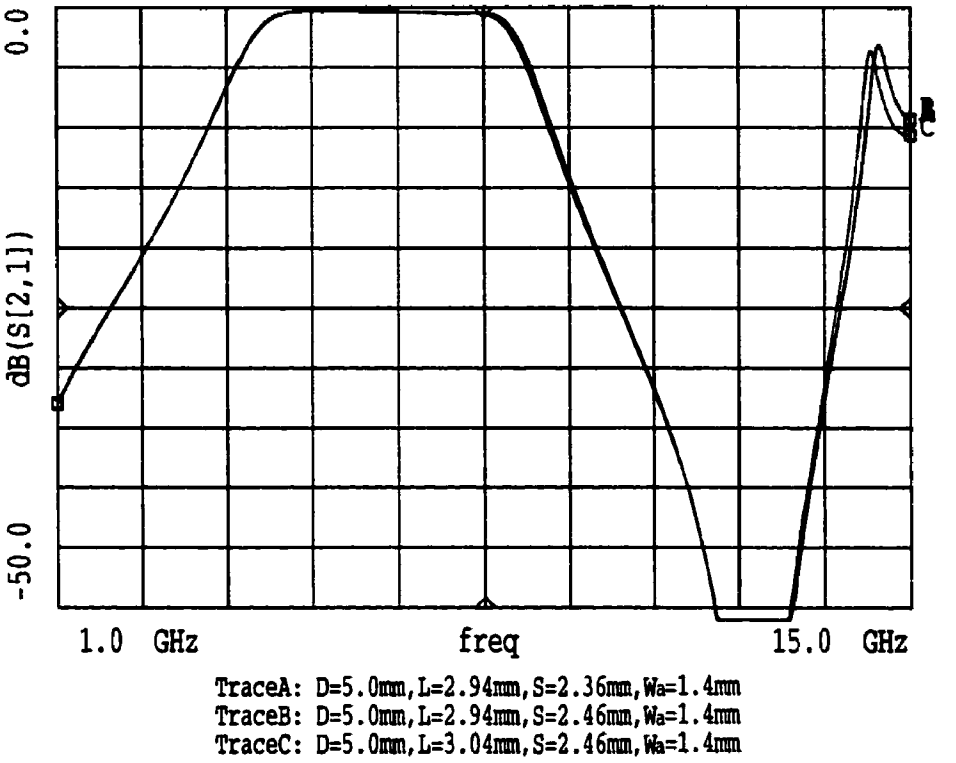

(b) insertion loss (S_{21})

Figure 4.12 Simulated frequency response of the band-pass filter using the HP Momentum software: Group (I)

Fig 4.12 presents the first group of simulated frequency response for the band-pass filter with different dimensions (L & S) under the fixed aperture length (D=*5.0mm*), marked by "Group (I)". Three different cases correspond to the Trace A (L=*2.94mm* & S=*2.36mm*), Trace B (L=*2.94mm* & *2.46mm*) and Trace C (L=*3.04mm* & S=*2.46mm*), respectively. All the three simulated results exhibits the appearance of the broad passband behavior at the central frequency of about f=*6.6 GHz* and a harmonic upper-passband around f=*14.4 GHz*.

Also, we can observe that all the three return losses (S_{11}) appear an asymmetrical frequency-related configuration within the dominant passband. By extending very slightly its stub length (S) from *2.36mm* to *3.46mm*, the maximum S_{11} is found to fall

down from about *–15.0* to *–17.0 dB* and its harmonic upper-passband tends to be shifted downwards to some extent. Figure 4.12(b) shows that the minimum insertion losses (S_{21}) are better than *–0.4 dB* and appear around the upper frequency range within the passband, attributed to the limited Q-factor of the microstrip line. Otherwise, they have almost same frequency-related configuration for all the three cases.

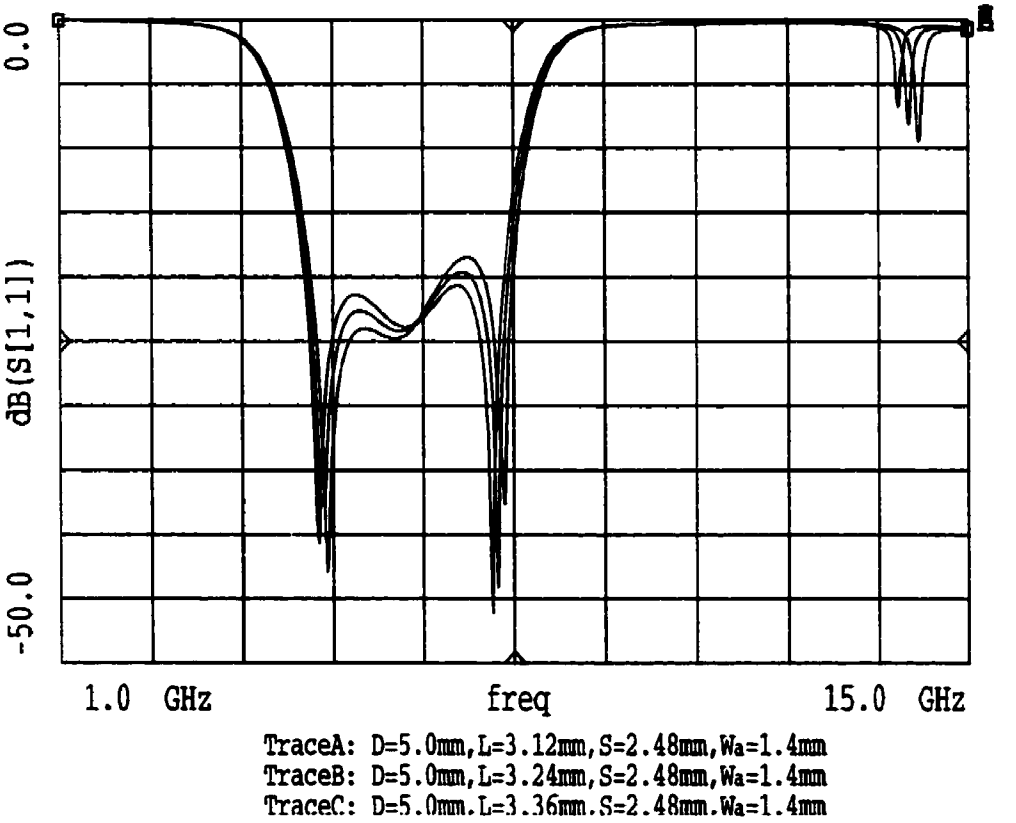

(a) return loss (S_{11})

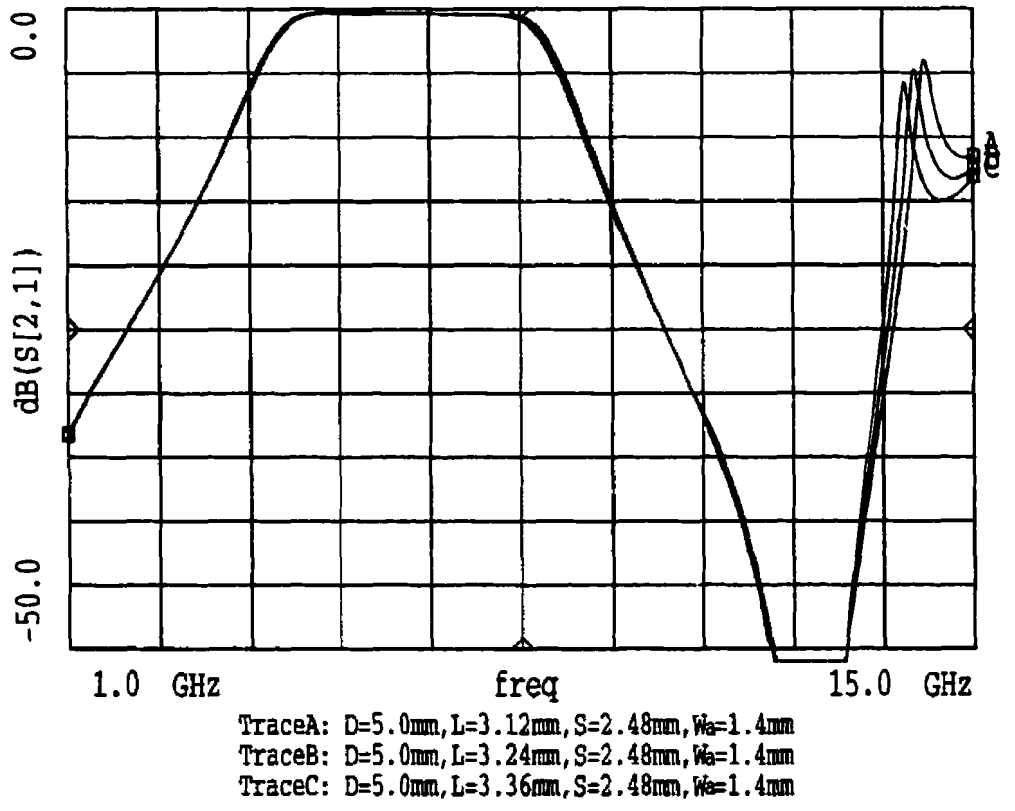

(b) insertion loss (S_{21})

Figure 4.13 Simulated frequency response of the bandpass filter using the HP Momentum software: Group (II)

Figure 4.13 describes the second group of simulated frequency response of this band-pass filter, marked by "Group (II)", obtained in the HP momentum calculation through the choice of the line length (*L=3.12, 3.24, 3.36mm*) under the fixed *S= 2.48mm and Wa=1.4mm*. As *L* increases, the bandwidth of the dominant passband tends to be slightly narrowed by about 2.0% from *65.0%* to *63.0%*. We can observe from Figure 4.13(a) that the return loss (S_{11}) within the pass-band gains a visible improvement in achieving a good symmetrical shape and also in reducing its maximum value from about *–17.2 dB* to *-20.7dB*. Otherwise, the spurious pass-band seems to shift downwards gradually as *L* is extended.

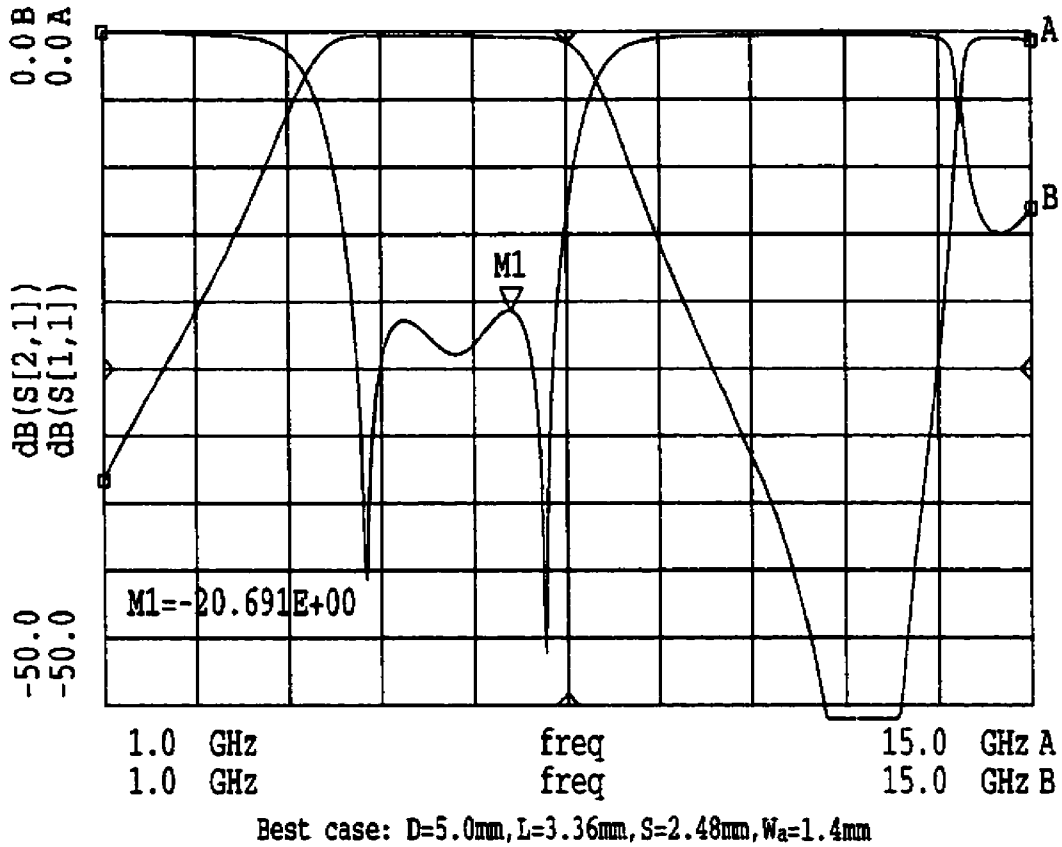

Figure 4.14 Optimized frequency response of this bandpass filter using the HP Momentum software

To take a close look at the best case of these frequency responses, Figure 4.14 plots the simulated result again with regard to the case of Trace C (*L=3.36mm*) as illustrated in Figure 4.13. As opposed to the optimized frequency response of the prototype band-pass filter in Figure 4.8, this optimized result exhibits that the attachment of such a pair of capacitive stub brings a great improvement in its whole filtering behavior. Its spurious upper-passband is significantly shifted upwards far away from its dominant pass-band of our interest, showing the wide and deep spurious up-band rejection. According to our above description, it can be well understood that such capacitive open-end stubs lead to the enlargement of difference between the second- and third-order resonant frequencies of the central line resonator.

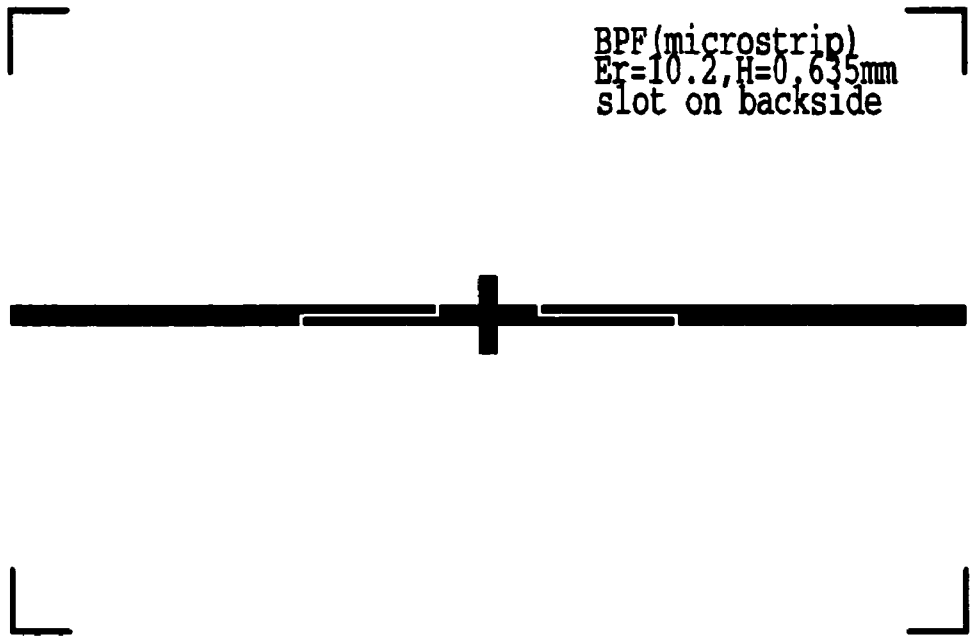

(a) upper-layer

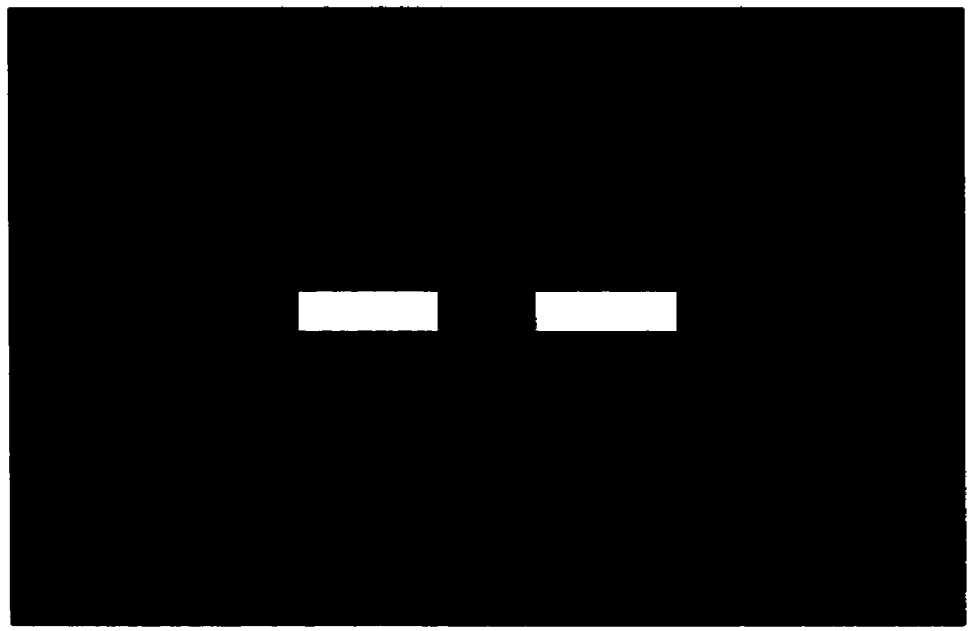

(b) bottom-layer

Figure 4.15 Upper- and bottom-layer configration of an improved microstrip band-pass filter arranged for etching fabrication.

To verify our optimized frequency response with several attractive features, a band-pass filter sample is fabricated with the whole layout dimension determined by our optimized design (Trace C). Figure 4.15 (a) and (b) show the upper- and bottom-layer configuration of this filter arranged for etching fabrication. Following the above description on the operating mechanism of prototype and improved bandpass filters, we can see from Figure 4.15 that the shortening of the central line section with the loaded-stub leads to the miniaturization of the whole filter layout. It also allows us designing and developing the size-compact and low-cost microstrip bandpass filter with several distinct electrical behaviors as shown above. In this case, the total length of this stub-loaded bandpass filter ($D+L+D=13.36mm$) is much shorter than its guided-wavelength, that is, about $0.7\lambda_{g0}$, at the central frequency of $f_0=6.1GHz$.

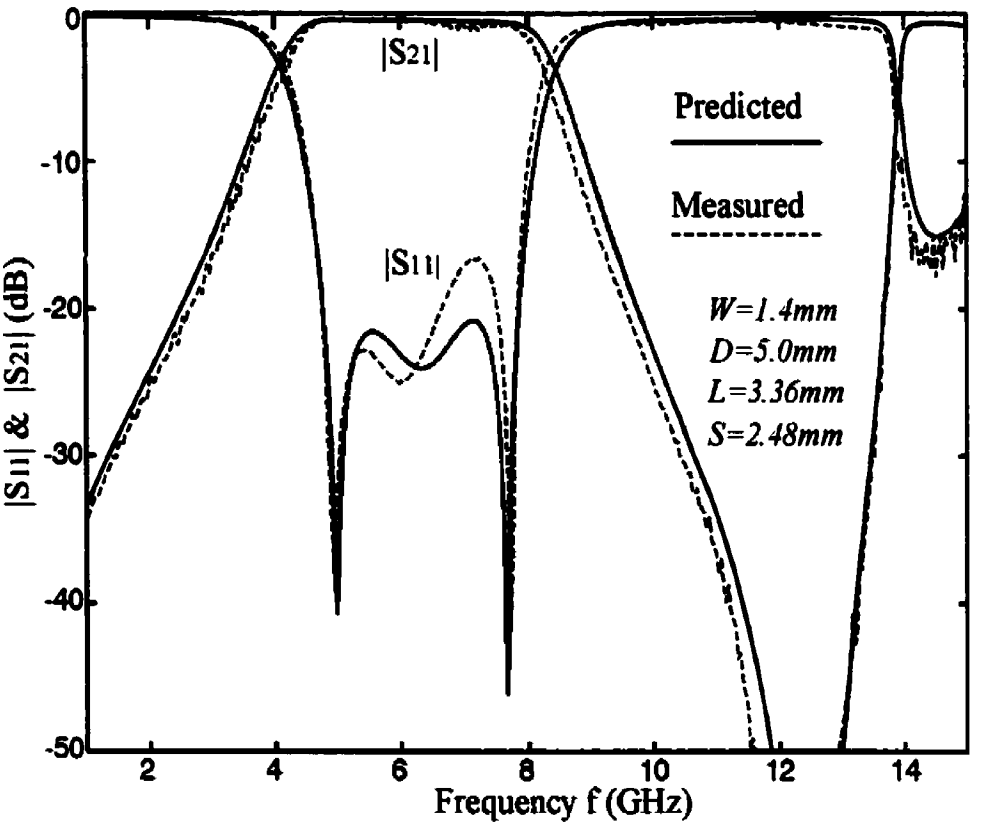

Figure 4.16 Comparison of predicted and measured frequency response of the improved bandpass filter with completely same dimension.

Figure 4.16 depicts the measured frequency response of the fabricated filter sample over the wide frequency range (*1.0* to *15.0 GHz*), together with our optimized result (Trace C). This result is obtained through the use of the HP Network Analyzer under the easy-to-use full two-port calibration procedure. First of all, we can observe that both of them show a good agreement for its entirely bandpass configuration with the ultra-broad pass-band and the wide up-band rejection, providing an excellent proof for our proposed band-pass filter and our optimized results from the HP Momentum simulation.

Figure 4.16 shows that a minimum insertion loss (S_{21}) is achieved at *–0.6 dB* in our measurement against our predicted value of about *–0.4dB* and its pass bandwidth tends to be narrowed to a very small extent. Our measured return loss (S_{11}) is found about *–16.0 dB* at maximum, a little higher than our predicted value of *–20.0 dB*, which is mainly caused by a slightly asymmetrical configuration in its return loss (S_{11}) as illustrated in Figure 4.16. This visible difference may be attributed to the small error of our fabrication tolerance and also the difficult-to-guarantee strip conductor configuration in our etching fabrication.

4.7 Conclusion

In this work, an aperture-compensated parallel-coupled microstrip line (AC-PCML) structure is applied for innovative design of a new class of size-miniaturized, multi-pole and broadband microstrip band-pass filter. At first, we show that the AC-PCML itself exhibits its filtering behavior with two poles in the case of *J>Yo*. Subsequently, a uniform line section is brought between the two AC-PCML sections to construct a prototype layout of the proposed band-pass filter. The operating mechanism of this filter is explained and its frequency response is optimally designed to exhibit a multi-pole and broadband filtering property. The multiple poles are contributed by the first- and second-order resonant modes of the line resonator, as well as the tight coupling of the

two PCML, e.g., $J=Y_0$. Our results show a ultra-broadband and 4-pole bandpass behavior with $BW>70\%$ & $|S_{11}|<-15dB$. Furthermore, a pair of capacitive open-end stubs is attached at the central location of this line resonator to effectively tune resonant frequencies of the second and fourth-order harmonics. Improved version of the band-pass filter with a single capacitive-loaded line resonator is designed to show its attractive features such as low return-loss (<-20 *dB*), wide up-band of rejection (>100%) and broad bandwidth (*60%*). Our measured results are in an excellent agreement with our predicted results over a wide frequency range (*1.0* to *15.0 GHz*) and the fabricated filter shows $|S_{11}|<-16dB$ & $|S_{21}|>-0.6dB$ within the pass-band $BW=60\%$.

References

[1] G. L. Matthaei, L. Young, and E. M. T. Jones, *Microwave Filters, Impedance-Matching Networks, and Coupling Structures*, Artech House, Norwood, 1980.

[2] S. B. Cohn, "Parallel-coupled transmission-line-resonator filter," *IRE Trans. Microwave Theory Tech.*, vol.MTT-6, pp.223-231, Apr., 1958.

[3] L. Zhu and K. Wu, "Accurate circuit model of interdigital capacitor and its application to design of new quasi-lumped miniaturized filters with suppression of harmonic resonance," *IEEE Trans. Microwave Theory Tech.*, vol.MTT-48, no.3, pp.347-356, Mar. 2000.

[4] L. Zhu, H. Bu and K. Wu, "Aperture compensation technique for innovative design of ultra-broadband microstrip bandpass filter," *2000 IEEE MTT-S Int. Microwave Symp. Dig.*, vol.1, pp.315-318, Boston, June 11-18, 2000.

[5] M. Makimoto and S. Yamashita, "Bandpass filters using parallel coupled stripline stepped impedance resonator," *IEEE Trans. Microwave Theory Tech.*, vol.MTT-28, no.12, pp.1413-1417, Dec. 1980.

CHAPTER V
CONCLUSIONS

In the present Master's thesis, an aperture compensation technique has been proposed and applied for design of low-loss microstrip low-pass filter and miniaturized microstrip broad band-pass filter. With a backside aperture on the ground plane underneath the strip, the aperture-compensated microstrip line (AC-ML) and aperture-compensated parallel-coupled microstrip line (AC-PCML) structures are studied for the realization of high impedance and tight frequency-distributed coupling behavior, respectively.

In the beginning, the electrical performance of traditional ML and PCML structures is quantitatively characterized by some well-established closed-form design equations that show their drawbacks such as high conductor loss and relatively weak coupling. By keeping the strip width electrically large ($W=0.2mm$), this low-loss AC-ML structure is characterized into an equivalent circuit model with one series reactance and two parasitic shunt susceptances. Those extracted parameters indicate that a wide aperture allows realizing a good microstrip series reactive element due to its high impedance. On the other hand, the AC-PCML structure is extensively studied over a wide frequency range in terms of a unified equivalent J-inverter circuit model. The extracted parameters exhibit its extremely tight coupling behavior ($J>Y_0$) and also its frequency-dependent periodicity.

Next, a five-stage microstrip low-pass filter is formulated by linking two AC-ML sections together with three wide ML sections in a cascaded manner and its low-pass behavior is analyzed and optimally designed by using its equivalent circuit model. The whole filter layout is then simulated with the HP Momentum software and further optimized by slightly adjusting some of filter dimensions. Also, a filter sample is fabricated and measured to verify the predicted results for the return loss ($S_{11}<-15dB$)

within the low-pass band and minimum insertion loss (S_{21}=-25dB) in the high-stop band.

On the other hand, the proposed AC-PCML structure is applied for the realization of a new miniaturized, multi-pole and broadband microstrip band-pass filter. By inserting a uniform line section in the two AC-PCML sections, a prototype band-pass filter is formulated and characterized to investigate its operating mechanism in terms of its J-inverter based topology. Its frequency response is optimally designed to exhibit its multi-pole and broad filtering properties. The multiple-pole broadband filtering behavior is contributed by the first- and second-order resonant modes of the line resonator, as well as the tight coupling of the two PCML, e.g., $J=Y_0$.

Then, a pair of capacitive open-end stubs is attached to this line resonator to tune resonant frequency of the second and fourth-order harmonics. This improved band-pass filter is designed to show its attractive features such as low return-loss (<-20 dB), wide up-band of rejection (>100%) and broad bandwidth (60%). Our measured results are in excellent agreement with our predicted results over a wide frequency range (1.0 to 15.0 GHz) and the fabricated filter shows $|S_{11}|$<-16dB and $|S_{21}|$>-0.6dB within the pass-band BW=60%.

With the increasing development of the three-dimensional (3-D) fabrication technology such as LTCC (Low-Temperature Co-fired Ceramic) and M(H)MICs, it can be expected that the aperture compensation technique proposed in this research is very useful for the realization of multilayered microstrip integrated circuits with low-cost, low-loss, high-quality and size-miniaturized electrical and geometrical features. Also, the newly proposed operating mechanism of the multi-pole broad bandpass filter can be further extended to construct a new class of miniaturized and/or light-weight band-pass filters with adjustable bandwidth and good harmonic suppression using other planar and non-planar transmission line structures as well as waveguide structures.